Max-Planck-Institut
für Meteorologie

MAX-PLANCK-GESELLSCHAFT

International Max Planck Research School
on Earth System Modelling

Turbulent Enhancement of the Melt Rate at an Ice-Ocean Interface

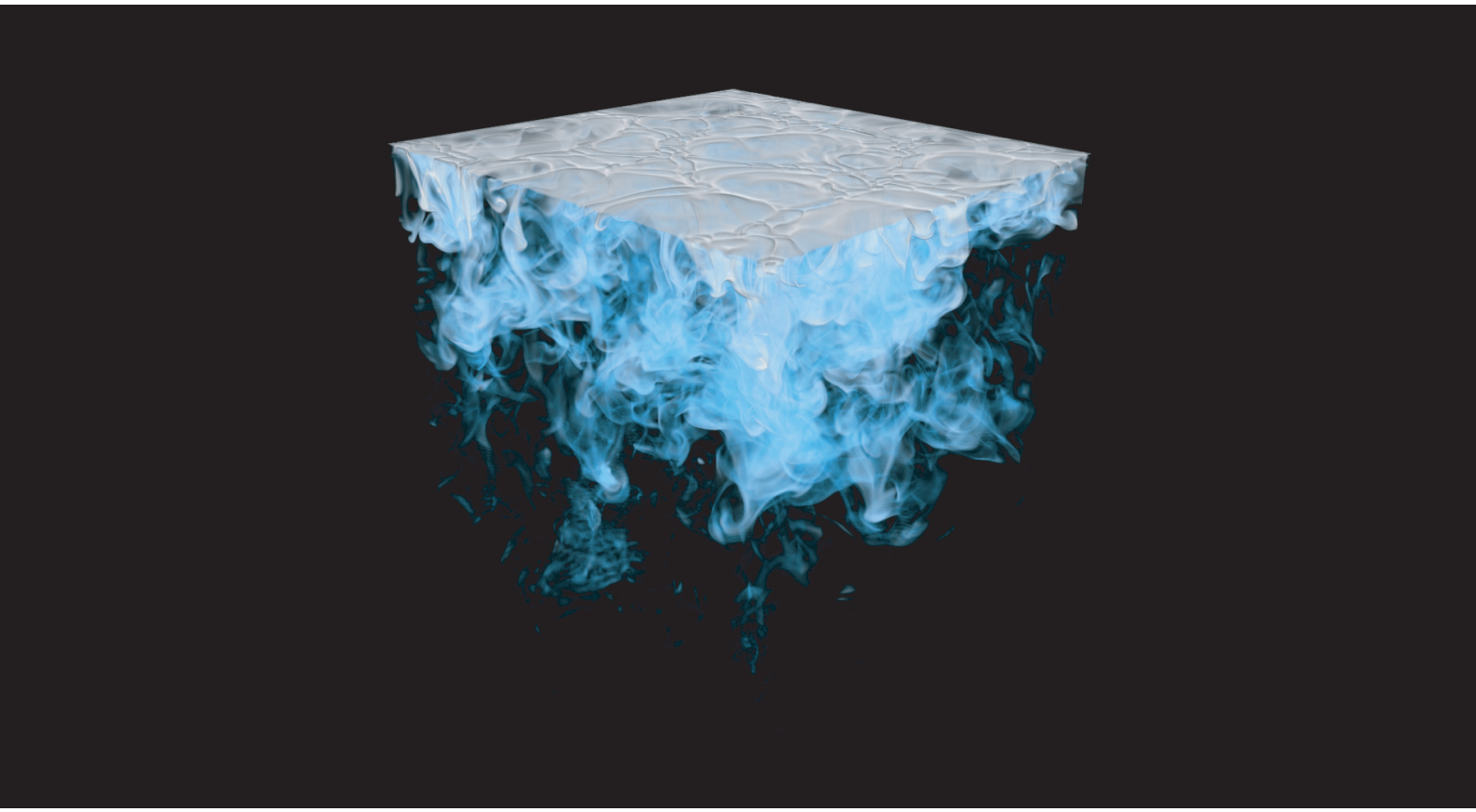

Thomas Keitzl

Hamburg 2015

Berichte zur Erdsystemforschung
Reports on Earth System Science

176
2015

Hinweis

Die Berichte zur Erdsystemforschung werden vom Max-Planck-Institut für Meteorologie in Hamburg in unregelmäßiger Abfolge herausgegeben.

Sie enthalten wissenschaftliche und technische Beiträge, inklusive Dissertationen.

Die Beiträge geben nicht notwendigerweise die Auffassung des Instituts wieder.

Die "Berichte zur Erdsystemforschung" führen die vorherigen Reihen "Reports" und "Examensarbeiten" weiter.

Notice

The Reports on Earth System Science are published by the Max Planck Institute for Meteorology in Hamburg. They appear in irregular intervals.

They contain scientific and technical contributions, including Ph. D. theses.

The Reports do not necessarily reflect the opinion of the Institute.

The "Reports on Earth System Science" continue the former "Reports" and "Examensarbeiten" of the Max Planck Institute.

Anschrift / Address

Max-Planck-Institut für Meteorologie
Bundesstrasse 53
20146 Hamburg
Deutschland

Tel./Phone: +49 (0)40 4 11 73 - 0
Fax: +49 (0)40 4 11 73 - 298

name.surname@mpimet.mpg.de
www.mpimet.mpg.de

Layout

Bettina Diallo and Norbert P. Noreiks
Communication

Copyright

Turbulent Enhancement of the Melt Rate at an Ice-Ocean Interface

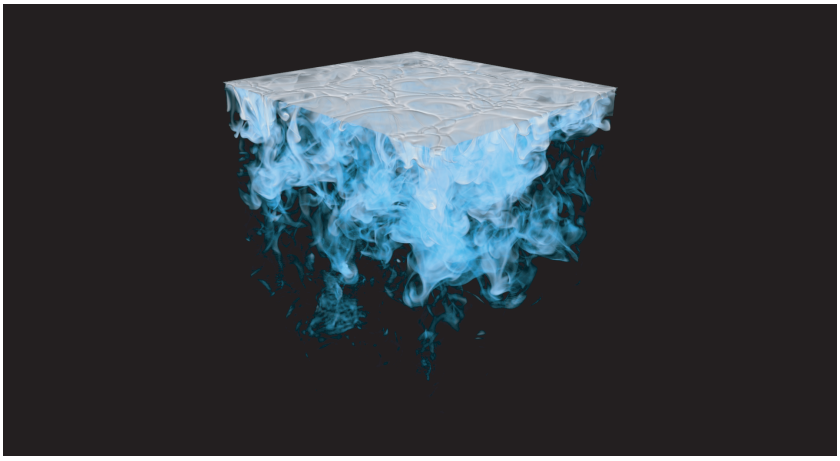

Thomas Keitzl

Hamburg 2015

Thomas Keitzl
aus Offenbach am Main, Deutschland

Max-Planck-Institut für Meteorologie
Bundesstrasse 53
20146 Hamburg

Als Dissertation angenommen
vom Fachbereich Geowissenschaften der Universität Hamburg

auf Grund der Gutachten von
Prof. Dr. Lars Kaleschke
und
Dr. Juan-Pedro Mellado

Hamburg, den 23. 11. 2015
Professor Dr. Christian Betzler
Leiter des Departments Geowissenschaften

Berichte zur Erdsystemforschung / Max-Planck-Institut für Meteorologie 176
Reports on Earth System Science / Max Planck Institute for Meteorology 2015

ISSN 1614-1199

Contents

Abstract

The ice–ocean boundary layer ubiquitously mediates the heat exchange between ocean and ice in polar regions. It is unclear how the heat exchange depends on the ocean conditions such as salinity, temperature and turbulence intensity. Generally, turbulence intensity in a boundary layer affects the heat exchange most of all. Instead of approaching the full complexity of turbulence, the present work utilises free convection into a neutrally stratified ocean beneath a smooth surface as an abstraction. In this work, direct numerical simulation and laboratory experiments of free convection are performed. They prove to complement each other: their heat fluxes and flow structures agree quantitatively. Then, simulations of a simplification of the ice–ocean boundary layer, the fresh-ice–fresh-water system, reveal how a stably stratified inversion beneath the ice shields the heat exchange; a convective Richardson number, Ri_*, is introduced to describe the shielding. Finally, the simulations of the sea-ice–sea-water system reveal how the double diffusion supports and enhances the stably stratified shield; as a result, the heat flux is reduced by one to two orders of magnitude compared to the former. Meltwater advection is estimated to influence the heat flux only for $\mathrm{Ri}_* < 0.2$. The flux ratio of heat flux to salinity flux is found to be 80-90. From the flux ratio, a physically sound assessment of the interfacial conditions and the heat flux of both systems are provided as functions of salinity, temperature and turbulence intensity.

Zusammenfassung

Die Grenzschicht zwischen Ozean und Eis bestimmt überall im Polargebiet deren Wärmefluß. Dabei ist noch unklar, in welchem Ausmaß der Wärmefluß zwischen Ozean und Eis von den ozeanischen Umgebungsbedingungen wie Salzgehalt, Temperatur und turbulenter Mischung abhängt. Im Allgemeinen bestimmt vor allem turbulente Mischung den Wärmefluß. Anstatt das Phänomen der turbulenten Mischung in seiner vollen Komplexität zu untersuchen, wird in dieser Arbeit der Ansatz verfolgt, eine Abstraktion dessen zu untersuchen: freie Konvektion unter ebenem Eis in einen neutral geschichteten Ozean hinein. Konkret bedeutet dies, daß im Folgenden direkte numerische Simulationen und Laborexperimente dieser Abstraktion durchgeführt werden. Die Simulationen komplementieren die Laborexperimente erfolgreich: Ihre Wärmeflüße und Strömungsverläufe stimmen überein. Daraufhin werden direkte numerische Simulationen verwendet, um zunächst eine weitere Vereinfachung der Abstraktion zu untersuchen, ein Systems aus Süßwassereis und Süßwasser, bevor im Anschluß das System aus Meereis und Salzwasser untersucht wird. Anhand des Systems aus Süßwassereis und Süßwasser wird deutlich, wie eine stabile Schichtung unter dem Eis den Wärmefluß abschirmt. Um diese Abschirmung zu quantifizieren, wird eine konvektive Richardson Zahl Ri_* eingeführt. Das System aus Meereis und Salzwasser zeigt schließlich, wie Doppeldiffusion die stabil geschichtete Abschirmung unterstützt und verstärkt. Der Wärmefluß wird dadurch im Vergleich zum System aus Süßwassereis und Süßwasser um ein bis zwei Größenordnungen reduziert. Der Vergleich beider Systeme deutet in der Folge darauf hin, daß der Wärmefluß durch schmelzendes Wasser nur beinträchtigt wird, wenn Ri_* kleiner als 0.2 ist. Das Fluverhältnis zwischen Wärmefluß und Salzfluß wird zu 80-90 bestimmt. Diese Arbeit präsentiert mit Hilfe des bestimmten Fluverhältnisses eine physikalisch fundierte Abschätzung des Wärmeflusses für beide Systeme in Abhängigkeit von ihrem Salzgehalt, ihrer Temperatur und der auftretenden turbulenten Mischung.

Chapter 1

Introduction

Five to ten percent of the earth's ocean is covered by ice which separates the ocean from the atmosphere. Hence, ice influences the direct exchange of internal energy, mass, and momentum on a global scale. How much ice exists and where it exactly persists on top of the oceans depends on the growth and the ablation of ice at its boundaries. Both the ice–atmosphere boundary layer and the ice–ocean boundary layer are responsible for the growth and ablation of ice. In this work, I focus solely on the ablation of ice by the ice–ocean boundary layer.

In this introduction, relevant characteristics of the ice–ocean boundary layer, of the energy transport across it, and relevant process studies are recapitulated. The recapitulation will guide the reader to the proposition of research questions and their solution in the following chapters.

1.1 The Ice–Ocean Boundary Layer

The ice–ocean boundary layer is the upper ocean layer that is influenced by the presence of ice (cf. Figure 1.1). Ice and the ocean layer that is not influenced by the presence of the ice—the far-field ocean—pose the boundary conditions to the flow in-between. It is the flow's fate to comply with these boundary conditions. As a result, the flow mixes to equalise the boundary conditions by transporting mass, momentum and energy between far-field ocean and the ice. When the boundary conditions are sufficiently destabilising, the flow even mixes turbulently.

Two main forcing mechanisms drive turbulence: shear and buoyancy. A shear occurs when the far-field-ocean current is different from the velocity of the ice. A buoyancy occurs when the density in the ocean varies due to temperature, salinity or pressure variations. In general, a combination of these two mechanisms forces the mixing while a combination of other opposing mechanisms dampens the mixing.

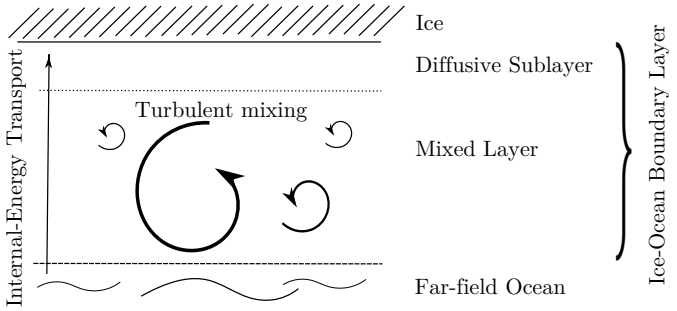

Figure 1.1: Drawing of the ice–ocean boundary layer. Ice and far-field ocean impose the boundary conditions to the boundary layer. When the boundary conditions are sufficiently destabilising, the flow in the boundary layer features turbulent mixing. The turbulent mixing has two important consequences: It enhances the internal-energy transport across the boundary layer, and the interaction of turbulent mixing with the interface promotes the formation of a diffusive sublayer beneath the ice. The internal-energy transport from the far-field ocean to the ice crosses the mixed layer and the diffusive sublayer likewise.

This work mainly focuses on the forcing and dampening of turbulent mixing by buoyancy in the absence of other forcings.

The buoyancy forcing arises from the dependence of density on temperature, salinity, and pressure, and on the boundary conditions that the ice and the far-field ocean provide. In polar oceans, the boundary conditions are nearly always that of a cold and less saline layer aloft a warmer and more saline layer of water (McPhee, 2008, p. 28). The equation of state of sea water (Sharqawy, Lienhard and Zubair, 2010) renders the temperature layering—cold aloft warm—here unstable. The salinity layering—less aloft more saline—is always stable. Generally, the effect of salinity layering excels that of temperature in the polar ocean and the ice–ocean boundary layer is stably stratified. Where salinity sufficiently meets its far-field boundary condition, temperature, however, can still vary so much that its effect reverses the effect of salinity. As a result, the buoyancy layering features a reversal and the ice–ocean boundary layer is unstable. The buoyancy reversal features the most negative buoyancy and is an intrinsic feature to the boundary layer. The instability that arises due to the buoyancy reversal is referred to as buoyancy reversal instability.

The buoyancy reversal instability solely prevails in the ice–ocean boundary layer due to the diffusivity difference between temperature and salinity. In general, hydrophysical processes that are caused by diffusivity differences are referred to as double diffusion (Stern, 1960; Turner, 1974). Double diffusion promotes the buoyancy reversal instability in the following way. Across the boundary layer the mean profiles of both temperature and salinity vary continuously from their condition at the ice towards their far-field condition. Temperature, however, diffuses stronger than salinity and the temperature layering, as a result, occurs

across a wider distance than the salinity layering. The faster diffusive broadening of the temperature layer with respect to the salinity layer will continue until the temperature-layer fraction beneath the salinity layer yields a buoyancy reversal instability (Martin and Kauffman, 1977). Then, the boundary layer mixes and, as the case may be, becomes turbulent.

Turbulent mixing in the boundary layer has two important consequences. First, it enhances the transport capabilities of the boundary layer. A turbulently enhanced transport of energy determines, then, the ablation of ice. Second, the interaction of turbulent mixing with the interface promotes the formation of a diffusive sublayer (Yaglom and Kader, 1974) just beneath the ice. The diffusive sublayer separates the ice from the layer of turbulent mixing, "the mixed layer". Any energy transport from the far-field ocean to the ice interface crosses the mixed layer and the diffusive sublayer likewise. The energy transport may hence be considered based on only one of the two parts of the ice–ocean boundary layer.

Due to the immediate vicinity of the diffusive sublayer and the ice, and due to a prospective analytical description of diffusive processes, the consideration of the energy transport across the diffusive sublayer has become the dominant approach to describe the energy transport to the ice in literature. In the following section, the basics of the energy transport are recapitulated.

1.2 The Energy Transport Through the Boundary Layer

The energy transport across the diffusive sublayer is mainly restricted to molecular diffusion because momentum boundary condition suppresses turbulence close to the ice interface—the flow may not slip and may (almost) not penetrate the ice. This diffusive sublayer is defined as the layer next to a ice interface across which the contribution of the molecular transport exceeds the turbulent transport by order one (Pope, 2000). As a result of negligible turbulent transport, the characteristics of the diffusive sublayer depend only on the diffusivities of the fluid and the buoyancy forcing, but not on the intensity of turbulence. From this it follows that the diffusive sublayer has a fixed extent. The smaller the diffusive-sublayer extent is, the larger is the energy transport at the interface. This extent is well known for horizontal interfaces if the buoyancy depends linearly on only one scalar (Mellado, 2012). For systems with a buoyancy reversal instability or for double-diffusive systems, however, the diffusive-sublayer extent is unknown. As a consequence, the energy transport is unknown, and so is the ablation rate of ice.

Besides the diffusive-sublayer extent, also the temperature difference across it determines the energy transport. The particular temperature and salinity boundary conditions (Frank, 1950) that ice imposes on the ocean summon an additional

puzzle. While mixing transports energy to ablate the ice, the ablation dilutes the upper ocean. But the mixing also transports salt towards the ice interface that counteracts the dilution. The interfacial temperature—important for the temperature difference across the sublayer—results from the equilibrium of dilution and salt transport. The interfacial conditions are, thus, subject to the thermodynamics of the ice, and to the dynamics of the ocean. This adds an interesting twist: In the end, not only molecular diffusion but also turbulent mixing is decisive for the interfacial conditions of the diffusive sublayer and the ice. The equilibrium of dilution and salt transport is readily obtained from the boundary conditions, the far-field temperature, the far-field salinity, and the ratio between the transport of temperature and salinity (Gade, 1979, 1993).

Turbulence enhances the mixing of salt and temperature as compared to molecular diffusion. Temperature and salinity are then mixed more equally in the mixed layer and the ratio between the transport of temperature and salinity is expected to be smaller than given by the ratio of the diffusivities. But turbulence does not entirely suppress the difference in molecular diffusivities, and the ratio remains different from unity. How much so, is unclear. Gade (1993) calculates the ratio in units of the total salinity and temperature difference of 2.3 from the laboratory data of Martin and Kauffman (1977) and of 2.26 from the simulation data of Wilson, Sarma and Pritchard (1980). Interestingly, the latter study considers a laminar flow, which indicates that the experiment of the former study plays also in a rather laminar regime. From the laboratory data provided by Gebhart, Sammakia and Audunson (1983), Gade further concludes that the ratio should be constant and independent of the thermal forcing for fully developed turbulence. The author is not aware of further efforts to determine the exact ratio between the transport of temperature and salinity at the interface.

Generally, systems of different forcing, shear or buoyancy, feature a similar vertical flow structure next to an interface (Pope, 2000; Mellado, 2012). Whenever turbulence aids the ablation of ice, the diffusive sublayer develops between the ice and the turbulent layer irrespective of the forcing. The characteristics of the diffusive sublayer determine the transport of internal energy, mass and momentum to the ice. In summary, two unknown characteristics of the diffusive sublayer hinder the general determination of the energy transport across the diffusive sublayer: First, the extent of the diffusive sublayer beneath ice, and second, the interfacial temperature and salinity that mark the interface of ice and diffusive sublayer. Both unknowns will be addressed in this work. The following section introduces the methods that will be applied to do so, as well as the state-of-the-art in the application of the methods.

1.3 Approaches to Studying the Energy Transport

To gain a qualitative understanding of the behaviour of the energy transport from observations has proven difficult. In the field, the transport of internal

energy, mass and momentum are hard to measure with satisfactory resolution. Commonly, the above-mentioned forcing mechanisms and other environmental conditions interact, such as surface heterogeneity, roughness, intermittency and impacts from the ice–atmosphere boundary layer. Great efforts are therefore necessary to obtain a comprehensive picture of the field conditions that later on allow one to interpret the data, or questionable simplifications need to be employed. In the laboratory, boundary and initial conditions are well under the researcher's control and some success in determining the interfacial temperature and salinity has been made (Martin and Kauffman, 1977; Gebhart, Sammakia and Audunson, 1983; Gade, 1993). A laboratory setup is, however, necessarily bounded, and the achievable independence of turbulence intensity is limited. In numerical studies, on the contrary, single processes may be investigated in a well-defined setup that is unaffected by the bounding geometry or by a limited scale separation. It is key to the study of the diffusive sublayer that the flow evolution is resolved down to diffusion. Direct numerical simulation offers the opportunity to do so without any turbulence parameterisation.

Three main processes involved in the ablation of ice were isolatedly studied in this way so far.

Mellado (2010) studies the buoyancy reversal instability motivated by the cloud-top mixing layer in the atmosphere. He finds a horizontal layered structure whose evolution is determined by molecular transport. A relatively thin inversion of constant thickness forms aloft a turbulent convection layer that continuously broadens with time. The inversion thickness depends on the diffusivity, the buoyancy and a well-defined scalar mixing fraction only. The turbulent layer approaches a self-preserving state that is characterised by a reference buoyancy flux.

Mellado (2012) provides the boundary-layer structure of purely buoyancy-driven free convection over a heated plate. He forces free convection with a linear buoyancy, thus, does not account for buoyancy reversal. He finds that the internal-energy transport of free-convection systems is $\mathrm{Nu} \propto \mathrm{Ra}^{-\gamma}$ with Nusselt number Nu, Rayleigh number $\mathrm{Ra} \in 5 \times \left[10^5; 10^7\right]$ and $\gamma \in [.28;\ .30]$ as generally observed in Rayleigh-Bénard convection (Chillá and Schumacher, 2012). The Nusselt number is a measure for the internal-energy transport. The Rayleigh number is a measure for the buoyancy forcing of the system. Mellado (2010, 2012) has neither considered the buoyancy reversal instability in vicinity of an interface, nor double diffusion.

Carpenter, Sommer and Wüest (2012) take up convective double-diffusive interfaces. Their experiment setup consists of two vertically inverted ice–ocean boundary layers on top of each other. They find a double-boundary-layer structure that allows gravitationally unstable boundary layers at the edge of the diffusive interface. The thickness ratio of the diffusive interface, a proxy for the ratio between the transport of temperature and salinity, is found to scale with the diffusivity ratio to yield about 2.6 for as high a diffusivity ratio as 100. They further confirm that turbulence is not able to penetrate the stable stratification of

the interface core, and that molecular diffusion of salinity determines the growth of the diffusive-interface thickness in time.

The mechanism responsible for the formation of the diffusive sublayer next to an interface (Mellado, 2012) might be inherently different from that of forming diffusive layers in the absence of an interface (Mellado, 2010; Carpenter, Sommer and Wüest, 2012). It is a priori not clear how the interface and the effectively non-linear buoyancy forcing will influence each other, and no studies on it have come to the author's attention. This ignorance reflects in uncertainty on the rates of ablation of ice in the ice–ocean boundary layer with respect to far-field temperature, salinity, and ice–water speed (Notz, McPhee, Worster *et al.*, 2003). I study the influence of the ice interface and the effectively non-linear buoyancy forcing on each other in a combined laboratory experiment and numerical study to diminish the uncertainty on the ablation rate of ice. At first, I review the numerically simulated evolution of an ice–water boundary layer with a laboratory tank experiment to complement the real-world measurement with comprehensive simulation data. Then, I use the simulation to investigate the extent of the diffusive sublayer and the ratio between the transport of temperature and salinity.

1.4 Research Proposition

With this work I address the overarching question: **How does the diffusive sublayer that separates the ice from turbulent convection evolve with respect to far-field temperature, salinity, and ice–water speed?** Rather than trying to quantify the impact of a plurality of forcing mechanisms on the diffusive sublayer, one main question that guides me focuses on the qualitative impact of turbulence that confronts the diffusive sublayer. A second main question then focuses on the influence of double diffusion on the diffusive sublayer. Two methodological questions have to be addressed first, before the two main questions will be tackled and answered thereafter. Each of these questions is now posed individually in the following four paragraphs.

To study the overarching question, I choose a buoyancy-driven setup to study the diffusive sublayer, because it provides a well-known and well-controllable framework in both numerical simulations and laboratory. Buoyancy-driven turbulence beneath an ice–ocean interface mainly depends on the combination of several processes mentioned in the previous section: the influence of the ice interface, the buoyancy reversal instability, and double diffusion. The first methodological question that needs to be resolved is: **How can the processes involved in the turbulent mixing be studied independently from each other in the context of ice ablation?** I present the fresh-ice–fresh-water system as an idealisation of the buoyancy-driven ice–ocean system in chapter two. It shows that the idealisation simplifies the research subject in that it reduces the number of independent control parameters without changing the qualitative structure of

the mean-buoyancy profile. It allows one therefore to study the evolution of the mean-buoyancy profile as a combination of two well-known systems: the influence of the interface (Mellado, 2012), and the buoyancy reversal instability (Mellado, 2010). Along with the idealisation, I present a laboratory setup and the direct numerical setup that can be used to study both the fresh-ice–fresh–ocean boundary layer and the sea-ice–sea-water boundary layer.

The second methodological question is: **Can direct numerical simulations be used to reproduce and complement laboratory experiments?** I employ the idealised setup in the laboratory and in direct numerical simulations to review their evolution in chapter three. The temporal evolution of their mean-temperature profiles and the internal-energy change of the whole system will be used to compare the two. The assessment of the comparison allows one to review the validity of the physical model employed in the direct numerical simulation and further provides indications as to whether the vertical melt-water advection is relevant for the physical model.

My first main question is to understand: **How does the buoyancy reversal instability influence the flow structure of free convection next to the ice interface?** The presented idealisation neglects the influence of salinity, allows one to omit double diffusion and to focus on the evolution of the mean-buoyancy profile that is caused by the buoyancy reversal instability. I employ the idealised setup with direct numerical simulation in chapter four to overcome resolution and size limitations of the laboratory experiment and to yield statistically converged boundary-layer mean profiles. The statistically converged boundary-layer information allows me to learn which dominant processes determine the flow structure next to the interface and the melt rate. Once the underlying dynamics of the processes is understood, the simulations are employed to assess further aspects of the flow, such as the influence of vertical melt-water advection on the flow next to the interface, the spatial inhomogeneity of the melt rate, implications of the results of the fresh-ice–fresh-water system for the more general case of ice floating on a salty ocean.

My second main question is to understand: **How does double diffusion influence the flow structure of free convection next to an interface?** I employ the full setup that includes the interplay of temperature and salinity with direct numerical simulation in chapter five. The diffusivity ratio between temperature and salinity—the Lewis number—is varied to approach real-world conditions. As opposed to previous research methods, the ratio between the transport of temperature and salinity at the interface is readily obtained as a simulation outcome. Consequently, this work provides a physically sound answer to the question: What are the interfacial conditions between ice and the diffusive sublayer? The simulations are then used to study the question: How much is the diffusive-sublayer extent increased compared to that of the idealised setup? As a consequence, this work further provides approximations of the energy transport, as well as for the ablation rate of ice.

Chapter 2

Setup and Methods

The concept of this study has been introduced in the previous chapter: a combined laboratory and simulation approach to study the individual processes of the energy transport beneath the ice. The combined approach to study the energy transport from the ice–ocean boundary layer to the ice requires a well-defined common framework. This chapter sets it up (section 2.1). Two similar subsetups are derived from the physical setup: the full setup that incorporates salt, and an idealised setup that is only driven by temperature. Then, this chapter explains the methods that are employed, namely the laboratory experiment and the direct numerical simulation (section 2.2).

2.1 The Physical Setup

A mass of solid, pure ice rests on top of an initially motionless body of sea water of fixed uniform temperature $T = T_\infty$ (cf. Figure 2.1a). Ice and water form a horizontal interface. The ice mass is isothermal at the freezing temperature of water and has a smooth surface. Hence, the ice imposes a Dirichlet boundary condition on the temperature field of the water and a no-slip boundary condition on the velocity field of the water. I consider this physical setup of the ice–ocean interface together with the sea-water body as my system of interest.

This system is purely buoyancy driven. I define buoyancy b as:

$$b = g\frac{\rho_\infty - \rho}{\rho_\infty}, \tag{2.1}$$

with earth's gravitational acceleration, g, and water density, ρ, where the subscript $_\infty$ denotes the value of a property far away from the interface—in the far field.

Generally, the density of sea water, ρ_{sw}, depends on temperature, T, and on salinity, S. It does so in a particular way that is, to present day, best described

as

$$\rho_{\mathrm{sw}}\left(S,T\right)=\rho_{\mathrm{w}}\left(T\right)+a_1\left(T\right)\ S+a_2\left(T\right)\ S^{3/2}+a_3\ S^2, \tag{2.2}$$

with the density dependence of fresh water, ρ_w, the high-order polynomials a_1, a_2 and a constant a_3 (Sharqawy, Lienhard and Zubair, 2010). Subsequently, I approximate this function with the product of a linear salinity-dependence of the density, ρ_s, and a parabola as temperature-dependent variation to it, $\tilde{\rho}_t$. I define the density ρ as:

$$\rho\left(S,T\right)=\rho_s\left(S\right)\ \tilde{\rho}_t\left(T\right), \tag{2.3a}$$

$$\rho_s\left(S\right)=c_1+c_2\ S, \tag{2.3b}$$

$$\tilde{\rho}_t\left(T\right)=1-c_3\left(T-T_{\mathrm{m}}\right)^2. \tag{2.3c}$$

Notice that the temperature-dependent variation $\tilde{\rho}_t\left(T\right)$ is dimensionless. It is chosen analogous to the functional form of the fresh-water density formula with the temperature of maximum density, T_{m}. To allow for the analogy, the variation of T_{m} with the solute concentration, S, needs to be considered,

$$T_{\mathrm{m}}\left(S\right)=c_4-c_5\ S. \tag{2.4}$$

The density-formula coefficients c_i need to be chosen according to the particular parameter range of T and S of the system and according to the solute under consideration. c_1 is the background density, c_2 is the haline contraction coefficient, c_3 is the relative thermal expansion coefficient, c_4 is the maximum-density temperature, and c_5 describes the variation of the maximum-density temperature with salinity. Within the confining temperatures, T_{ice} at the ice interface and T_∞ in the far field, and the confining salinities, S_{ice} at the ice interface and S_∞ in the far field, the buoyancy based on ρ varies between zero in the far field, a minimum buoyancy, b_m, and the interfacial buoyancy, b_{ice}, that can exceed the far-field value.

The system is purely buoyancy driven and evolves in space and time according to the evolution equations of mass, momentum, internal-energy and solute. With the velocity field $\mathbf{v}\left(\mathbf{x},t\right)$, the temperature field $T\left(\mathbf{x},t\right)$, the salinity field $S\left(\mathbf{x},t\right)$, the spatial coordinate $\mathbf{x}=x_1\mathbf{e}_1+x_2\mathbf{e}_2+z\mathbf{e}_3$, with $\mathbf{e}_i=\varepsilon_{ijk}\mathbf{e}_j\mathbf{e}_k$, and with time t, these evolution equations are respectively given as

$$\partial_j\upsilon_j=0, \tag{2.5a}$$

$$\partial_t\upsilon_i=-\upsilon_j\partial_j\upsilon_i+\nu\partial_j^2\upsilon_i-\partial_i p+b\left(S,T\right)\ \delta_{i3}, \tag{2.5b}$$

$$\partial_t T=-\upsilon_j\partial_j T+\kappa_T\partial_j^2 T, \tag{2.5c}$$

$$\partial_t S=-\upsilon_j\partial_j S+\kappa_S\partial_j^2 S. \tag{2.5d}$$

The equations are given in the Bussinesq approximation. ν is the kinematic viscosity, κ_T the thermal diffusivity, κ_S the diffusivity of salinity, p the modified

kinematic pressure, ∂_t the temporal derivative and ∂_i is the spatial derivative in direction $\mathbf{e}_i$.

After an initial transient, once the effet of the initial conditions is sufficiently forgotten, the system solely depends on a set of control parameters $\{\nu,\ \kappa_T,\ \kappa_S,\ T_{\mathrm{ice}},\ T_\infty,\ S_{\mathrm{ice}},\ S_\infty,\ c_i\}$. Typically, dimensional analysis for a linearised buoyancy function provides the set of independent control parameters $\{\mathrm{Pr},\ \mathrm{Le},\ R_\rho^s\}$, with Prandtl number $\mathrm{Pr} = \nu/\kappa_T$, Lewis number $\mathrm{Le} = \kappa_T/\kappa_S$, and density ratio $R_\rho^s = (\beta\,(S_\infty - S_{\mathrm{ice}}))\,/\,(\alpha\,(T_\infty - T_{\mathrm{ice}}))$, where α is the thermal expansion coefficient, $\alpha = 1/\rho\partial\rho/\partial T$, and β is the saline contraction coefficient, $\beta = 1/\rho\partial\rho/\partial S$.

2.1.1 The Fresh-Ice–Fresh-Water System

The core idea of this work is to idealise the system based on its prospective mean-buoyancy profile. The prospective mean-buoyancy profile beneath the ice–ocean interface looks as follows (cf. Figure 2.1b, dotted line). The buoyancy at the ice interface is higher than the buoyancy in the far field. The system would be stably stratified but the buoyancy between ice interface and far field features a global minimum. This buoyancy minimum leads to overturning and mixing. I propose the fresh-ice–fresh-water system, $S = 0$ g kg^{-1}, with a far-field temperature $T_\infty > T_m$ as an idealisation to the more general ice–ocean system. The application offers the possibility to separately study one aspect of the general system, the buoyancy-forcing structure, in a well defined environment.

The buoyancy-forcing structure of the idealised setup is obtained from the buoyancy definition (cf. Eq. (2.1)) with $c_1 = 999.96$ kg m^{-3}, $c_2 = c_5 = 0$, with a slightly differently defined thermal coefficient $c_3 \times c_1 = \alpha = -7.00 \times 10^{-3}$ kg m^{-3} ℃$^{-2}$, and $c_4 = 3.98$ ℃. This choice of c_i yields a simpler density function.

$$\rho(T) = c_1 + \alpha\,(T - T_{\mathrm{m}})^2 \tag{2.6}$$

This parabolic density function deviates relatively to Eq. (2.2) by less than 0.01 % between 0 ℃ and 30 ℃ for $S = 0$ g kg^{-1}. The resulting buoyancy-forcing structure is qualitatively similar to the one beneath the ice–ocean interface. In the case of the fresh-ice–fresh-water system, it is sufficient to follow the evolution of the water temperature to understand the buoyancy-forcing structure.

The water body has a fixed uniform temperature, T_∞. The ice also has a fixed uniform temperature, T_{ice}, that corresponds to the freezing temperature. Just beneath the fresh-ice–fresh-water interface, the temperatures merge: With increasing distance from the ice interface, the water temperature increases from T_{ice} to T_∞ (cf. Figure 2.1c). As the water temperature increases, the density first increases (as long as $T < T_m$) and then decreases ($T > T_m$) (cf. Figure 2.1d). Accordingly, the buoyancy first decreases and then increases again. Hence, for

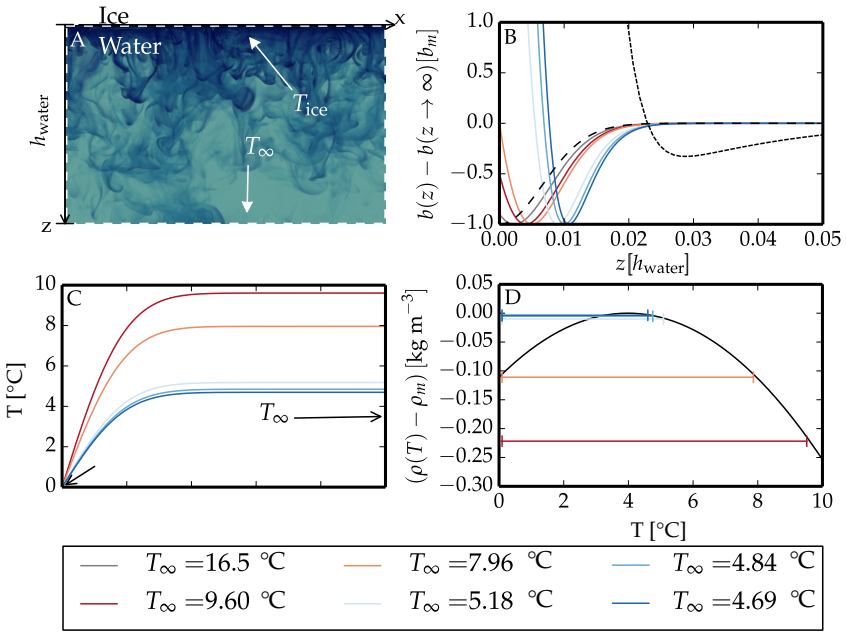

Figure 2.1: Sketch of the system studied. a) Ice rests on top of a water body (greenish). A sketch of a turbulently mixed temperature field is exemplarily given (dark blue). b) The density variation shown in (c) poses a certain buoyancy profile in the system. The dashed line shows a buoyancy profile for a density function without buoyancy reversal. The dotted line is a prospective mean-buoyancy profile of the sea-ice—sea-water interface for a Ri = 130. Ri = 130 corresponds to the far-field conditions employed by Martin and Kauffman (1977). c) The water temperature increases from the interface value, T_{ice}, to the far-field value, T_∞. The distance from the interface is given in units of the tank height h_{water}. Different colours symbolise different far-field temperatures according to cf. Figure 2.1c. The given profiles are the initial profiles of the numerical simulations of this work. d) Coloured bars indicate the temperature range of density variation that characterises the system for a certain far-field water temperature.

$T_\infty > T_m$, the buoyancy in the far field is higher than the buoyancy close to the interface and the system is convectively unstable (cf. Figure 2.1b). I am interested in this convectively unstable regime.

For $T_\infty = 2\,T_m$, the buoyancy at the interface equals the buoyancy in the far field. The buoyancy profiles suggest a different behaviour if $T_\infty < 2\,T_m$ compared to if $T_\infty > 2\,T_m$. For $T_\infty > 2\,T_m$, the whole column of fluid can overturn (cf. Figure 2.1b, reddish profiles). In contrast, for $T_\infty < 2\,T_m$, there exists a layer next to the interface that is statistically stable (cf. Figure 2.1b, bluish profiles). This stably stratified layer beneath the ice acts as a shield against the warmer fluid of the convectively unstable region as will be shown below.

The spatiotemporal evolution of the system is determined by the buoyancy b (cf. Eq. (2.5b)). For sufficiently low viscosity, the system becomes turbulent, decorrelates from its initial state, and solely depends on the set of control parameters $\{\nu,\ \kappa,\ T_m - T_{\mathrm{ice}},\ T_{\mathrm{ice}} - T_\infty\}$. Dimensional analysis provides the set of independent control parameters $\{\mathrm{Pr},\ \chi_{\mathrm{m}}\}$, with $\mathrm{Pr} = \nu/\kappa_T$ and $\chi_m = (T_m - T_\infty)\,/\,(T_{\mathrm{ice}} - T_\infty)$. This is a remarkable simplification compared to the physical system that depends on three independent control parameters. While the system is reduced to only two independent control parameters, it maintains the buoyancy-forcing structure.

This investigation shall be constrained to water-like fluids of fixed Prandtl number $\mathrm{Pr} = 10$. Hence, any flow property solely depends on one governing control parameter, χ_{m}, and on the position in space and time, $\{\chi_{\mathrm{m}},\ \mathbf{x},\ t\}$. I am interested in convectively unstable conditions, $T_\infty > T_m$, so that $0 < \chi_m < 1$.

The fully developed turbulent system is statistically homogeneous in horizontal directions. I denote horizontally averaged quantities by $\langle\cdot\rangle$ and fluctuations around that mean by $\cdot'$. Horizontally averaged statistics only depend on $\{\chi_{\mathrm{m}},\ z,\ t\}$ with $z = \mathbf{x}\cdot\mathbf{e}_3$ and the origin of $\mathbf{x}$ chosen such that z gives the distance from the interface. χ_{m}, b_m and T_∞ equivalently describe the system (cf. Eqs. (2.10,2.13)).

2.1.2 The Sea-Ice–Sea-Water System

The inclusion of salt is the sole difference between the fresh-ice–fresh-water system and the sea-ice–sea-water system. Now, both temperature and salinity influence the buoyancy. The diffusivity of salinity, κ_S, is significantly smaller than the diffusivity of temperature, κ_T, and the evolution of buoyancy is not given in terms of one conserved scalar anymore (Mellado, Stevens, Schmidt *et al.*, 2010). Thus, a second scalar diffusion–advection equation describes the evolution of salinity, Eq. (2.5d) and κ_S adds to the set of independent control parameters of the system.

Salinity influences the evolution of the flow in two ways. First, the freezing temperature of water fixes the interfacial temperature, T_{ice}, no longer at zero degrees

Celsius, but depends on the interfacial salinity, S_{ice}. The resulting interfacial buoyancy is

$$b_{\text{ice}} = b\left(S_{\text{ice}}, T_{\text{ice}}\right). \tag{2.7}$$

Second, while the buoyancy reversal instability no longer occurs due to the density anomaly of water, it is now due to the mixing of temperature and salinity. The minimum buoyancy, b_m, occurs when fluid of far-field salinity, S_∞, is cooled to the interfacial temperature, T_{ice}:

$$b_m = b\left(S_\infty, T_{\text{ice}}\right) \tag{2.8}$$

(cf. Eq. (2.3)).

The fully turbulent free-convection sea-ice–sea-water system depends solely on the set of control parameters, $\{\nu,\ \kappa_T,\ \kappa_S,,\ T_{\text{ice}},\ T_\infty,\ S_{\text{ice}},\ S_\infty,\ c_i,\ \}$. Instead of focusing on the precise density-formula coefficients, c_i, I will study the sea-ice–sea-water system based the most striking features of the buoyancy function: the interfacial buoyancy, b_{ice}, and the minimum buoyancy, b_m. Under this premise, dimensional analysis provides a set of independent control parameters as $\{\text{Pr},\ \text{Le},\ \text{Ri}_0\}$, with $\text{Pr} = \nu/\kappa_T$, $Le = \kappa_T/\kappa_S$, and Richardson number

$$\text{Ri}_0 = 1 - b_{\text{ice}}/\left|b_m\right| \qquad . \tag{2.9}$$

As will be shown during this study, now Ri_0 represents the choice of the far-field conditions, T_∞ and S_∞.

2.2 The Methods

2.2.1 Laboratory Experiment

The laboratory setup that I use to mimic the idealised setup consists of a Plexiglas tank filled with tap water, a thermistor cascade just beneath the water surface, and an ice block dangling on a manual tackle just above the water surface (cf. Figure 2.2). The setup resides in a cold room whose temperature can be controlled with a precision of ±3 °C. The water body has the dimensions 0.347^3 m^3 and is laterally isolated by a Styrofoam cover around the tank. Temperature changes are measured with a cascade of 23 thermistors. The thermistor cascade has a spacing of 7 mm between the thermistors and a total profile length of 154 mm. Each thermistor is spherical with a radius of 1 mm and is placed on the tip of a 4 mm thick and 2 cm long finger to minimise the influence of the instrument body on the flow. The precision of the temperature measurement is at least 0.01 K while temperature changes are measured with a response time of two to four seconds depending on the sign of the temperature change. The ice block, 8 cm to

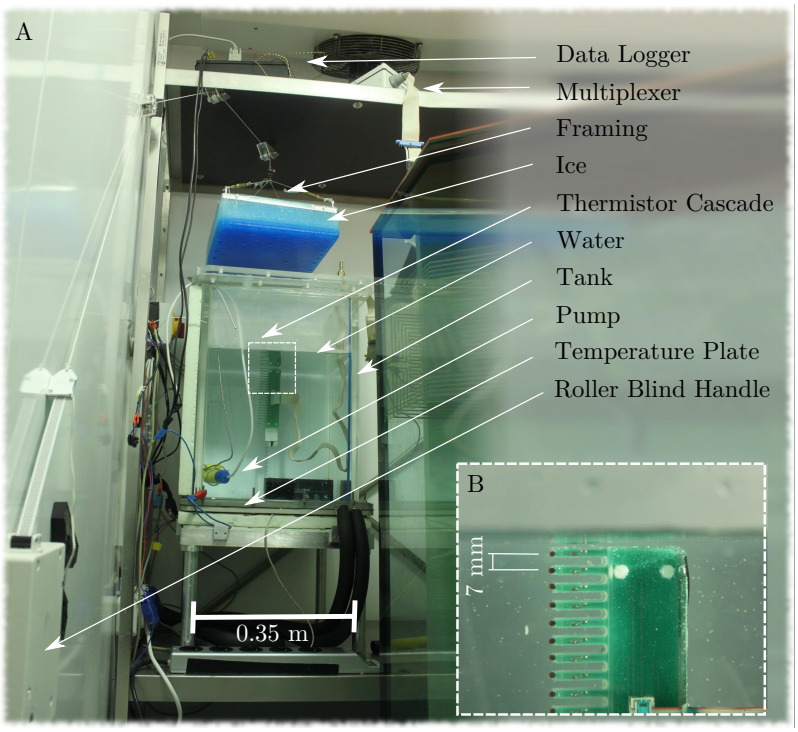

Figure 2.2: Laboratory setup. a) Dyed ice dangles on a manual tackle just above the water body in the tank. The setup is placed in a cooling chamber. b) Magnification of the upper thermistor cascade.

13 cm thick, covers almost the entire water surface and is prepared from distilled water prior to the experiment.

Before an experiment is conducted, I orientate the system components and prepare the temperatures of the water body and the cold room. I align the ice block horizontally to attach it plainly to the water surface and displace the thermistor cascade vertically such that the upper thermistor is just beneath the water surface. A pump mixes the water body to a homogeneous initial temperature T_∞. The cold-room temperature is set to match T_∞ in order to minimise any temperature gradient between the water body and its lateral surrounding. I keep the cold-room temperature constant at T_∞ for several hours to ensure that the ice is isothermal. When the pump stops, I await the decay of turbulent kinetic energy for 3 minutes and then cautiously lower the ice block via the manual tackle.

The experiment starts as soon as the ice touches the water surface. The ice is not lowered further. The thermistor cascade measures a temperature profile every 5 seconds for an experiment run time Δt. After that, the ice block is lifted from the water surface and the recording continues for about another minute while the water is mixed with the pump to record the final bulk temperature of the system, T_end. This entire procedure constitutes one realisation of the laboratory experiment. The horizontal position of the thermistor cascade is varied after every laboratory realisation.

First, I assess the capability of the setup to temporally resolve the turbulently mixing system, and to detect thermal changes that result from the mixing. For high far-field temperatures, the system evolves too quickly compared to the response time of the thermistors. For lower far-field temperatures, the temperature changes too little compared to the temperature sensitivity of the system. Second, I record an ensemble of 25 realisations at $T_\infty = 5$ °C and $\Delta t = 15$ min to capture the mean temperature profile of the turbulent system. Third, I record several ensembles of small realisation number (three to five) at $T_\infty \in \{4.5,\ 5,\ 6,\ 15\}$ °C and varying run time, Δt, to capture the temporal bulk-temperature change of the turbulent system.

2.2.2 Direct Numerical Simulation

I integrate Eqs. (2.5) using a high-order finite-difference method on a collocated, structured grid. The integration is approximated by a fourth-order Runge–Kutta scheme and the spatial derivatives by sixth-order spectral-like finite differences (Williamson, 1980; Lele, 1992). After every integration step, a pressure solver ensures fulfillment of the solenoidal constraint. For this, a Fourier decomposition is employed along periodic horizontal coordinates and a factorisation of the resulting second-order equations in the vertical coordinate (Mellado and Ansorge, 2012).

The calculations are performed on three-dimensional grids, that yield an aspect ratio of 3.33 : 1 (big simulations) and 1.33 : 1 (small simulations). Adequacy

of the vertical resolution, the domain height, and the domain width has been assured for the simulations of the fresh-ice–fresh-water system. Consequently, the results discussed in this work are sufficiently independent of those simulation properties. The simulations of the sea-ice–sea-water system have been derived from the well-tested simulations of the fresh-ice–fresh-water system. Adequacy of the vertical resolution has also been assured for those simulations but influences of the domain height on the simulations cannot completely be ruled out.

The grid spacing is uniform in the horizontal directions $\mathbf{e}_1$, $\mathbf{e}_2$ and in most of the vertical direction $\mathbf{e}_3$. The resolution in $\mathbf{e}_3$ next to the ice interface, however, is increased because the main mean-temperature variation all over the domain occurs next to the ice interface. This temperature variation potentially entails the main mean-buoyancy change, a change in the forcing of the system from a positive to the global-extreme negative value and back to almost zero (cf. Figure 2.1b). To fully cover this buoyancy variation, I increase the resolution next to the ice interface by a factor of five for the simulations of the fresh-ice–fresh-water system. For the simulations of the sea-ice–sea-water system, a factor of 2.5 was sufficient to ensure an adequate vertical resolution next to the ice interface. The regions of uniform and adjusted resolution in $\mathbf{e}_3$ are gradually matched by hyperbolic tangents. Finally, the grid in $\mathbf{e}_3$ far from the ice interface is coarsened to save computing time. This part of the domain serves to diminish the influence of the computational boundary on the flow.

The boundary conditions in the velocity field are no-slip and no-penetration at the ice interface, and free-slip and no-penetration in the far field. The boundary conditions in the scalar fields—temperature field and salinity field—are Dirichlet at the ice interface and Neumann in the far field. The initial condition is an error function of thickness d across the vertical profile in the scalar and a zero field in velocity. The scalar fields are perturbed close to the ice interface with a wavelength that corresponds to 7 d [see Mellado (2012) for details].

Simulations of the Fresh-Ice–Fresh-Water System

To simulate the fresh-ice–fresh-water system, I integrate the evolution equations, Eq. (2.5), with the buoyancy based on the simplified density function, Eq. (2.6). It is convenient to express the buoyancy in terms of the control parameter χ_m.

$$\chi_m\left(T_\infty\right) = \chi\left(T = T_m, T_\infty\right) = \frac{T_m - T_\infty}{T_{\text{ice}} - T_\infty}. \tag{2.10}$$

This control parameter bi-uniquely describes the far-field temperature of the system, T_∞. One could also argue χ_m describes the fraction of the temperature range $(T_{\text{ice}} - T_\infty)$ that is responsible for the occurrence of the buoyancy reversal instability. To obtain the buoyancy expression in terms of χ_m, I also give the

temperature, T, as normalised deviation from the far-field temperature:

$$\chi\left(T, T_\infty\right) = \frac{T - T_\infty}{T_\mathrm{ice} - T_\infty}. \tag{2.11}$$

The normalised temperature, χ, then varies between 0 in the far field and 1 at the interface.

With χ, the buoyancy of the fresh-ice–fresh-water system can be given as

$$b = b_\mathrm{m}\ \chi\left(2\chi_\mathrm{m} - \chi\right)\chi_\mathrm{m}^{-2}, \tag{2.12}$$

where the minimum buoyancy is

$$b_m = g\frac{\alpha T_m^2}{\rho\left(T_\infty\right)}\frac{\chi_m^2}{\left(1-\chi_m\right)^2}, \qquad g\frac{\alpha T_m^2}{\rho\left(T_\infty\right)} \approx -1.1 \times 10^{-4}\ \mathrm{m\ s^{-2}}. \tag{2.13}$$

I simulate systems of different far-field temperatures T_∞ (cf. Table 2.1). For the idealised setup, I study the system of $T_\infty = 2\ T_\mathrm{m}$ ($\chi_m = 0.5$) and three systems of both higher and lower buoyancy at the interface. In addition, I perform three numerical simulations with altered flow boundary conditions to study the influence of melt water on the flow.

The final boundary-layer height of the simulated systems, z_*, is between 0.12 m and 1.05 m. These sizes are comparable to the size of the laboratory tank of 0.347 m. The Reynolds numbers $\frac{w_* z_*}{\nu}$ and $k^2/\left(\varepsilon\nu\right)$ are about 900 and 100, with the turbulent kinetic energy k, the viscous dissipation rate ε, the convective velocity scale, w_* and the viscosity ν.

χ_m	Ri_0	T_∞ [°C]	b_m [m s^{-2}]	Colour	z_* [m]	$\frac{w_* z_*}{\nu}$	$\frac{k^2}{(\varepsilon\nu)}$	$w_{\mathrm{rms}}^{\mathrm{max}}/w_0$	z_0 [mm]	w_f [mm d^{-1}]
0.152	31	4.69	3.6×10^{-5}		1.05	950	190	0.81	39	42
0.179	21	4.85	0.5×10^{-4}		0.96	990	190	0.87	31	58
0.232	11	5.18	1.0×10^{-4}		0.86	1100	200	0.95	21	90
0.500	1	7.96	1.1×10^{-3}		0.37	900	140	1.03	5.6	400
0.586	0.5	9.61	2.2×10^{-3}		0.29	820	120	1.01	4.0	610
0.760	0.1	16.57	1.1×10^{-2}		0.15	670	87	0.94	2.0	1700
1.000	0	T_∞	$b_m\,(T_\infty)$		-	531	34	-	-	$w_f\,(T_\infty)$
0.500[f]	1	7.96	1.1×10^{-3}	-	0.39	960	140	1.04	5.6	390
0.841[*,f]	0.04	25.00	3.1×10^{-2}	-	0.14	850	88	0.99	1.3	3200
0.901[*,f]	0.01	40.00	0.9×10^{-1}	-	0.12	1000	85	1.01	0.9	6700

Table 2.1: Properties of the numerical simulations of the fresh-ice–fresh-water system. The first four columns equivalently define the simulation. They are the far-field temperature parameter χ_m, the Richardson number Ri_0, far-field temperature T_∞ and minimum buoyancy b_m (cf. Eqs. (2.13, 2.10, 4.18)). The colour column gives the colour assigned to the simulation throughout the whole work. The following four columns, characterise the turbulent system in its stage of final simulation time. The boundary-layer height z_* and the convective velocity scale w_* are defined in Eq. (4.4) and Eq. (4.5), respectively. The turbulent Reynolds number $\mathrm{Re}_{\mathrm{turb}}$ is the maximum value of $e^2/(\varepsilon\nu)$ in the domain with turbulent kinetic energy k, viscous dissipation rate ε and viscosity ν. $\mathrm{Re}_{\mathrm{turb}}$ and $w_* z_* \nu^{-1}$ are measures for the scale separation in the simulations. The diffusive velocity scale $w_0 = (z_0\, b_m)^{1/2}$ with the diffusive length scale z_0 is defined in Eq. (4.3). The last two columns, the diffusive length scale and the melt rate of the fresh-ice–fresh-water interface, w_f, Eq. (4.12), are results of the simulation and analysis. The regular grid size of the simulations is $1280 \times 1280 \times 576$. (f) marks simulations with background mean advection; (*) marks simulations of smaller size $512 \times 512 \times 576$ points.

Simulations of the Sea-Ice–Sea-Water System

To simulate the sea-ice–sea-water system, I integrate the evolution equations, Eq. (2.5), based on a linear buoyancy parameterisation—linear in temperature and linear salinity. This buoyancy parameterisation is established from the density function of sea water, Eq. (2.2), in the appendix A.1 and reviewed in A.2. As explained along with the introduction of Eq. (2.9), instead of focusing on the precise density formula, I will use the Richardson number, Ri_0, to study the sea-ice–sea-water system based on the striking features of the buoyancy function: the interfacial buoyancy and the minimum buoyancy, b_m.

$$\frac{b}{b_m} = -\mathrm{Ri}_0\ \sigma + \theta. \tag{2.14}$$

To avoid confusion between the fresh-ice–fresh-water system and the sea-ice–sea-water system, the distinct symbols, θ and σ, will be used here to represent the normalised temperature and normalised salinity:

$$\theta = \frac{T - T_\infty}{T_\mathrm{ice} - T_\infty}, \tag{2.15a}$$

$$\sigma = \frac{S - S_\infty}{S_\mathrm{ice} - S_\infty}. \tag{2.15b}$$

In analogy to the fresh-ice–fresh-water system, b_m, defines the minimum buoyancy in the parameter space. b_m occurs when fluid of far-field salinity, S_∞, is cooled to the interfacial temperature, T_ice, (cf. Eq. (2.8)). For $\mathrm{Ri}_0 \geq 5$, the approximation yields deviations from the real buoyancy smaller than 0.06 b_ice and smaller than about 0.2 b_m in the relevant section of the parameter space (cf. appendix A.1). This approximation of b is sufficient to reproduce the buoyancy reversal instability that leads to overturning of the system.

I am particularly interested in simulations of the sea-ice–sea-water system of $\mathrm{Pr} = 13.8$ and $\mathrm{Le} = 176$ that resembles ocean-like fluids (Steele, Mellor and Mcphee, 1989). The available computational resources, however, constrain my investigations to $\mathrm{Pr}\times\mathrm{Le} = 40$. The smaller I choose Pr, the larger the Le that I can simulate.

I study one system of $\mathrm{Pr} = 10$, $\mathrm{Le} = 4$, and $\mathrm{Ri}_0 = 10$ on a $1280^2 \times 1152$ grid (cf. Table 2.2). $\mathrm{Le} = 4$ is the largest diffusivity ratio κ_T/κ_S for which turbulence is still fully resolved on diffusive scales in a water-like fluid of $\mathrm{Pr} = 10$. I further study the behaviour of systems with different far-field temperatures T_∞ with $\mathrm{Pr} = 1$, $\mathrm{Le} = 4$, and $\mathrm{Ri}_0 \in \{1, 2, 5, 10, 100\}$ on a $512^2 \times 576$ grid. And I study the behaviour of systems of different Le with $\mathrm{Pr} = 1$, $\mathrm{Le} \in \{2, 4, 10\}$, and $\mathrm{Ri} = 2$ on a $512^2 \times 576$ grid.

The size of the simulated systems is between 0.09 m and 0.19 m and thus almost an order of magnitude smaller than the simulations of the fresh-ice–fresh-water systems. The Reynolds numbers $\frac{w_* z_*}{\nu}$ and $k^2/(\varepsilon\nu)$ are about 5×10^2 and 2×10^2, with the turbulent kinetic energy k and the viscous dissipation rate ε.

Pr	Le	Ri_0	R_ρ^s	T_∞ [°C]	b_m [m s^{-2}]	Colour	z_{est} [m]	$\frac{w_* z_{\mathrm{est}}}{\nu}$	$\frac{k^2}{(\varepsilon\nu)}$	$\frac{\delta_s}{z_0'}$	w_s [mm d^{-1}]
10	4	11	-6.4	16.4	2.6×10^{-2}	■	0.16	390	42	1.69	18
01*	4	1	-0.86	77.8	2.7×10^{-1}	■	0.09	1200	310	2.68	620
01*	4	2	-1.14	47.9	1.35×10^{-1}	■	0.14	1100	340	6.79	170
01*	4	5	-2.9	27.0	0.53×10^{-1}	■	0.14	610	140	11.1	40
01*	4	10	-6.1	17.3	2.6×10^{-2}	■	0.13	400	110	11.7	19
01*	4	100	-81	2.9	2.0×10^{-3}	■	0.19	140	25	9.39	1
01*	2	2	-1.14	47.9	2.6×10^{-2}	-	0.10	960	260	2.5	160
01*	10	2	-1.14	47.9	2.6×10^{-2}	-	0.14	1300	330	12	190

Table 2.2: Properties of the numerical simulations of the sea-ice–sea-water system. The set of the first three columns uniquely define the system. They are the Prandtl number Pr, Lewis number Le, and Richardson number Ri. The reader can obtain the far-field temperature, T_∞, and the far-field salinity, S_∞, corresponding to the simulations from Figure 5.14 and Figure 5.15. For his convenience, T_∞ and the minimum buoyancy, b_m, are given for an assumed far-field salinity of $S_\infty = 34$ g kg^{-1}. The density ratio, $R_\rho^s = \beta\,(S_\infty - S_{\mathrm{ice}})\,\alpha^{-1}(T_\infty - T_{\mathrm{ice}})^{-1}$, is a commonly used system-describing parameter and is provided here to compare this work to other studies. The far-field values $S_\infty = 34$ g kg^{-1} and T_∞ have been used as a reference to determine the thermal expansion coefficient, α, and the saline contraction coefficient, β. The colour column gives the colour assigned to the simulation throughout the whole work. They are chosen such that they match the colour of the fresh-ice–fresh-water simulation of corresponding Richardson number (with the exception of the simulation of Pr = 10). The columns 6–8 characterise the turbulent system in its stage of final simulation time. The simulations reach a boundary layer height, z_{est}, [cf. Eq. (5.5)] of about 0.15 m, and a turbulence intensity, $\frac{w_* z_{\mathrm{est}}}{\nu}$, of about 5×10^2, and $Re_{\mathrm{turb}} = k^2/(\varepsilon\nu)$ of about 2×10^2, with turbulent kinetic energy k, viscous dissipation rate ε and viscosity ν. The convective velocity scale, w_*, is defined in Eq. (4.5). The last two columns are results of the simulation and analysis. The diffusive length scale z_0, [cf. Eq. (5.3)] describes the observed salinity gradient thickness, δ_s, to order one. w_s are the melt rates observed from the simulations. For the simulations of $Pr = 1$, w_s has been multiplied by $10^{1/3}$ to give presumable melt rates for the corresponding Pr = 10 case. The grid size of the simulations at Pr = 10 is $2560\times1152\times2560$ with an aspect ratio of 3.33:1. The grid size of the simulations at Pr = 1 (*) is $512\times576\times512$ with an aspect ratio of 1.33:1.

Chapter 3

Measurements of the Melt Rate in the Fresh-Ice–Fresh-Water System

The main objective of the laboratory experiments is to review if they can be represented by direct numerical simulations. In its core, the question encompasses whether or not the physical model involved in the direct numerical simulation is valid. The laboratory experiment has therefore been developed along the setup of the direct numerical simulation. The one-to-one comparison allows me to review that all relevant aspects of the physics are captured.

From the physical model, the freely developing system is expected to mix diffusively for $T_\infty < T_m$ and mix turbulently for $T_\infty > T_m$. First, I assess how well the diffusively mixing system is represented in the laboratory (section 3.1). The precision, to which the diffusively mixing laboratory system laboratory follows the theory, benchmarks the laboratory setup. Second, I assess the capability of the laboratory setup to temporally resolve the turbulently mixing system, and its capability to detect thermal changes that result from the mixing (section 3.2).

Then, the turbulent evolution of the laboratory system is compared to the one of the numerical system. The assessment of the validity of the physical model is achieved in two ways: First, by comparing the temporal evolution of the mean-temperature profiles of the laboratory system and the numerical system (section 3.2.3). Second, by comparing the melt rates of both (section 3.3).

3.1 Diffusive-Mixing Experiments

A diffusive-mixing laboratory experiment of the fresh-ice–fresh-water system should follow the evolution equations, Eq. (2.5), for neglected advection terms.

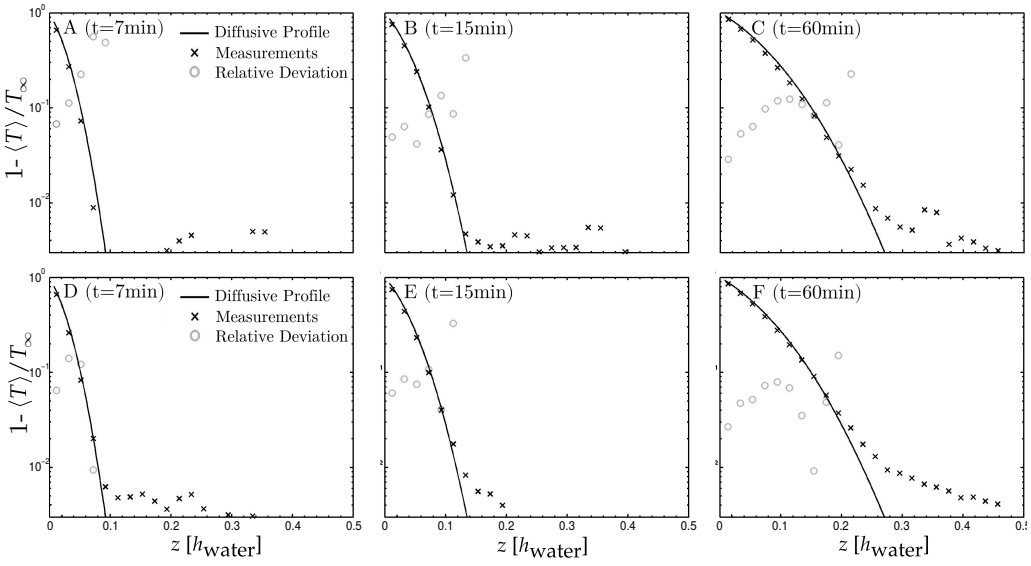

Figure 3.1: The profile of the normalised temperature, $\chi = 1 - \langle T \rangle / T_\infty$, of the diffusive laboratory experiments. It varies between 1 at the ice interface ($z = 0$) and 0 in the far field ($z = 0.5 h_{\mathrm{water}}$). Temporal evolution of a single vertical temperature profile for $T_\infty = 3.0$ ℃. Profiles are given after an evolution time of a) 7 minutes, b) 15 minutes, and c) 60 minutes. Next to the interface, thermistor measurements (crosses) generally deviate from a theoretical error-function profile (solid) by less than 10% (circles). Away from the interface, thermistor measurements deviate by about 10^{-2} $(T_\infty - T_{\mathrm{ice}})$ from the theoretical error-function profile. d,e,f) same as (a,b,c) but $T_\infty = 3.5$ ℃.

A diffusive-mixing numerical experiment of the fresh-ice–fresh-water system rigorously does so for the particular boundary and initial conditions. The solution to the numerical experiment is a zero velocity field and a growing error function in the vertical mean-temperature profile. Here, I present two diffusive laboratory realisations, one for $T_\infty = 3.0$ °C (cf. Figure 3.1a,b,c) and one for $T_\infty = 3.5$ °C (cf. Figure 3.1d,e,f), to obtain the solution of the laboratory experiment for the mean-temperature profile.

Over the course of these two laboratory runs, the ice bottom melts and the distance between the melting ice bottom and the thermistor cascade grows. A considerable ablation of the ice bottom is only observed after an experimental run time of hours. The ice had ablated by 2 mm after two hours, while the far-field temperature remained unaffected to within less than 1%.

I compare the temperature profile from the diffusive-mixing laboratory experiment to an error-function profile that takes the growing distance between melting-ice bottom and thermistor cascade into account. The measurement by each thermistor is normalised by its own maximum temperature that is found throughout the experiment realisation. I give the relative deviation with respect to the theoretical curve.

In both realisations, the thermistor measurements (crosses) do follow the theoretical error-function profile (solid) to within an accuracy of 10% (circles) next to the interface. Away from the interface, there should not be any temperature deviations from T_∞ if the experimental realisation were perfect. Here, the noise level of the temperature measurements is about 10^{-2} $(T_\infty - T_{\mathrm{ice}})$ for the measurement of $T_\infty = 3.0$ °C (cf. Figure 3.1a,b,c). For the measurement of $T_\infty = 3.5$ °C the temperature deviations away from the interface clearly exhibits a pattern (cf. Figure 3.1f). The pattern suspiciously resembles that of slight convective motion. The motion has likely been induced from a temperature difference between the cold room and the water body.

Any mean-temperature signal that shall be attributed to convection induced by the ice interface in the following laboratory experiments has to be compared to the described temperature noise level of 10^{-2} $(T_\infty - T_{\mathrm{ice}})$.

3.2 Turbulent-Mixing Experiments

3.2.1 Laboratory Realisation

I conduct several laboratory realisations to investigate the principle behaviour of the laboratory setup for varying far-field temperatures, $T_\infty > T_m$. Once the far-field temperature, T_∞, surpasses the temperature of maximum density, T_m, the stable stratification of the system is lost. Then, the system features a buoyancy reversal instability instead and becomes convectively unstable.

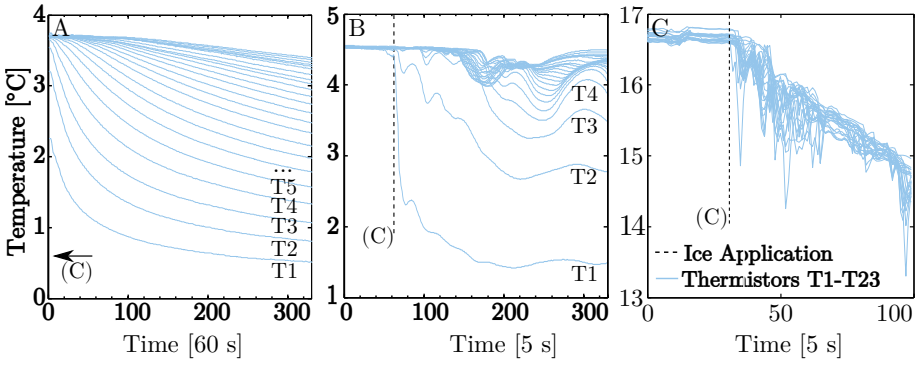

Figure 3.2: Temporal evolution of the thermistor measurements in a single realisations of a) $T_\infty = 3.7$ ℃, b) $T_\infty = 4.6$ ℃, and c) $T_\infty = 16.4$ ℃. (C) marks the application of the ice to the water body.

The comparison of the temporal evolution of the thermistor measurements in a single realisations of $T_\infty = 4.5$ ℃ to one of $T_\infty = 17$ ℃ shows that the flow evolves too quickly compared to the response time of the thermistors when T_∞ is chosen too high (cf. Figure 3.2). Then, all 23 thermistors simultaneously measure a continuous temperature drop: The system has completely overturned and yields a new mean temperature after about half a minute. That corresponds to five thermistor-cascade measurements and the temporal evolution is not resolved anymore. So, a suitable far-field temperature that allows me to sample the flow evolution with a decent amount of measurements lies on the lower end of the temperature range given by these two realisations.

The comparison of a turbulent-laboratory-experiment ensemble of $T_\infty = 4.35$ ℃ to the diffusive runs exhibits systematic deviations between their mean-profiles (cf. Figure 3.3). At the interface, the mean temperature gradient is increased in the turbulent ensemble compared to the diffusive run. Away from the interface, a constant mean-temperature level prevails that differs systematically from the far-field temperature, T_∞. These differences are the turbulent signal in this laboratory experiment. In the diffusive run on the contrary, the mean-temperature profile away from the interface varies more randomly (cf. Figure 3.1).

The turbulent signal in the far field is, however, only of the order of the noise level, 10^{-2} $(T_\infty - T_{\mathrm{ice}})$. The turbulent signal will increase with increasing turbulence intensity. From the two opposing requirements on the laboratory experiment, to use

(i) a high far-field temperature to comply with the temperature resolution of the thermistor measurements, and to use

(ii) a low far-field to comply with the temporal resolution of the thermistor cascade,

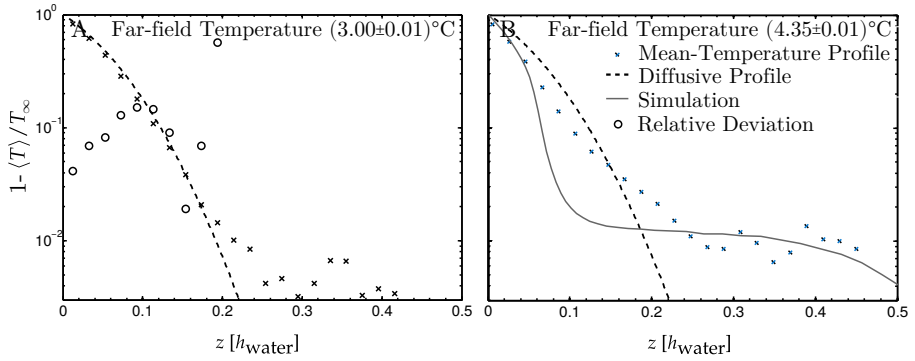

Figure 3.3: The profile of the normalised mean-temperature, $\chi = 1 - \langle T \rangle / T_\infty$, (crosses) after a experiment run time, Δt, of 40 minutes for a) $T_\infty = 3.00$ ℃, and b) $T_\infty = 4.35$ ℃. (a) is taken from the same experiment as Figure 3.1b. The profile pattern in (b) seems to systematically deviate from the diffusive profile (dashed). It follows the simulation (solid) behaviour. It is still similar to that of the diffusive setup shown in Figure 3.1f.

educated guessing suggests $T_\infty = 5.00$ ℃ as a reasonable compromise.

I record an ensemble of 25 realisations at $T_\infty = 5$ ℃ and $\Delta t = 15$ min to capture the evolution of the mean-temperature profile of the turbulent system (cf. Figure B.3).

3.2.2 Numerical-Simulation Realisation

I record an ensemble of 25 tower measurements from one simulation at $T_\infty = 4.975$ ℃ ($\chi_m = 0.20$) to capture the evolution of the mean-temperature profile of the turbulent system (cf. Figure B.4). The simulation grid needed to resemble a laboratory tank of domain size 0.360 m is just $512 \times 512 \times 192$ grid points, with an aspect ratio of four to one. 256 base locations equally distribute within a horizontal cross-section of 512×512 grid points to obtain tower measurements. The tower measurement consists of the temporal evolution of the vertical temperature profile beneath the ice interface at the base locations, just as does a laboratory ensemble member.

3.2.3 Assessment

I compare the ensemble of 25 laboratory realisations of $T_\infty = (5.00 \pm 0.01)$ ℃ to the simulation of $T_\infty = 4.975$ ℃ ($\chi_m = 0.20$). First, I qualitatively compare the phenomena obtained from laboratory realisations with dyed ice and simulation visualisations. Second, I quantitatively compare the temporal evolution of both the mean behaviour and individual tower data of laboratory experiment and simulation.

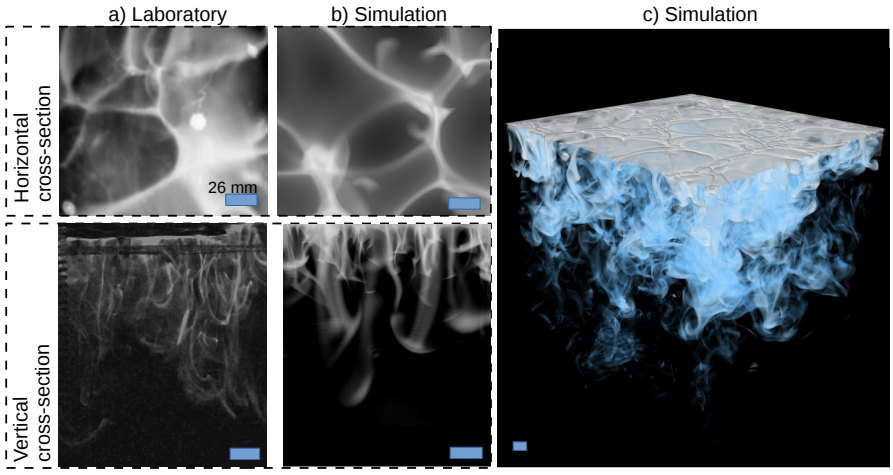

Figure 3.4: Structure of the flow as retrieved from laboratory tank experiment (a) and simulation (b,c). Bright fluid indicates a low temperature compared to the temperature of the dark warmer surrounding fluid. The blue dash in all of the visualisations indicates the diffusive length scale of 26 mm. Dashed boxes contain a horizontal (upper box) and vertical cross-section (lower box). A visualisation of the temporal evolution of (c) can be found in Keitzl, Notz and Mellado (2014). Note: The horizontal cross-sections of the laboratory tank experiment visualise a substituting setup in which—for visualisation purposes—a constant-temperature cooling plate is used instead of ice.

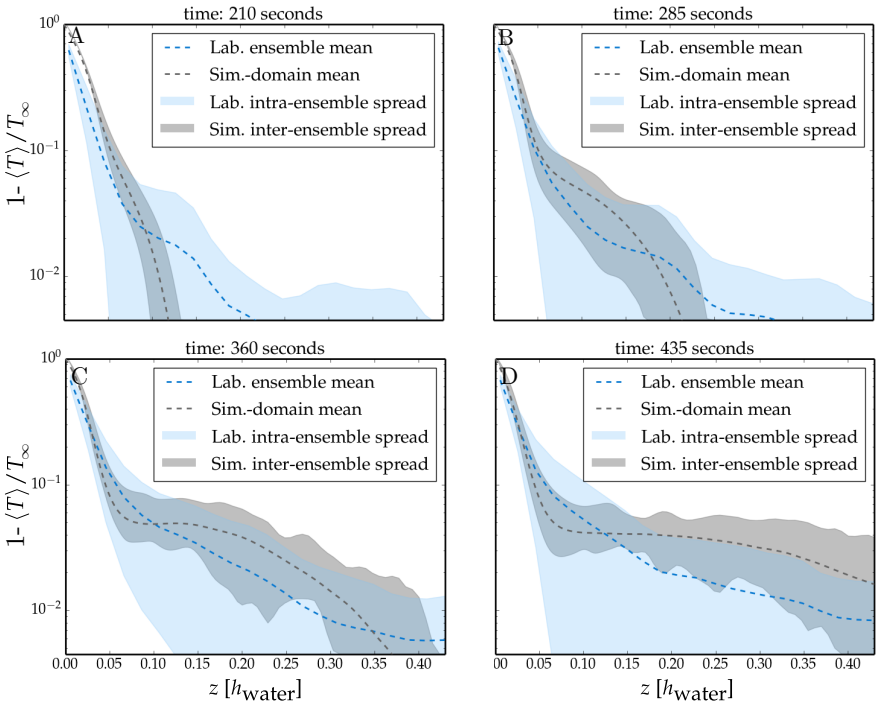

Figure 3.5: The profiles of the normalised mean-temperature, $\chi = 1 - \langle T \rangle / T_\infty$, of the laboratory ensemble (blue) and the simulation-data ensemble (grey) for $T_\infty = 5$ ℃ after a) 210 s, b) 285 s, c) 360 s, and d) 435 s. The standard deviation around the means is given to indicate as the spread of the individual ensemble members (shaded areas).

Qualitatively, the structure of the boundary layer beneath the ice in the laboratory matches the one in the simulation (cf. Figure 3.4). Cold fluid (bright) unites more mass per volume and congregates to thin streaks that push downward through warmer surrounding fluid (dark). The lowermost point of the streaks is marked by a plume-like tip structure with vortexes at their sides. Looking at the horizontal cross-section, a honeycomb pattern is seen for both laboratory experiment and numerical simulation. From the comparison of vertical and horizontal cross-sections, one observes that plumes actually form the septum of the honeycomb cells. Cold plumes push down along the cell rim while fluid must consequently move up in the interior of the cell. Plumes are the dominant structures. Their movement and diffusive decay mixes the water beneath the ice in the so called 'mixed layer'. The mixing successively entrains calm, warmer water from below and the colder mixed layer broadens. Both laboratory experiment and simulations exhibit this working principle, known from the convective boundary layer in the atmosphere (Stull, 1988), but vertically inverted, and from Rayleigh-Bénard convection (Chillá and Schumacher, 2012).

Quantitatively, the time evolution of temperature profiles of individual laboratory

ensemble members, as well as that of individual tower data from the simulation, vary strongly among each other. Hence, I draw the comparison on the basis of the mean-temperature profiles instead of on the basis of laboratory ensemble member and individual tower data from the simulation.

The mean profiles evolve as described in the previous paragraph: A mixed layer develops and broadens in time. The broadening happens at the same pace in the laboratory experiment as in the simulation (Figure 3.5) and takes about 7 minutes to cover a height of 0.40 h_{water}, with the water height h_{water}. In the mixed layer, the mean temperature is almost constant in time. At the interface, $\langle\chi\rangle$ decreases by an order of magnitude over a distance of $\sim 0.05\ h_{\text{water}}$ for both laboratory and simulation. This region forms part of what is generally referred to as 'the surface layer'.

Differences between laboratory experiment and simulation exist in the boundary conditions, the initial conditions and the system itself. Regarding the boundary conditions, the lateral boundary of the numerical experiment is periodic in $\mathbf{e}_1$ and $\mathbf{e}_2$, whereas the laboratory tank walls impose no-penetration conditions. The tank walls also allow for additional heat exchange if the surrounding temperature is not matched perfectly. The horizontal bottom boundary of the numerical experiment is far from the turbulent region and the flow develops freely. A ground plate of a certain heat capacity limits the flow in the laboratory instead. The comparison is therefore only carried out as long as the fluid motion is no affected by the motion redirected by the bottom boundary. Regarding the initial conditions, the numerical experiment manifests instabilities half a minute later than for those of the laboratory experiment, because kinetic energy remains from the laboratory preparations. The need to initiate a thermally equilibrated water-body temperature opposes the prerequisite of the water being motionless. The longer a timespan the system is given to lose its turbulent kinetic energy acquainted from mixing to yield a homogeneous initial temperature, the more it stratifies due to a heat flux through the tank top where the ice awaits its employment. Regarding the setups, they differ in the presence of the thermistor cascade and its response time in the laboratory. The main issue when comparing temperature profiles is the presence of the measuring device itself. The device is not negligibly small in relation to the size of the tank and imposes no-slip conditions across its surface which alters the movement of the flow.

K–S Test

To test the agreement between the laboratory experiment and the numerical simulations, I perform a Kolmogorov–Smirnov test on the mean profiles with the following null hypothesis: The laboratory measurements and simulation tower data are drawn from the same distribution. I cannot reject the null hypothesis on a significance level of 5% for the regions indicated by the grey bars in Figure 3.6a. The laboratory measurement and tower data can thus be considered as

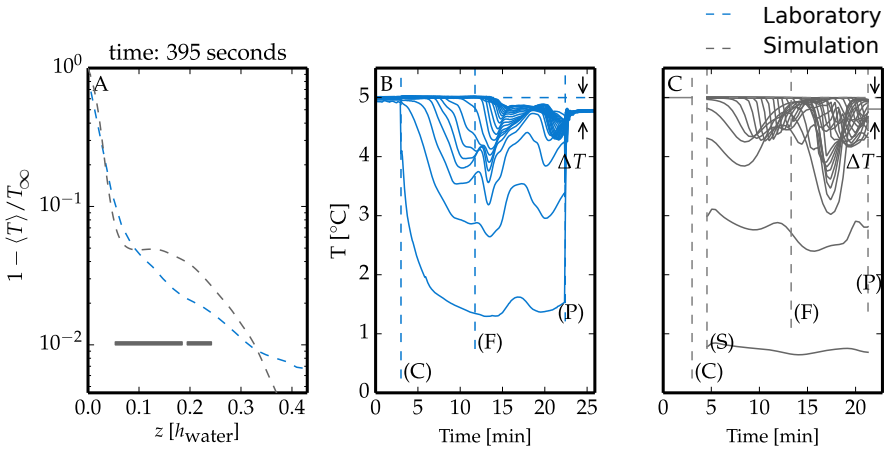

Figure 3.6: Comparison of laboratory (blue) and simulation (grey) temperature profiles. a) The laboratory temperature profile (blue dashed line) is averaged over 25 realisations after equal elapsing time of seven minutes. The simulation temperature profile (grey dashed line) is averaged over the complete horizontal plane. The grey bars below the profiles indicate regions of quantitative agreement between laboratory experiment and simulation. In these regions, the nullhypothesis cannot be rejected that the laboratory ensemble of 25 members and the mean profile of the simulation are drawn from the same distribution with a Kolmogorov–Smirnov test. b) Temporal evolution of one realisation of a temperature-profile measurement taken from the laboratory. (C) marks the time of ice–water contact, (F) the time when fully developed turbulence approximately starts and (P) the time of external mixing with a pump. After (P), I find a temperature difference ΔT of the averaged mean-temperature profile with respect to the temperature prior to the experimental conduct. c) Same as (b), taken from the simulation. (S) marks the starting time of the simulation.

statistically equivalent in those regions. The regions broaden with evolving time and stretch from close to the interface to roughly half of the mixed layer.

In summary, I find qualitative and quantitative agreement between laboratory experiment and simulation given the number of laboratory ensemble members. Both experiments and simulations are used in the following section to investigate the melt rate of the ice.

3.3 The Melt Rates

Ice melts if more internal-energy per area and time, H_{water}, is supplied to the ice interface than can be transported away, H_{ice}. I focus on an isothermal ice block with $H_{\text{ice}} = 0$ W m^{-2}. The melt rate w_f is hence solely determined by H_{water}.

$$w_f = \frac{1}{\rho_{\text{ice}} L} H_{\text{water}} \tag{3.1}$$

$L = 333.5$ kJ kg^{-1} is the specific energy required to melt the ice (Frankenstein and Garner, 1967) and $\rho_{\text{ice}} = 916.8$ kg m^{-3} is the density of pure ice at 0℃ (Pounder, 1965). The internal-energy flux at the ice interface, H_{water}, originates from the evolution of the internal energy in the fluid system. The mean evolution of the internal energy, Eq. (2.5c), is

$$\partial_t \langle T \rangle (z,t) = -\frac{1}{\rho_{\text{water}} c_p} \partial_3 H (z,t) , \tag{3.2}$$

with

$$H (z,t) = -\rho_{\text{water}} c_p \left(\kappa_T \partial_3 \langle T \rangle (z,t) - \left\langle \upsilon_3' T' \right\rangle (z,t) \right) . \tag{3.3}$$

The specific heat capacity of water is $c_p = 4.22$ kJ kg^{-1} K^{-1}; the thermal diffusivity of water is $\kappa_T = 1.36 \times 10^{-7}$ m^2 s^{-1} at 273.15 K (Sharqawy, Lienhard and Zubair, 2010) and $\rho_{\text{water}} = \rho (T_\infty)$.

3.3.1 Melt Rates Observed in the Laboratory Experiment

From the laboratory bulk measurements, I evaluate the melt rates from an approximation of the energy-flux, H_{water}, based on the net change of the internal energy, ΔE_{int} and the run time, Δt.

$$H_{\text{water}} \approx \rho_{\text{water}} c_p \kappa_T \Delta E_{\text{int}} / \Delta t \tag{3.4}$$

The net change of the internal-energy, ΔE_{int}, has been converted to heat of fusion $E_{\text{Lat}} = m_{\text{ice}} L$ and to internal energy of the melt water $E_{\text{mw}} = m_{\text{ice}} c_p (T_{\text{end}} - T_{\text{ice}})$.

From the integral formulation of Eq. (3.2) one obtains the internal-energy balance of the system,

$$\Delta E_{\text{int}} = m_{\text{water}} c_p \left(T_{\text{end}} - T_\infty\right) = E_{\text{Lat}} + E_{\text{mw}} = m_{\text{ice}} L + m_{\text{ice}} c_p \left(T_{\text{end}} - T_{\text{ice}}\right), \tag{3.5}$$

with the mass of the melted ice, m_{ice}, and the mass of water in the tank, m_{water}.

From Eq. (3.5), from the approximation that water and ice share the same base area A, from $m_{\text{ice}} = \rho_{\text{ice}}\ h_{\text{ice}}\ A$ and from $m_{\text{water}} = \rho_{\text{water}}\ h_{\text{water}}\ A$, the height h_{ice} of the melted ice is given as

$$h_{\text{ice}} = h_{\text{water}} \frac{\rho_{\text{water}}}{\rho_{\text{ice}}} \frac{c_p \left(T_\infty - T_{\text{end}}\right)}{L + c_p \left(T_{\text{end}} - T_{\text{ice}}\right)}. \tag{3.6}$$

Several laboratory experiments for the same temperature T_∞, but with different run time Δt, allow to estimate a melt rate $w_f = \Delta h_{\text{ice}}/\Delta t$ from the data. This assumes a constant energy flux at the interface, which is well known for free-convection systems and which I observe for all our simulations (presented in section 4.3). The standard deviation among the calculated heights at each Δt is up to 13 %. I obtain the melt rates $w_{\text{f}} = [53,\ 55,\ 136,\ 1260]$ mm d^{-1} for $T_\infty = [4.5,\ 5,\ 6,\ 14.8]$ ℃ within the error bounds supplied in Figure 3.8 (crosses and black solid bars).

I compare these melt rates w_f to melt rates w_d in a purely diffusive laboratory experiment of similar boundary-layer height $\delta = 0.40\ h_{\text{water}}$ (dotted line). An error-function profile in $T_d\left(z\right)$ and δ defined by $\langle T_d\left(z=\delta\right)\rangle / T_\infty = 0.995$ yield

$$w_{\text{d}} = \frac{\rho_{\text{water}}}{\rho_{\text{ice}}} \frac{c_p}{L} \kappa_T\ \partial_3 \left\langle T_d \right\rangle|_\delta = \frac{\rho_{\text{water}}}{\rho_{\text{ice}}} \frac{c_p T_\infty}{L} \frac{\kappa_T}{\delta} \left(\frac{2\ \text{erf}^{-1}\left(-.995\right)}{\sqrt{\pi}} \right) \tag{3.7}$$

I find that the melt rates w_f are increased by one to two orders of magnitude compared to w_d (Figure 3.8b,c), in contrast to the increase by a constant factor of about two reported in Martin and Kauffman (1977). I will elaborate on this finding in section 5.1.

3.3.2 Melt Rates Simulated in the Numerical Experiment

In the simulation, I evaluate the melt rates from the horizontally averaged energy flux H_{water} according to Eqs. (3.1,3.3). At the interface ($z = 0$) one finds

$$H_{\text{water}} \equiv H\left(z,t\right)|_{z=0} = -\rho_{\text{water}} c_p \kappa_T \partial_3 \left\langle T \right\rangle. \tag{3.8}$$

I obtain melt rates for several simulations of varying far-field temperature (Table 2.1, Figure 3.8a, dots). From temperatures $T_\infty = 3.98$ ℃ to $T_\infty = 5.20$ ℃, melt rates increase strongly from diffusive values of 11 mm d^{-1} (dashed line) up to 86 mm d^{-1} (Figure 3.8b, blue dot). From temperatures of $T_\infty = 17$ ℃ to

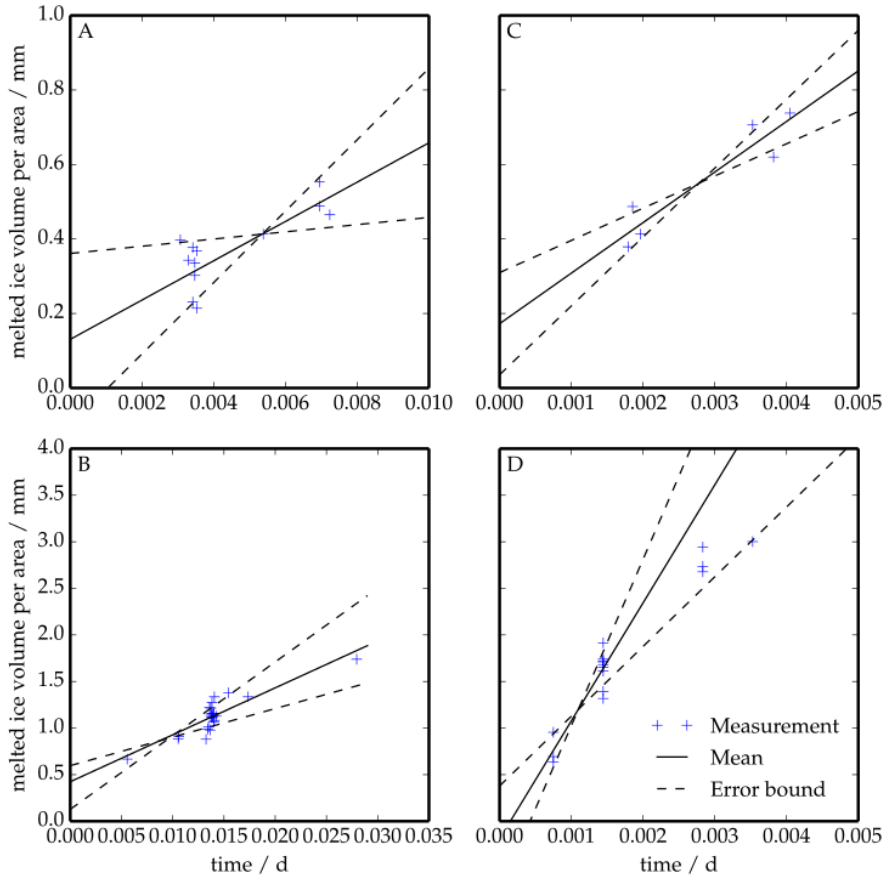

Figure 3.7: Energy-flux, H_{water}, approximation from the net change of the internal energy, ΔE_{int} and the run time, Δt, from laboratory experiments of same T_∞. a) $T_\infty = 4.5$ ℃, b) $T_\infty = 5.0$ ℃, c) $T_\infty = 6.0$ ℃, and d) $T_\infty = 14.9$ ℃.

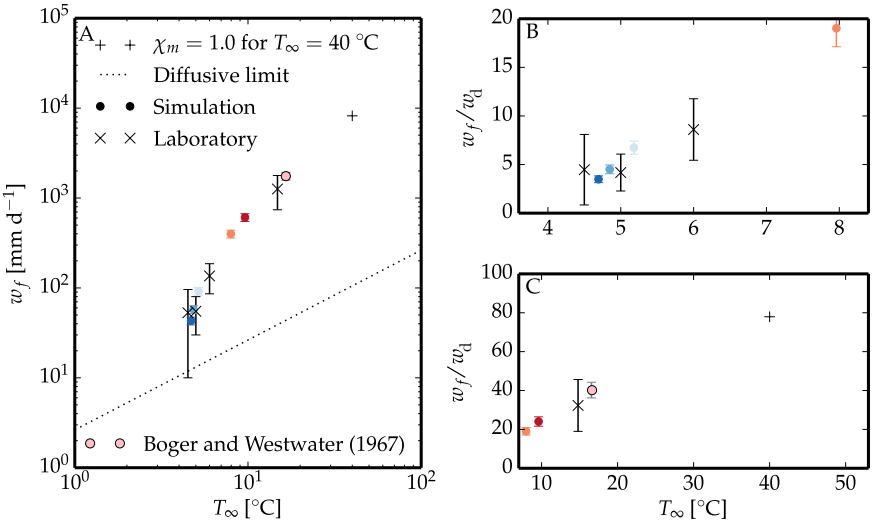

Figure 3.8: Melt rate derived from scalar gradient at the interface (simulation, coloured dots corresponding to Figure 2.1) and derived from bulk-temperature change (laboratory, crosses). Diffusive melt rates, w_d, as given in Eq. (3.7) (dotted line). (a) Double logarithmic plot illustrates the power-law change over the full temperature range. (b) Linear plot illustrates the melt-rate enhancement in the low-temperature range. (c) Linear plot illustrates the melt-rate enhancement in the high-temperature range.

$T_\infty = 40$ ℃, melt rates increase from 1.7 m d^{-1} to 7 m d^{-1} (Figure 3.8c, grey dot and plus). These meltrates agree quantitatively with those observed in the laboratory.

The relative error of the melt rates from the simulation is less than 10% due to varying initial conditions (Mellado, 2012).

The simulation of $\chi_m = 1$ cannot be assigned to a definite far-field temperature. If the far-field temperature increases, χ_m approaches 1 asymptotically (cf. Eq. (2.10)). $\chi_m = 1$ is the limit of high far-field temperatures. Just in this limit the buoyancy reversal vanishes entirely (Figure 2.1, dotted line) and I find the minimum buoyancy directly at the wall. This situation is reminiscent of the free convection over a heated plate (Mellado, 2012), where buoyancy decreases linearly with the stratifying agent from the maximum value at the wall to the far-field. I provide the melt rate derived from this simulation ($\chi_m = 1$) exemplarily for a far-field temperature of $T_\infty = 40$ ℃ for which I expect the assumption of negligible buoyancy reversal to be sufficiently good approximation (Figure 3.8, plus).

3.3.3 Melt Rates Observed by Boger and Westwater (1967)

Boger and Westwater (1967) experimentally investigated the effect of buoyancy on top and bottom melting in a $0.05 \times 0.0127 \times 0.0127$ m^3 test chamber. Among mostly bottom-freezing and top-melting experiments they conducted one bottom-melting experiment labeled “12V” with buoyancy reversal just as considered in this work. I briefly present their setup and result to compare it properly to the melt rates obtained so far.

They set the temperatures of the bottom and the top of an laterally isolated test chamber that is filled with water. The top of the test chamber is held at -38.4 ℃ and ice forms. The bottom of the test chamber is set to 24.9 ℃ once the experiment starts. They provide the measured interface velocities and time series of three thermocouple measurements, one in the ice and two in the water beneath.

From their interface velocities v_m between 2×10^{-4} cm s^{-1} to 1×10^{-4} cm s^{-1} and the corresponding thermocouple measurement in the ice, a heat flux in the water of about

$$H_\text{water} = Q_\text{Lat} + H_\text{ice} = \rho_\text{ice} L v_m + k_\text{ice} \frac{\mathrm{d}T}{\mathrm{d}z} \approx 3.06 \frac{\text{kW}}{\text{m}^2} + 3.01 \frac{\text{kW}}{\text{m}^2} \tag{3.9}$$

can be estimated. This heat flux corresponds to a melt rate of 1700 mm d^{-1} if the ice were isothermal (cf. Figure 3.7, pink).

From their thermocouple measurement in the water beneath the ice at position $z = 1.402$ cm and $z = 2.339$ cm, the far-field temperature can be estimated with an error function fit (cf. Figure 3.9a). An educated guess for the far-field

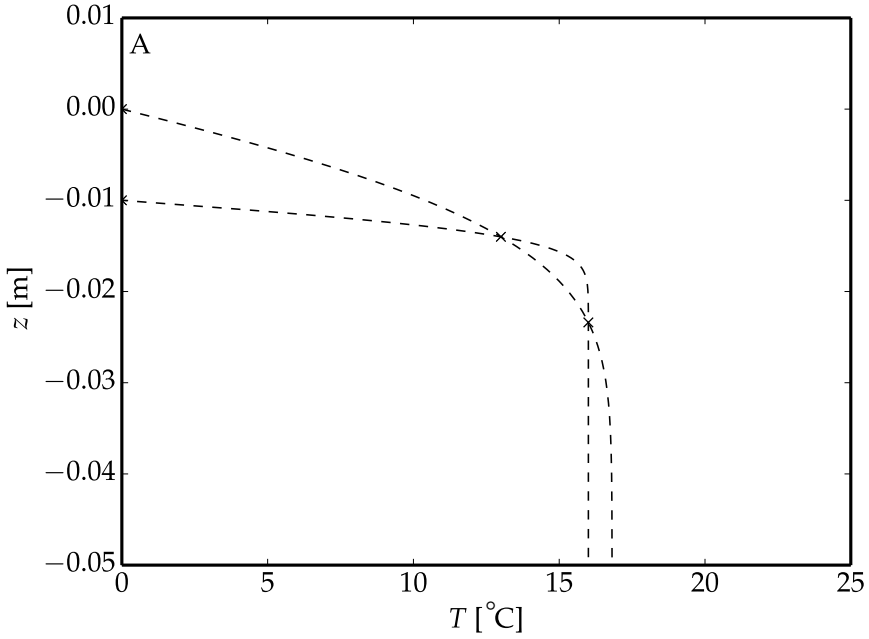

Figure 3.9: The two thermocouple measurements in the water beneath the ice at position $z = -1.402$ cm and $z = -2.339$ cm from Boger and Westwater (1967) (crosses). The far-field temperature is estimated from an error function fit considering different unknown ice-interface positions (dashed lines). Ice prevails at $z = -0.442$ cm and water prevails at $z = -1.402$ cm at the time of measurement and the true position must have been in-between. An estimated far-field temperature of the experiment is read from these fits.

temperature in their experiment must lie between 16 ℃ (error function shape) and 17.7 ℃ (turbulent mean profile), while values close to 16 ℃ are more likely.

3.4 Summary

The melt rates observed in the laboratory and the simulated melt rates agree quantitatively (cf. Figure 3.8) and the structure of the flow differs insignificantly. Thus, the physical model is sound and I complement the temperature profile from the laboratory experiment with the temperature and flow fields of the direct numerical simulations. The melt rate observed by Boger and Westwater (1967) lies within the range of the observed and simulated values. The melt rates depend strongly on the far-field temperature.

Chapter 4

Parameterisation of the Melt Rate in the Fresh-Ice–Fresh-Water System

With the successful complementation of laboratory measurements with direct numerical simulations in the previous chapter, I now employ the simulations to find a physically sound parameterisation of the melt rate of the fresh-ice–fresh-water system. The melt rate serves as a metric for the energy transport.

A physically sound parameterisation necessarily arises from an understanding of the structure of the flow (section 4.1). This chapter therefore follows the development of a general understanding of the energy transport through the system (section 4.2) that points to the investigation of the flow structure in terms of the two main transport mechanisms: diffusive transport and turbulent transport (section 4.3). The consideration of both transport mechanisms leads to my main result of this chapter (section 4.4): the formulation of a physically sound parameterisation of the melt rate with Eq. (4.12).

Several aspects of the melt rate such as its spatial inhomogeneity and its sensitivity to melt water are then discussed as well as its applicability to sea-ice–sea-water system.

4.1 The Appearance

The numerical simulations complement the temperature-profile measurements in the laboratory with temperature and velocity fields that are fully resolved in space and time. They also allow me to examine systems of increased domain size of up to one meter (cf. Table 2.1). Consequently, I obtain a statistically converged and more comprehensive impression of the flow: Figure 4.1.

The appearance of the flow has necessarily been described already for the comparison of laboratory experiment and simulation (cf. section 3.2.3). The description I have given there along with the visualisations in Figure 3.4 also holds for the visualisations of the higher resolved simulations (cf. Figure 4.1):

> "*Cold fluid [(blue)] unites more mass per volume and congregates to thin streaks that push downward through warmer surrounding fluid [(white)]. The lowermost point of the streaks is marked by a plume-like tip structure with vortexes at their sides. Looking at the horizontal cross-section, a honeycomb pattern is seen for both laboratory experiment and numerical simulation. From the comparison of vertical and horizontal cross-sections, one observes that plumes actually form the septum of the honeycomb cells. Cold plumes push down along the cell rim while fluid must consequently move up in the interior of the cell. Plumes are the dominant structures.*"

Their motion and diffusive decay mixes the water and transports energy across the boundary layer.

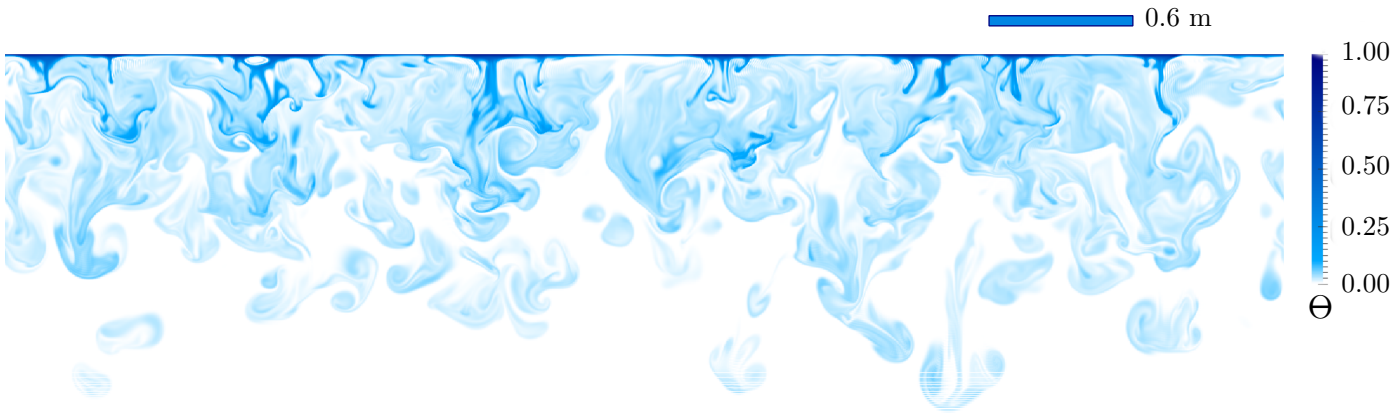

Figure 4.1: Vertical cross-section of the temperature field of the simulation of $\mathrm{Pr} = 10$, $\chi_m = 0.232$ on a $1280^2 \times 576$ grid at final simulation time. That corresponds to $\mathrm{Ri} = 11$ and a far-field temperature $T_\infty = 5.18$ ℃.

4.2 The Energy Flow

From the simulation data, I obtain the global energy flow through the system. The turbulent-kinetic-energy budget illustrates the similar working principle between fresh-ice–fresh-water system (cf. Figure 4.2b) and free convection in general (cf. Figure 4.2a). The evolution equation of the turbulent kinetic energy,

$$k = \frac{1}{2}\langle v_i' v_i' \rangle, \tag{4.1}$$

is derived from the second-order evolution equation of the velocity components. k evolves approximately according to

$$\partial_t k = -\frac{1}{\rho}\partial_t \mathcal{T} + \langle b' v_3' \rangle - \varepsilon \tag{4.2}$$

for purely buoyancy-driven flows (in the Boussinesq limit). $\langle b' v_3' \rangle$ is the buoyancy flux. $\mathcal{T}$ represents the turbulent transport term, i.e. the flux vector of k, and ε is the viscous dissipation rate.

Only vertical buoyancy production, $\langle b' v_3' \rangle$, feeds the turbulent kinetic energy, k, in the system (cf. Figure 4.2b). It can be shown that $\langle b' v_3' \rangle$ potentially converts potential energy to turbulent kinetic energy and vice versa. The dissipation rate, ε, on the contrary, converts turbulent kinetic energy unidirectional to internal energy. Dissipation is an irreversible process. It follows the production of turbulent kinetic energy in each component and follows the turbulent transport next to the wall.

The global energy flow through the system is thus from potential energy via kinetic energy to internal energy. Internal energy is continuously transported out of the system through the ice interface, the sink. Potential and internal energy is continuously supplied to the system by the infinite high-temperature reservoir in the far field, the source. To equilibrate the temperature difference between sink and source, the system diffuses and mixes fluid in-between sink and source and thereby entrains fluid from the high-temperature reservoir. The entrainment sustains a constant potential-energy flux to the system, that feeds the turbulent kinetic energy.

The distribution of turbulent kinetic energy in the system is not homogeneous. To equilibrate the spatial kinetic-energy inhomogeneity in the system, turbulent kinetic energy is transported away from the regions of its production to regions of lesser production: to a thin sharp region next to the interface and to a broad region in the far field. This transport of turbulent kinetic energy maintains the entrainment.

The symmetry of the system yields a vertical potential-energy gradient. The potential-energy gradient yields, thus, only vertical velocity fluctuations. To equilibrate this inhomogeneity in the partition of the kinetic energy, (i) the vertical

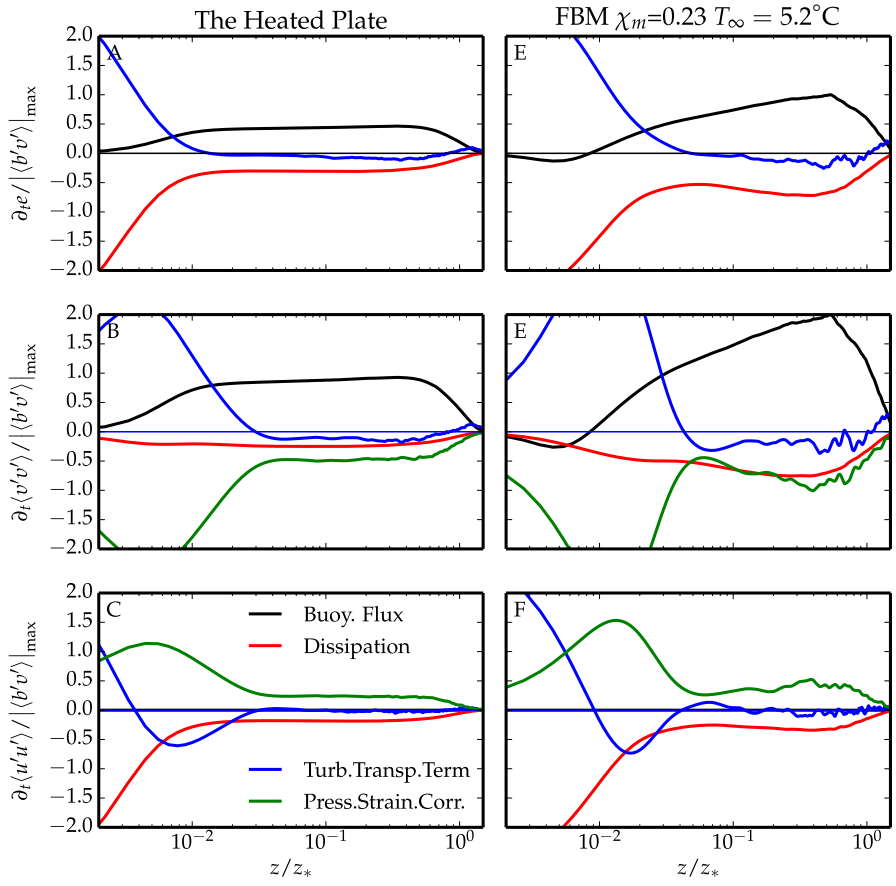

Figure 4.2: Turbulent-kinetic-energy budget of free convection over a heated plate (hp, left) and of the fresh-ice–fresh-water system (fbm, right). The data is normalised by the maximum buoyancy flux of the fresh-ice–fresh-water system. The upper panels (a,d) show the terms contributing to the total turbulent-kinetic-energy evolution $\partial_t k$: buoyancy production, $\langle b'v' \rangle$, (black), dissipation, ε, (red), and the turbulent transport term, $\mathcal{T}$, (blue). The panels in the middle (b,e) show the terms contributing to the vertical component of the turbulent kinetic energy. The pressure strain correlation (green) moves turbulent kinetic energy from the vertical component to the horizontal component [shown in lower panels (c,f)]. Data of the heated plate by courtesy of Juan-Pedro Mellado.

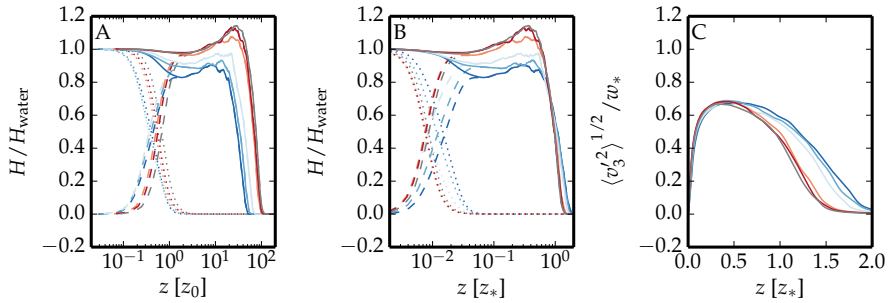

Figure 4.3: Simulation internal-energy flux and velocity fluctuation. Colours indicate different far-field temperatures according to Fig. 2.1. Molecular (dotted) and turbulent (dashed) fluxes contribute to the total internal-energy flux (solid). a) Internal-energy flux with abscissa normalised by the diffusive scale. b) Internal-energy flux with abscissa normalised by the convective scale. c) Vertical velocity fluctuation, normalised by the convective scale.

velocity fluctuations are transported away from the regions of their production to regions of lesser production: the interface and the far field. (ii) The pressure strain shifts turbulent kinetic energy from the vertical component to the horizontal (cf. Figure 4.2b,c). (iii) The interface also deflects the vertical velocity fluctuations to horizontal velocity fluctuations. The region next to the interface is the main region of horizontal velocity-fluctuation production. To equilibrate the spatial kinetic-energy inhomogeneity in the system, the horizontal velocity fluctuations are transported away from the regions of their production to regions of lesser production: to the mixed layer and the far field.

The system pursues equipartition of energy with the help of dissipation, the transport of turbulent kinetic energy and its spatial components. The resulting internal-energy fluxes and the resulting internal-energy distribution between sink and source are discussed in the following chapters.

4.3 The Flow Structure

The partitioning of the internal-energy flux according to Eq. (3.3) into a molecular flux $-c_p\rho\kappa\partial_3\langle T\rangle$ and a turbulent flux $c_p\rho\langle v_3'T'\rangle$ shows the working principle described in section 3 (Fig. 4.3): The positive turbulent flux shows that negative temperature fluctuations occur with descending motion and positive temperature fluctuations occur together with ascending motion in most of the domain (dashed line). Cold water descends, warm water ascends. At the interface the no-penetration condition suppresses the turbulent flux nearby, and the molecular flux remains as the only transport mechanism (dotted line). The total energy flux (solid) is sustained by turbulent entrainment of warm far-field water at the lower

boundary of the mixed layer. As the mixed layer broadens with time, it entrains warm water at a rate that yields a spatially constant energy flux throughout the mixed layer (solid line). The energy flux throughout the system determines the energy flux at the interface, H_{water}. The constant flux foretells according to Eq. (3.2) a steady mean-temperature profile despite cooling from the interface. A large extent of the system is hence in dynamic equilibrium (Mellado, 2012). As a consequence, I expect a steady temperature gradient at the interface, i.e. a constant melt rate.

The illustrated working principle and the heat-flux partition warrant a separate description of the diffusion-dominated inner layer and the turbulence-dominated mixed layer.

4.3.1 The Diffusion-Dominated Inner Layer

Next to the interface, the mean temperature changes by an order of magnitude over a diffusion-dominated layer of thickness z_0. The layer is stably stratified except for an unstably stratified fraction at its lower bound. This unstable fraction tends to overturn and hence tends to thin the diffusion-dominated layer. Such a situation is reminiscent of the buoyancy-reversal configuration studied, e.g., by Siems, Bretherton, Baker *et al.* (1990) and Mellado (2010). The unstable fraction covers the non-dimensionalised temperature range $[0, 2\chi_m]$ (cf. Eq. (2.12) and Fig. 2.1d) and thus extends over a distance $2\chi_m z_0$. A perturbation to the flow within $2\chi_m z_0$ accelerates proportionally to b_{m} and decelerates proportionally to the viscosity ν. The timescale of the perturbation growth is $t_{\mathrm{buoy}} = (\nu/b_{\mathrm{m}}) \,/\, (2\chi_m z_0)$ (Turner, 1973). On the other hand, diffusion broadens z_0 at a rate κ/z_0. The timescale of diffusive advancement over the fraction of z_0 is hence $t_{\mathrm{diff}} = 2\chi_m z_0 / (\kappa/z_0)$. While diffusive advancement broadens z_0, a buoyancy perturbation accelerates fluid away from the region and thins it. The critical depth at which the rate of thinning is equal to the rate of broadening, $t_{\mathrm{diff}} = t_{\mathrm{buoy}}$, marks the extent of the diffusion-dominated layer z_0,

$$z_0 = \frac{10}{(2\chi_m)^{2/3}} \mathrm{Pr}^{1/3} \left(\kappa^2 / |b_m|\right)^{1/3}. \tag{4.3}$$

The layer of extent z_0 is 'the diffusive sublayer', a part of the surface layer that has been introduced in the previous section. The factor 10 gives the commonly used criticality for this Rayleigh-number criterion. z_0 is independent of time; the diffusive sublayer has a fixed extent.

4.3.2 The Turbulence-Dominated Mixed Layer

The mixed layer, on the contrary, is unsteady; it broadens in time. Still, it behaves self-similarly if a boundary-layer height z_* is chosen as

$$z_* = \frac{1}{H_{\text{water}}} \int_0^\infty \mathcal{H}\left(\langle T' v_3' \rangle\right) \langle T' v_3' \rangle \mathrm{d}z \tag{4.4}$$

(Fig. 4.3b), and a convective velocity scale w_* is chosen as

$$w_*^3 = \int_0^\infty \mathcal{H}\left(\langle b' v_3' \rangle\right) \langle b' v_3' \rangle \mathrm{d}z \tag{4.5}$$

(Fig. 4.3c), where $\mathcal{H}$ is the Heavyside function. The convective velocity scale w_* is found from the inviscid scaling of the viscous dissipation rate $\varepsilon \propto w_*^3 \, z_*^{-1}$ (Pope, 2000) and the observation that

$$\frac{\int_0^\infty \varepsilon \mathrm{d}z}{\int_0^\infty \langle b' v_3' \rangle \mathrm{d}z} \approx 0.7 \tag{4.6}$$

in our simulations. This result implies that the viscous dissipation rate ε balances a large constant fraction of the turbulent buoyancy production $\langle b' v_3' \rangle$.

Commonly, a relevant buoyancy-flux scale of a free-convection system, B_{eff}, is known a priori, and is then used in combination with the boundary-layer height z_* to construct a velocity scale from $(B_{\text{eff}} \, z_*)^{1/3}$ (Deardorff, 1970). In this work, however, a relevant buoyancy-flux scale is not known a priori, nor is it readily evident from the internal-energy flux, H_{water}, via a buoyancy parameter that relates temperature and buoyancy (cf. Eq. (2.13)). Hence, I define an effective buoyancy flux by

$$B_{\text{eff}} = \frac{w_*^3}{z_*}. \tag{4.7}$$

In agreement with the previous paragraphs and with free-convection systems in general, B_{eff} as defined above is found to be constant in time, once the mixed layer is developed (cf. Figure 4.4a). B_{eff} ranges between 0.1 and 0.4 in units of the diffusion-dominated buoyancy flux of free-convection systems, $\left(b_m^4 \kappa\right)^{1/3}$ (cf. Figure 4.4b). As a function of χ_m, B_{eff} decreases by a factor of 4 from the low-temperature range to the high-temperature limit. By definition of Eq. (4.7), the effective buoyancy flux relates to the energy flux H_{water} as

$$H_{\text{water}} = B_{\text{eff}} \frac{\int_0^\infty \mathcal{H}\left(\langle T' v_3' \rangle\right) \langle T' v_3' \rangle \mathrm{d}z}{\int_0^\infty \mathcal{H}\left(\langle b' v_3' \rangle\right) \langle b' v_3' \rangle \mathrm{d}z} \tag{4.8}$$

(Fig. 4.5c). The linear relationship, $H_{\text{water}}/B_{\text{eff}} \approx 0.55 \chi_m T_\infty / b_m$, is empirically determined. With Eqs. (2.13, 2.10, 4.7, 4.8) it yields

$$H_{\text{water}} = \alpha_{\text{T}} \frac{w_*^3}{z_*} \frac{T_m}{T_\infty - T_m}, \tag{4.9a}$$

$$\alpha_{\text{T}} = 8.3 \times 10^9 \text{ W s}^3 \text{ m}^{-4}. \tag{4.9b}$$

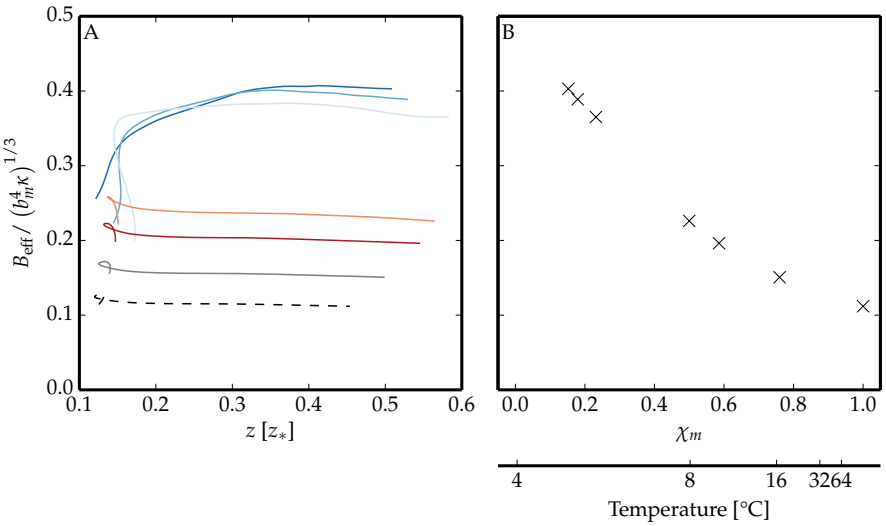

Figure 4.4: Effective buoyancy flux. Colours indicate different far-field temperatures as illustrated in Fig. 2.1b. a) Time evolution of the effective buoyancy flux given in convective time scale. b) Averaged effective buoyancy flux as a function of far-field temperature parameter. The average does not include the initial transient (cf. panel a).

H_{water} is thus obtainable for systems of known far-field temperature T_∞ once estimates for the boundary-layer height, z_*, and the convective velocity, w_*, are provided. With H_{water} determined, the melt rate can be obtained from Eq. (3.1).

4.3.3 The Energy Flux of Fully Developed Systems

After an initial transient, the energy flux of all simulations decays towards a constant value (Fig. 4.5). The warmer the far-field water is, the larger the energy flux. The energy flux in terms of the temperature gradient ranges over more than an order of magnitude, from 2.6×10^2 K m^{-1} at $T_\infty \approx 4.8$ °C to 3.7×10^3 K m^{-1} at $T_\infty = 9.6$ °C. I find that the gradient is described by a temperature drop of order T_∞ over a length z_0.

$$\partial_3 \langle T \rangle (z,t)|_{z=0} = f(\chi_m)\ T_\infty\ {z_0}^{-1}, \tag{4.10}$$

with the proportionality constant f only dependent on the far-field temperature parameter χ_m (Fig. 4.5b). f varies within the interval $[1.0; 2.2]$. So far, the diffusive length scale z_0 has been derived as the critical depth at which molecular diffusion and buoyancy are in balance. This reasoning was inspired by the analogy between this study and the cloud-top mixing layer. The system in this study, however, has a solid wall next to the diffusive sublayer. Hence, I attribute the variation f of the normalised temperature gradient at the wall (Fig. 4.5) to the

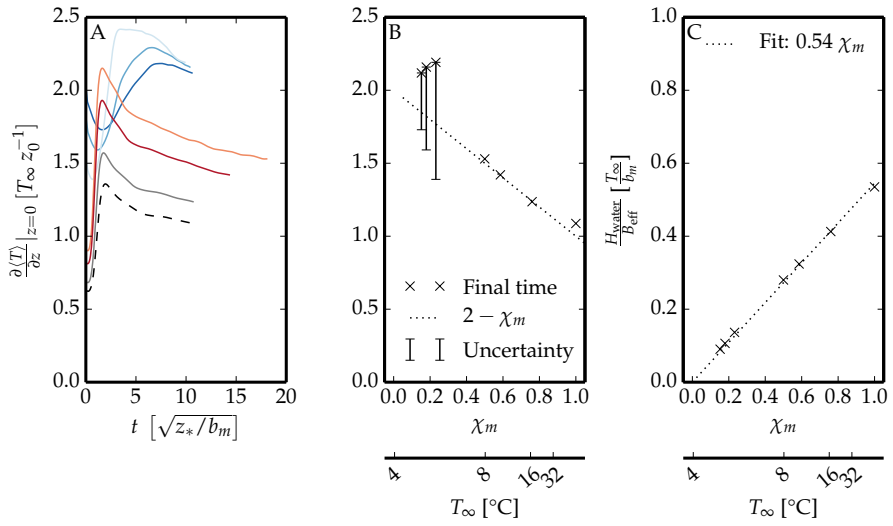

Figure 4.5: Melt rates (a) given as the interfacial temperature gradient in units of T_∞/z_0. All simulations seem to target a non-dimensional temperature gradient between one and two. Colours indicate different far-field temperatures according to Fig. 2.1. (b) Temperature gradient at final simulation time over the far-field temperature parameter, χ_m, defined in Eq. (2.10), and $f(\chi_m)$ (dotted line). (c) Proportionality coefficient $\int_0^\infty \mathcal{H}\left(\langle T'v_3'\rangle\right)\langle T'v_3'\rangle \mathrm{d}z\ /\ \int_0^\infty \mathcal{H}\left(\langle b'v_3'\rangle\right)\langle b'v_3'\rangle \mathrm{d}z$ in units of $\mathrm{T}_\infty\ \mathrm{b}_m^{-1}$ as determined from our simulations.

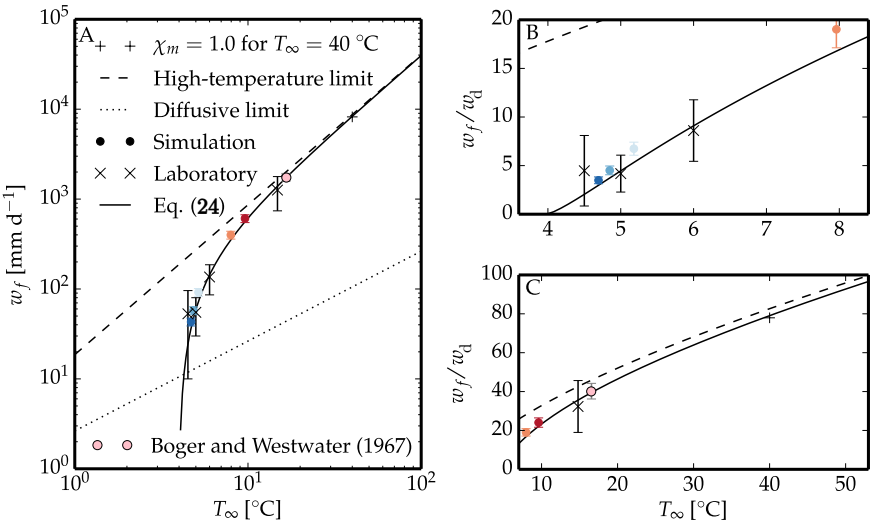

Figure 4.6: Melt rate derived from scalar gradient at the interface (simulation, coloured dots corresponding to Fig. 2.1) and derived from bulk-temperature change (laboratory, crosses). Analytical melt rate, w_f, as given in Eq. (4.12) (black solid line). Diffusive melt rates, w_d, as given in Eq. (3.7) (dotted line). The dashed line indicates the high-temperature melt rate limit. (a) Double logarithmic plot illustrates the power-law change over the full temperature range. (b) Linear plot illustrates the melt-rate enhancement in the low-temperature range. (c) Linear plot illustrates the melt-rate enhancement in the high-temperature range. The pink dot indicates the interpreted measurement "12V" of Boger and Westwater (1967).

presence of the wall. To account for this influence, I estimate

$$f(\chi_m) = 2 - \chi_m \tag{4.11}$$

(Fig. 4.5, dotted line).

4.4 The Melt-Rate Parameterisation

The assessment of the inner layer and the mixed layer indicates that the internal-energy flux of the simulation is in a steady state (cf. Figure 4.5). A steady internal-energy flux to the interface yields a constant melt rate that only depends on the far-field temperature of the water.

The previous results are now combined to give an analytical expression for the melt rate of a thermally driven fresh-ice–fresh-water interface. With Eqs. (2.13,

2.10, 3.1, 4.3, 4.10, 4.11) I find

$$w_{\mathrm{f}} = w_{\mathrm{f},0} \left(\frac{(T_\infty - T_m)^2}{T_\infty T_m} \right)^{2/3} \left(\frac{T_\infty + T_m}{T_m} \right) \tag{4.12}$$

with

$$w_{\mathrm{f},0} = \left(\frac{2^2}{10^3 \mathrm{Pr}} \right)^{1/3} \frac{\rho\,(T_\infty)}{\rho_{\mathrm{ice}}} \frac{c_p T_m}{L} \left(g \frac{\beta T_m^2}{\rho_{\mathrm{water}}} \kappa \right)^{1/3} = 2.15 \times 10^{-6} \mathrm{m\ s^{-1}}, \tag{4.13}$$

with Pr= 10 and $\rho\,(T_\infty) = 10^3$ kg m^{-3} (Fig. 4.6, black solid line). $w_{\mathrm{f},0}$ corresponds to $1.86{\times}10^2$ mm d^{-1}. Note that in nature Pr=Pr(T) and varies from 13.18 to 5.40 in the relevant temperature range of 0 ℃ to 30 ℃ (Sharqawy, Lienhard and Zubair, 2010). The melt rates of Eq. (4.12) match the melt rates estimated in the laboratory experiment and in the simulations. Eq. (4.12) seems to slightly underestimate the simulation results for low far-field temperatures (Fig. 4.6b), but these simulations have not yet completely reached their steady behaviour.

The enhancement of the melt rates for far-field temperatures between four and eight degrees Celsius ranges from 0 to 16 (Fig. 4.6b). The enhancement of the melt rates for far-field temperatures between 20 ℃ and 40 ℃ range between 45 to 77 (Fig. 4.6c). Thus, the relative enhancement of the melt rates with far-field temperature decreases for increasing temperature.

The comparison of Eq. (4.12) to the corresponding expression of free convection without buoyancy reversal reveals the dynamics of the system. With Eqs. (2.13, 3.1, 3.8) and the diffusive length scale in free convection without buoyancy reversal, $z_{\mathrm{diff}} = \left(\kappa^2 / |b_m|\right)^{1/3}$, one finds:

$$w_f \propto \frac{T_\infty}{T_m} \left(\frac{T_\infty - T_m}{T_m} \right)^{2/3}. \tag{4.14}$$

In the high-temperature limit, I obtain $(T_\infty/T_m)^{5/3}$ from Eq. (4.14) and I also obtain $(T_\infty/T_m)^{5/3}$ from Eq. (4.12) (Fig. 4.6, dashed line). Thus, the high-temperature limit of Eq. (4.12) corresponds to the behaviour found for the heated plate, where no stable stratification is present. I conclude that the shielding of the interface by the stable stratification next to it effectively vanishes for $T_\infty \gg T_m$.

In the low-temperature limit, I obtain $\left((T_\infty - T_m)/T_m\right)^{2/3}$ from Eq. (4.14) in contrast to $\left((T_\infty - T_m)/T_m\right)^{4/3}$ from Eq. (4.12). Thus, the shielding of the interface diminishes the melt rate with a power of two in the dependence on the relative temperature difference $\left((T_\infty - T_m)/T_m\right) < 1$.

4.5 Discussion

4.5.1 The Onset of Convection

In general, the comparison of melt rates w_f to diffusive melt rates w_d yields an enhancement by one to two orders of magnitude, where I give w_d related to the final boundary-layer thickness of our laboratory experiment, $\delta = 0.40\ h_{\mathrm{water}}$ (cf. Eq. (3.7)). For temperatures T_∞ just above T_m, however, for which the occurrence of buoyancy reversal sets in, I find turbulence-enhanced melt rates that seem smaller than diffusive melt rates (Fig. 4.6, solid line below dotted line). For these systems the diffusive sublayer z_0 is larger than δ, and no turbulence were to be observed for a boundary-layer thickness of $\mathcal{O}(\delta)$.

4.5.2 The Influence of Melt Water on the Melt Rate

When ice melts, it forms melt water of $T = 0$ °C. Recently formed melt water does not possess any kinetic energy and thickens the diffusive sublayer in which the stable stratification occurs. Thus melt water increases the shielding of the ice from rising warm fluid and diminishes the melt rate. This describes a negative feedback. I now assess its strength.

In a frame of reference that moves with an interface melting at speed w_{ice}, the formation of melt water appears as vertical background mean advection. The corresponding advection velocity is

$$v_{\mathrm{int}} = -\frac{\rho_{\mathrm{ice}}}{\rho_{\mathrm{water}}} w_{\mathrm{ice}}. \tag{4.15}$$

In principle w_{ice} depends on time and on the position within the interface. The time dependence of the mean value vanishes after an initial transient, when the system is freely developing (cf. Fig. 4.5). For now, I also assume no dependence on the position within the interface, but I will assess this assumption in the next section.

With constant v_{int}, the moving frame of reference is still an inertial system. The governing Eqs. (2.5) still apply, but different boundary conditions need to be considered. Instead of no-slip, no-penetration boundary conditions, the system imposes no-slip, constant-velocity boundary conditions, $v_{\mathrm{int}}\delta_{i3}$ at $z = 0$.

A first estimate of the influence of melt-water formation on the flow structure can be obtained as follows. The constant-velocity boundary condition imposes a second velocity scale, v_{int}, to the system. I am interested in how it compares to common velocities within the flow. From $\frac{v_{\mathrm{int}}}{w_*}$, using $w_{\mathrm{ice}} = w_f$ in Eq. (4.15), I find that the melt-water advection in the limit of small far-field temperatures is negligibly small compared to common flow velocities (cf. Fig. 4.7, crosses). The magnitude of $\frac{v_{\mathrm{int}}}{w_*}$ increases with increasing far-field temperature from 1.5‰

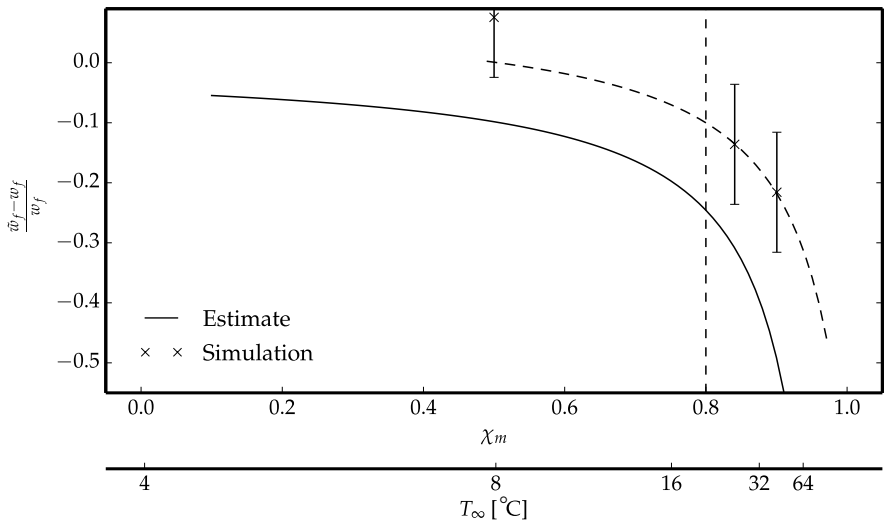

Figure 4.7: Estimates of the influence of melt-water formation at the interface on the melt rate. (black) Analytical estimate (cf. Eq. (4.16)). (dots) Numerical estimate derived from comparison between analytical melt rates and melt rates obtained from simulations with background mean advection. (dashed line) Guidelines to the eye.

at 8℃ to $\mathcal{O}(1\ \%)$ at 17 ℃. Only for far-field temperatures larger than that a considerable influence of v_{int} on the flow structure is to be expected.

I obtain a second estimate for the influence of the constant-velocity boundary condition on the melt rate from the comparison of the advection to the diffusion flux at the interface using $w_{\text{ice}} = w_f$ in Eq. (4.15):

$$\frac{v_{\text{int}}\,(T_{\text{ice}} - T_\infty)}{\kappa \partial_j T} = \frac{v_{\text{int}}\,(T_{\text{ice}} - T_\infty)}{\frac{L}{c_p} v_{\text{int}}} = \frac{c_p}{L}\,(T_{\text{ice}} - T_\infty)\,. \tag{4.16}$$

For far-field temperatures approaching T_m, the estimate approaches $(c_p/L)\,(T_{\text{ice}} - T_m) \approx \frac{1}{20}$, and diverges for high far-field temperatures (Fig. 4.7, line). The divergence for high far-field temperatures exposes that the estimate of Eq. (4.16) does not account for the full feedback mechanism described above. Melt water cannot diminish the melt rate infinitely but only diminishes it as long as ice is melting. Here, I only considered a fixed constant-velocity boundary condition with w_{ice} determined from Eq. (4.12). Thus, Eq. (4.16) is merely a maximum estimator to the feedback mechanism and I expect to find in practice a smaller diminution than estimated here.

To verify these estimates, I conduct a set of three simulations at temperatures $T_\infty \in \{8,\ 25,\ 40\}$ ℃ that account for the melt-water formation with v_{int} set accordingly. I compare the melt rates of these simulations $\tilde{w}_f$ to the analytical

melt rate w_f obtained from Eq. (4.12) as

$$\frac{\tilde{w}_f - w_f}{w_f}. \tag{4.17}$$

The values range within those of the analytical maximum estimator, Eq. (4.16), and confirm the diminishing effect of melt water on $w_f\,(T_\infty)$ (Fig. 4.7, dashed line). The simulated diminution and Eq. (4.16) follow an alike dependence on T_∞, with an offset of ~ -8 % and a shift of $\sim 0.06\ \chi_m$. Hence, the velocity $v_{\mathrm{int}}\delta_{i3}$ of each of the three simulations was systematically chosen too high to correctly represent reality. Smaller velocities v_{int} would in fact diminish the melt rate less and yield melt rates closer to Eq. (4.12).

I find the numerical estimate in agreement with the laboratory experiments. I did not observe a pronounced signature of the melt water in the flow structure as compared to the simulations with no-penetration boundary conditions.

I conclude that the effect of melt-water formation can at least be neglected for far-field temperatures $T_\infty < 20$ °C ($\chi_m = 0.8$). Within this limit the presented melt-rate equation, Eq. (4.12), holds with a diminution of less than 10 % due to the influence of melt water (Fig. 4.7, black dashed lines). For far-field temperatures $T_\infty \gg 20$ °C, for which the influence of the melt water is significant, I expect the feedback to yield a temperature dependence in-between $w_f \propto T_\infty$ (diffusive) and $w_f \propto T_\infty^{5/3}$ (turbulent).

4.5.3 The Spatial Inhomogeneity of the Melt Rate

The temperature gradient at the interface (Fig. 4.8a,b) varies in space, (x_1, x_2). I now assess this variation of the melt rate around its mean value, Eq. (4.12), on the basis of the probability density function (pdf) (Fig. 4.8c).

The ensemble of pdfs for different far-field temperatures exhibits two main modes of different characteristic. The first mode is dominant in pdfs of low far-field temperatures, represents melt rates smaller than the mean and has a relative standard deviation of 10 %. The second mode is dominant in pdfs of high far-field temperatures, represents the mean and has a relative standard deviation of 60 %. In the diffusive limit, that is in the absence of convection, one expects to find a pdf that is a delta function at $\langle \partial_3 T \rangle|_{z=0}$. The first mode is considerably narrower than the second and yields absolute melt rates closer to those of purely diffusive melting (Fig. 4.6). I refer to the first mode as the diffusive mode. The second mode at the centre of the pdf resembles the melt rate in the high-temperature limit $\chi_m = 1$ (Fig. 2.1d, dashed curve; cf. Fig. 4.8c, black). This mode is purely convection dominated as can be inferred from the interface pattern (Fig. 4.8b). I refer to the second mode as the turbulent mode.

With increasing far-field temperature I observe a shift of the main contribution to the pdf from the diffusive mode to the turbulent mode. This transition is

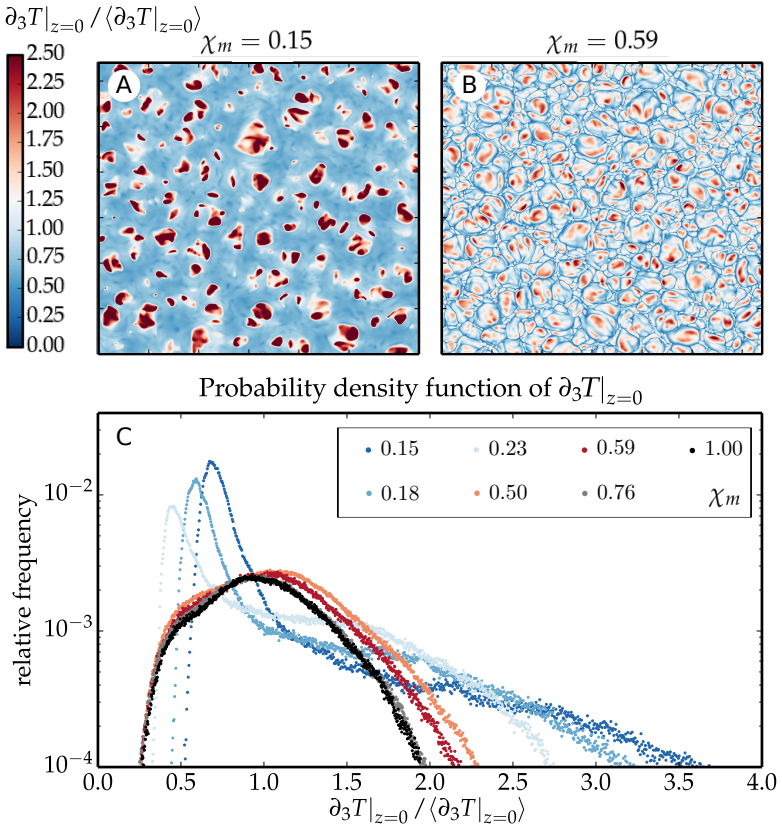

Figure 4.8: Dependence of the melt rate on the position within the interface. a) $\partial_3 T|_{z=0}(x_1, x_2) / \langle \partial_3 T|_{z=0} \rangle$ for $\chi_m = 0.15$. b) $\partial_3 T|_{z=0}(x_1, x_2) / \langle \partial_3 T|_{z=0} \rangle$ for $\chi_m = 0.59$. c) Probability density function of $\partial_3 T|_{z=0} / \langle \partial_3 T|_{z=0} \rangle$.

in line with the mechanism proposed so far: For low far-field temperatures, a strong stable stratification close to the interface shields the ice from the rising warm turbulent water. Only few rising plumes manage to intrude this shield and enhance the melting at the interface locally (Fig. 4.8a). This local turbulent intrusion contributes to the pdf at values five to seven times larger than the first mode. Most of the near-interface region remains stably stratified, thus diffusion dominates. For high far-field temperatures, the strength of the stable stratification is not sufficient to shield the ice anymore. The increasing contribution of the turbulent mode broadens the absolute bandwidth of the pdf and shifts the diffusive mode to lower relative values. As the importance of the diffusive mode ceases the relative bandwidth of the pdf reduces. Then, the ice is immediately exposed to rising warm turbulent plumes and I find an interface pattern known from the turbulent free-convective motion (Fig. 4.8b).

I have found in the last section that the influence of the melt-water formation is negligible for low far-field temperatures. For high far-field temperatures, the shielding effect of the melt water becomes more relevant, according to Eq. (4.16). The maintenance of a spatially resolved $\upsilon_{\mathrm{int}}\left(x_1, x_2\right)$ in section 4.5.2 would diminish the upper end of the pdf more than it would diminish the lower end of the pdf. As a first approach, Eqs. (3.8, 4.16, 4.17) suggest multiplying the pdf with a linear function of slope [Eq. (4.16)] to account for a spatially resolved υ_{int}. This would narrow the bandwidth of the probability density function in Fig. 4.8c and would homogenise the interface pattern found in Fig. 4.8b.

4.5.4 The Application of the Parameterisation to Natural Flows

The motivation to study the present setup has been its structural similarity to the sea-ice–ocean interface and to the ice-shelf–ocean interface. The question arises how much information can be transferred from our findings to such interfaces. I am aware that ice–ocean interfaces do not just melt, but ablate, in the interplay of differently diffusing salinity and temperature. Still, I use our model as a simplified approach and focus only on the shape of the mean-buoyancy profile.

The process picture used to derive the scaling laws of the inner layer suggests that the strength of the stable-stratification shield beneath the ice characterises the flow. The stable stratification has shown to shield the ice for all $b\left(z=0\right) > b_m$. The relative strength of the shielding is therefore defined as $\Delta b = b\left(z=0\right) - b_m$ and compared to the strength of the buoyancy forcing b_m (Fig. 2.1d). This is effectively the Richardson number

$$\mathrm{Ri}_0 = \frac{\Delta b z_0}{w_0^2} = \frac{\Delta b z_0}{\left|b_m\right| z_0} = \frac{b\left(z=0\right)}{\left|b_m\right|} + 1 \tag{4.18}$$

that describes the ratio between the potential energy that a fluid particle requires in order to overcome the diffusive shield Δb of thickness z_0, and the kinetic energy w_0^2 a fluid particle acquires in free fall at b_m over z_0.

Martin and Kauffman (1977) study the case of the sea-ice–ocean interface in a laboratory tank experiment. I derive $b\,(z=0) \approx 0.1385$ m s^{-2} from their salinity and temperature profiles given in Fig. 2e and Eq. (9) of their study [1] together with Eq. (2.1) of this study. With a redefinition of the minimum buoyancy that accounts for the influence of temperature and salinity,

$$b_m = g\frac{\rho\,(S_\infty, T_{\text{ice}}) - \rho\,(S_\infty, T_\infty)}{\rho\,(S_\infty, T_\infty)}, \tag{4.19}$$

with the far-field salinity S_∞ taken from their salinity profile, I find $b_m \approx 0.0011$ m s^{-2} and $\text{Ri}_0 \approx 129$. If I use the boundary conditions T_{ice}, S_∞ and T_∞ as provided from their one-dimensional theoretical model, I consistently obtain $\text{Ri}_0 = 136$ for their setup. In the case studied in this work, I find a similarly strong stable stratification for a far-field temperature of $T_\infty = 4.33$ °C.

According to our results turbulence enhances the melt rate by $w_f\,(T_\infty = 4.33)\,/w_d\,(T_\infty = 4.33) \approx 1.23$. Martin and Kauffman (1977) determined an enhancement of the melt rate by a constant factor of 2.5. Given that I consider melt-rate variations over two orders of magnitude (Fig. 4.9a), this is in fairly good agreement despite the neglect of the influence of salt.

As opposed to the finding of Martin and Kauffman (1977), turbulence does not seem to enhance the melt rate by a constant factor but by a factor that depends on the relative strength of the shielding, the Richardson number Ri_0. With the parameter range of far-field temperature and salinity that they provide from their model (Fig. 9 therein), Ri_0 varies between 10^2 and 10^3. This order-of-magnitude variation in Ri_0 translates to a variation in the turbulent enhancement by a factor of approximately four according to Fig. 4.9a (herein). $T_\infty \in [10, 30]$ °C even yields Ri_0 of $\mathcal{O}\left(10^1\right)$. Ri_0=40 corresponds to this T_∞ range and I find $w_f\,(\text{Ri}_0 = 40)\,/w_f\,(\text{Ri}_0 = 136) \approx 2$. I conjecture that Martin and Kauffman (1977) would have found a turbulence enhancement of the melt rate by a factor of five for significantly increased far-field temperatures.

In nature, the flow beneath an ice interface is driven by several mechanisms. To allow for the comparison of our results to those of systems with different driving mechanisms, such as shear or internal heating from radiation, I propose to use the convective Richardson number

$$\text{Ri}_* = \frac{\Delta b z_0}{w_*^2}. \tag{4.20}$$

The direct link of the buoyancy-forcing strength b_m to the velocity scale of the system w_0 is replaced by the more generic convective velocity scale of the system, w_*, as defined in Eq. (4.5). One could thus interpret the simulations of different far-field temperatures as simulations of fixed far-field temperature but different

[1] The zero-order density is taken as 10^3 kg m^{-3} and not as given there as 10^2 kg m^{-3}.

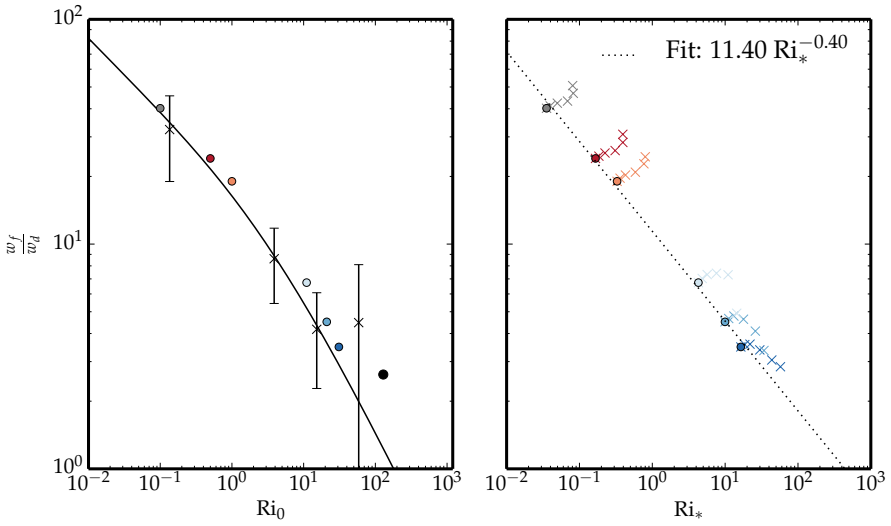

Figure 4.9: Turbulent enhancement of the melt rate compared to the diffusive melt rate w_d, Eq. (3.7), (a) over Richardson number Ri_0, Eq. (4.18), with the simulations (dots), laboratory experiments of this study (crosses), Eq. (4.12) (solid) and the study of Martin and Kauffman (1977) (black dot). Colours indicate different far-field temperatures according to Fig. 2.1. b) Turbulent enhancement of the melt rate over the convective Richardson number Ri_*, Eq. (4.20). Crosses indicate the temporal evolution towards the final simulation time (dots). A linear fit of the final-simulation values $\log(w_f/w_d)$ over $\log(\mathrm{Ri}_*)$ gives the fitted curve (dotted line).

Ri_* (Fig. 4.9b). From a linear fit of the final-simulation values $\log(w_f/w_d)$ over $\log(\mathrm{Ri}_*)$, I conjecture that the melt rate follows Ri_* as

$$w_f = \text{const.} \times \mathrm{Ri}_*^{-0.40}. \tag{4.21}$$

Chapter 5

Parameterisation of the Melt Rate in the Sea-Ice–Sea-Water System

The successful parameterisation of the melt rate in the previous chapter from the insights into the flow structure obtained by direct numerical simulations, encourages to apply this approach also to the sea-ice–sea-water system. Analogous to the treatment of the fresh-ice–fresh-water system, this chapter is organised into the appearance of the flow (section 5.1), the energy transport through the sea-ice–sea-water system (section 5.2) and its flow structure (section 5.3).

The influence of salt in the sea-ice–sea-water system complicates the parameterisation of the melt rate. In addition to the influence of salt on the flow structure, salt also influences the interface temperature of the ice. The flow transports heat to the ice interface, thereby ablates it and dilutes it, but the flow also transports salt to the ice interface that counteracts the dilution. The equilibrium between dilution and salt transport yields an interfacial salinity that determines the interfacial temperature. An additional section is therefore devoted to the interfacial equilibrium and the determination of the interfacial conditions (section 5.4).

The insights into the flow structure and the interfacial equilibrium are then combined to parameterise the melt rate with Eq. (5.24) (section 5.5). Several aspects of the melt rate such as the relevance of temperature, salinity, and intensity of turbulence are discussed and the parameterisation is applied to real-world conditions (section 5.6).

5.1 The Appearance

The visual appearance of the sea-ice–sea-water system (cf. Figure 5.1) is similar to the one of the fresh-ice–fresh-water system at first sight (cf. Figure 4.1). Whirls

of warm and cold water manifest next to the interface and move downwards (cf. Figure 5.1a). Their movement and their diffusive decay mixes the water.

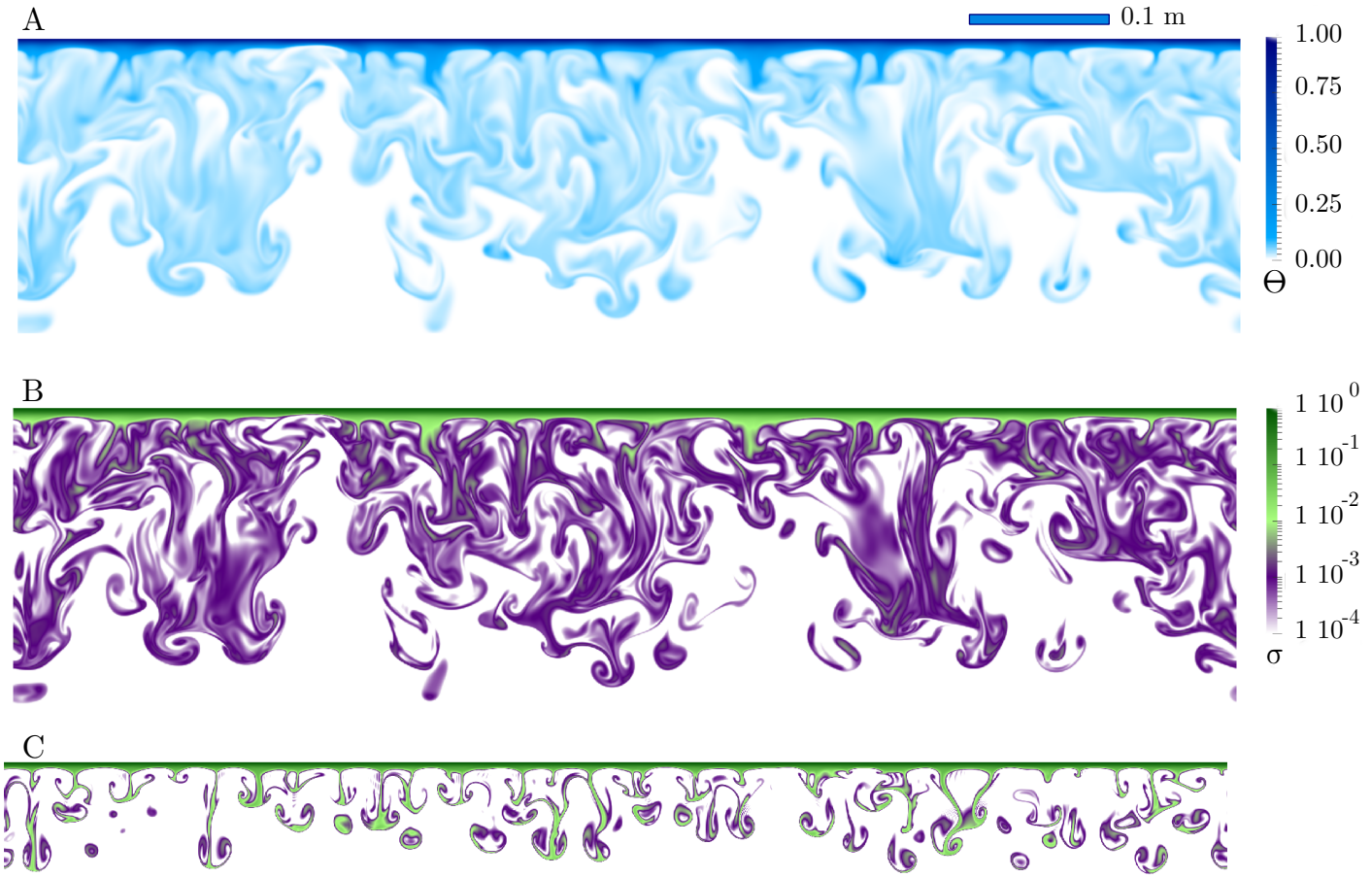

Figure 5.1: a) Vertical cross-section of the temperature field of the simulation at Pr = 10, Le = 4, and Ri = 11 on a $2560^2 \times 1152$ grid at final simulation time. That corresponds to a far-field temperature of $T_\infty = 16.4$ ℃ if a far-field salinity of $S_\infty = 34$ g kg^{-1} is assumed. b) Same as (a) but for the salinity field on a logarithmic colour scale. c) Initial evolution of the salinity field shows salt fingers.

The whirls are evident in both the temperature field and the salinity field (cf. Figure 5.1b). The comparison of the two fields highlights several intrinsic aspects of the sea-ice–sea-water system. First, salinity structures are more filigree than temperature structures because the Schmidt number is higher than the Prandtl number. Second, the mixing structures appear at the same locations in both fields because the instability arises from the interplay of both scalars. It is a double-diffusive phenomenon. Third, the core of instabilities consists of cold and saline fluid. The most saline and coldest fluid is particularly dense, it has the minimum buoyancy, b_m. This fluid promotes the buoyancy reversal instability and drives the convection.

On second sight, the visual appearance of the system differs from the one of the fresh-ice–fresh-water system. Double-diffusive systems are known to manifest different regimes with typical instabilities, such as salt fingers, staircases, oscillations and convection (Turner, 1974). Initially the flow clearly exhibits salt fingering in the form of plumes that are more waisted and elongated and reach further into the domain compared to those of the fresh-ice–fresh-water system (cf. Figure 5.1c). This is an effect of the high Schmidt number, $\mathrm{Sc} > \mathrm{Pr}$, and of the chosen initial condition to force a quicker development of the boundary layer. The regime of cold and fresh water above warm and salty water is called double-diffusive convection or semiconvection. Later when the flow is fully developed, semiconvection shows its countenance. The motion appears more confined than in fresh-ice–fresh-water system. In the latter plumes freely fall and mix till they diffuse. Here, they seem to be deflected and to travel sideward and upward. This is characteristic for double-diffusive convection (Zweigle, 2011): While the cold and salty structures sink and diffuse, they gain buoyancy by heating and rise again. In the fresh-ice–fresh-water system the plumes can often be traced back to their emerging spot at the interface, here they seem to disconnect more quickly from their source and form an interweaving network as they mix and diffusive to transport energy.

5.2 The Energy Flow

The global energy flow through the system is in principle similar as seen for the fresh-ice–fresh-water system. The total energy within a fixed volume can be stored as kinetic, potential or internal energy. In simple terms, the energy flows from potential energy via kinetic energy to internal energy. Internal energy is continuously transported out of the system through the ice interface, the sink. Internal energy is continuously supplied to the system by the infinite high-temperature reservoir in the far field, the source. To equilibrate the temperature difference between sink and source, the system diffuses and mixes fluid in-between sink and source and thereby entrains fluid from the high-temperature reservoir. The entrainment sustains a potential-energy flux to the system, that feeds the turbulent kinetic energy, and internal energy flows at continuous rate.

The difference to the fresh-ice–fresh-water system is that the potential energy is not supplied or removed by the sheer presence of the temperature difference between source and sink. Instead, the interplay of salinity and temperature provides the energy potential, thus provides and removes kinetic energy. Just beneath the lower boundary of the mixed layer, water is more saline than the average in the mixed layer. This water is cooled when it is entrained, and tends to sink, overturns, and sustains entrainment. Just aloft the upper boundary of the mixed layer, water is less saline than the average in the mixed layer. This water is heated by the mixed layer and would tend to rise. However, it does not: The influence of the salinity gradient throughout the diffusive layer dominates the heating. The salinity gradient acts as a potential-energy barrier to the kinetic energy of the mixed layer.

This interplay of temperature and salinity provides new means to reversibly and irreversibly convert energy between its different forms. In general, the potential-energy difference between two evolution stages of the system does not necessarily reflect the irreversible change in the system states. On the one hand, the system can reversibly convert potential energy to kinetic energy and vice versa. On the other hand, the system can irreversibly convert kinetic and potential energy in a way that alters the minimum potential energetic state of the system. One way to address the ambiguity in the definition of the energetic states of a turbulent system is by defining an available potential energy (Winters, Lombard, Riley *et al.*, 1995). The available potential energy is the energy available for irreversible conversion. Another way to address the ambiguity of reversible and irreversible energy conversion is the discussion of the energy flow in terms of the turbulent-kinetic-energy budget. The latter must only be applied if the turbulent-kinetic-energy budget can unambiguously be obtained in a way that excludes adiabatic processes. That is, the turbulent-kinetic-energy budget must be obtained by averaging over sufficiently large space or time. The successful employment of the latter method for the fresh-ice–fresh-water system encourages an attempt on the sea-ice–sea-water system.

The turbulent-kinetic-energy budget illustrates the similar working principle between fresh-ice–fresh-water system (cf. Figure 5.2, left column: a, b, c) and sea-ice–sea-water system (middle column: d, e, f) for similar shielding, $\mathrm{Ri}_0 = 11$. In both systems, vertical buoyancy production feeds the turbulent kinetic energy in the system (cf. Figure 5.2b,e, black line). Turbulence transports the turbulent kinetic energy away from regions of higher production to regions of lesser production (blue line): to a thin region above the mixed layer and the far field. The pressure strain shifts turbulent kinetic energy from the vertical component to the horizontal (cf. Figure 5.2b,e, green line). Dissipation follows the production of turbulent kinetic energy in each component and follows the turbulent transport next to the wall (red line).

The difference in the turbulent-kinetic-energy budget between fresh-ice–fresh-water system and sea-ice–sea-water systems for similar shielding is evident in

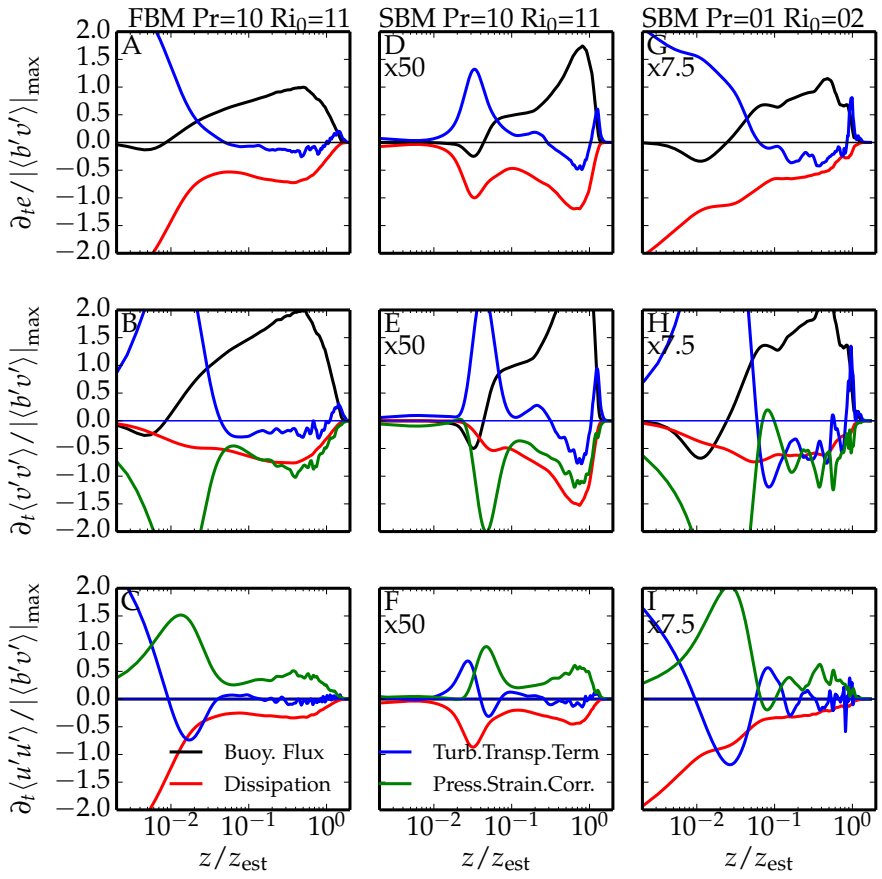

Figure 5.2: Turbulent-kinetic-energy budget of the fresh-ice–fresh-water system (fbm, left) and of the sea-ice–sea-water system (sbm, middle and right). The data is normalised by the maximum buoyancy flux of the fresh-ice–fresh-water system. The first (a,b,c) and second (d,e,f) column compare systems of similar Richardson number, Ri_0. The third column (g,h,i) adds a sea-ice–sea-water system of reduced Richardson number to the comparison. The upper panels (a,d,g) show the terms contributing to the total turbulent-kinetic-energy evolution $\partial_t k$: buoyancy production, $\langle b'v' \rangle$, (black), dissipation, ε, (red), and the turbulent transport term, $\mathcal{T}$, (blue). The panels in the middle (b,e,h) show the terms contributing to the vertical component of the turbulent kinetic energy. The pressure strain correlation (green) moves turbulent kinetic energy from the vertical component to the horizontal component [shown in lower panels (c,f,i)]. Note: The budget of the sea-ice–sea-water systems is blown up by a factor of 50 and 7.5, respectively.

two aspects. First, in the sea-ice–sea-water system the peak intensity is considerably smaller: about a factor of 50. Double diffusion creates a buoyancy reversal instability that is weaker than that of the single-diffusive counterpart, the fresh-ice–fresh-water system. A weaker buoyancy reversal instability results in decreased velocity fluctuations and in decreased buoyancy production. The distorted peak shape is a remaining effect of the initial condition and will equilibrate while the system develops further as will be seen later. Second, as a result of the decreased buoyancy production in the sea-ice–sea-water system, turbulence is transported less intense to the interface.

For a weaker shielding of the sea-ice–sea-water interface, the velocity fluctuations are transported closer to the ice (cf. Figure 5.2, right column: d, e, f). A weaker shielding of the sea-ice–sea-water interface is commensurate with a weaker stabilising salinity gradient across the system compared to the destabilising temperature gradient (cf. Eq. (2.14)). Thus, as the shielding ceases, the stabilising influence by molecular diffusion of salinity also ceases. The diffusion of temperature gains importance compared to the diffusion of salinity. As a consequence, double diffusion creates a stronger buoyancy reversal instability and the buoyancy production increases (cf. Figure 5.2, right column is only amplified by a factor of 7.5 while the middle column is amplified by 50). Both effects contribute to increasing buoyancy production with decreasing shielding strength, Ri_0.

As seen in the fresh-ice–fresh-water system, the sea-ice–sea-water system pursues equipartition of energy with the help of dissipation, the transport of turbulent kinetic energy and its spatial components. The resulting flow structure between ice interface and far field are examined in the following.

5.3 The Flow Structure

Both the normalised temperature and the normalised salinity yield a major change by more than one order of magnitude next to the interface and a constant mixing level away from the interface in the mixed layer (cf. Figure 5.3). The main change next to the interface happens over about the same distance for temperature and salinity. The constant mixing level is, however, a different one for each. Because the change next to the interface happens over the same distance but towards a different constant mixing level, it yields different interfacial gradients. Both the main change next to the interface and the constant mixing levels are a result of different diffusivities and fluxes of temperature and salinity.

The temperature and salinity fluxes across the boundary layer can be attributed to molecular transport and to turbulent transport (cf. Figure 5.4). For example, the magnitude of the temperature flux across the system, $H = \mathbf{He}_3$, is

$$H\left(z,t\right) = -\rho_{\mathrm{water}} c_p \left(\kappa_T \partial_3 \left\langle T\right\rangle \left(z,t\right) - \left\langle v_3' T'\right\rangle \left(z,t\right)\right)$$

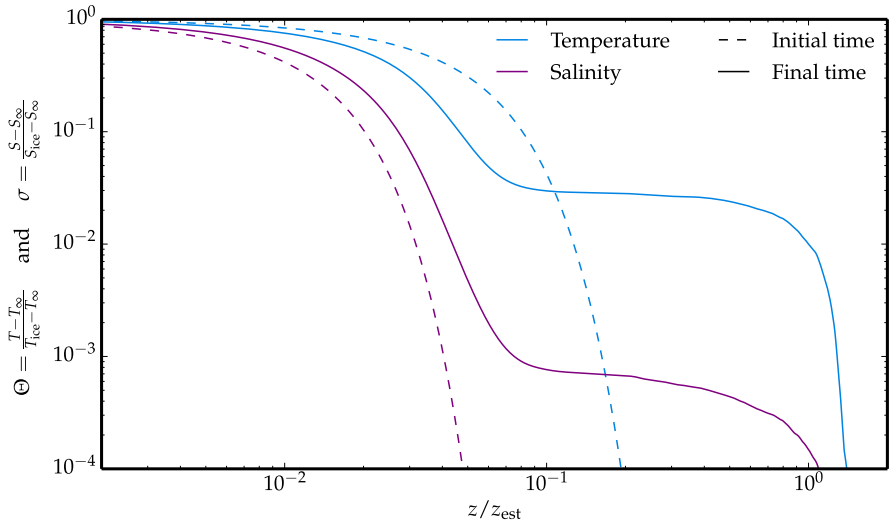

Figure 5.3: Mean profile of normalised temperature, Θ, (red) and normalised salinity, σ, (purple) over distance from the ice interface, z for the simulation at $\mathrm{Pr} = 10$, $\mathrm{Ri} = 11$. The mean profiles are given for two time instances: initial profiles (dashed) and final profiles (solid). The initial mean profiles are error functions. The final mean profiles both exhibit a main change next to the interface and yield a constant mixing level thereafter before they approach the far field. The main change occurs over the same distance for both profiles. The constant mixing level is, however, different. As a consequence, the mean profiles yield different interfacial gradients. z_{est} is evaluated at final simulation time.

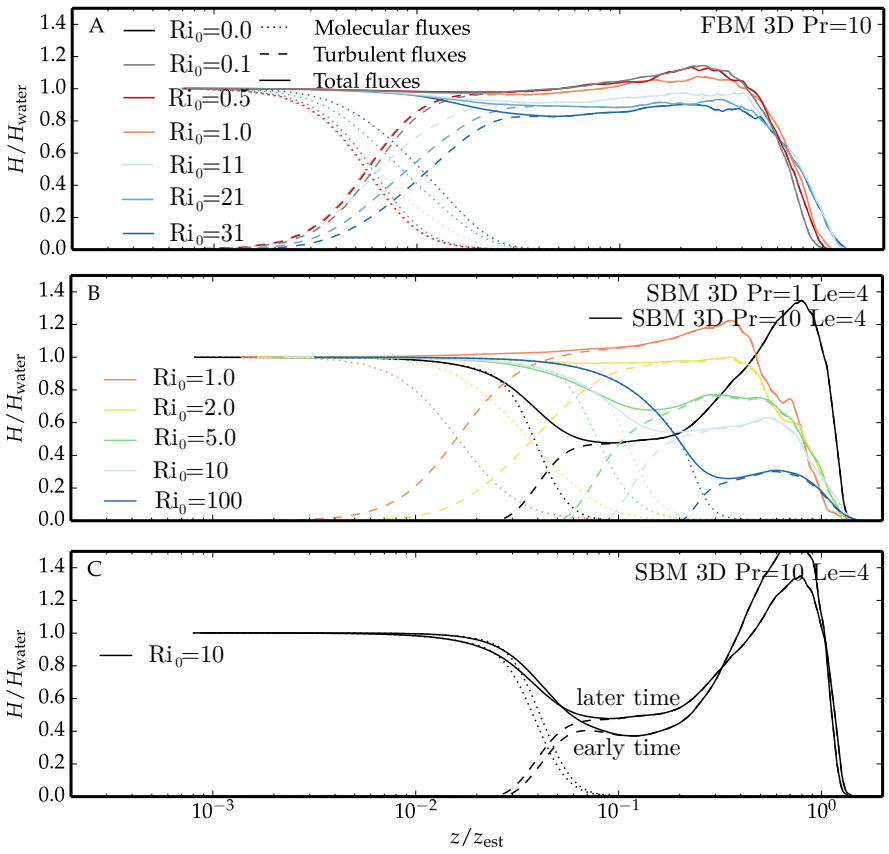

Figure 5.4: Simulated internal-energy flux. Colours indicate different far-field temperatures. Molecular (dotted) and turbulent (dashed) fluxes contribute to the total internal-energy flux (solid). a) Fresh-ice–fresh-water system. b) Ice–ocean system. c) Ice–ocean system. Illustration of the temporal evolution for the simulation at $\mathrm{Pr} = 10$, $\mathrm{Ri}_0 = 11$.

(Eq. (3.3) repeated from page 32). A comparison of the flux attributions in the region where the main change in the profiles occurs and in the region of constant mixing level shows: the transport next to the interface is dominated by molecular transport, the transport away from the interface is dominated turbulent transport.

If the temperature and salinity distributions were in a steady state, no spatial gradients in the flux could be observed (cf. Eq. (3.2)). As opposed to the simulations of the fresh-ice–fresh-water system, the simulations of the sea-ice–sea-water interface hardly seem to have reached this equilibrium. For the fresh-ice–fresh-water systems (cf. Figure 5.4a) the internal-energy flux is constant throughout a diffusion-dominated and a turbulence-dominated region right beneath the interface. The internal-energy flux H only varies about $\pm 0.2\ H_{\text{water}}$. For the sea-ice–sea-water system only simulations of $\text{Ri}_0 = 1$, $\text{Ri}_0 = 2$ and $\text{Ri}_0 = 5$ yield internal-energy fluxes that are about to approach an equilibrium (cf. Figure 5.4b). The internal-energy flux H only varies about $\pm 0.3\ H_{\text{water}}$.

If spatial gradients in the flux remain—as is the case for the simulations of the sea-ice–sea-water system—, the corresponding quantity will change in time towards an equilibrium (cf. Eq. (3.2)). For example, the temperature flux across the boundary layer is directed towards the ice, $\mathbf{H} \cdot \mathbf{e}_3 < 0$, and if vertical gradients of the temperature flux occur, they are mostly positive, $\partial_3 H_{\text{water}} > 0$. Therefore, the temporal gradient of the temperature is negative there, $\partial_t \langle T \rangle < 0$, (cf. Eq. (3.2)) and the interface is hence cooling the boundary layer. The presence of spatial gradients in the flux is expected at the lower boundary of the mixed layer, where warm far-field water is entrained. Next to the interface, however, a steady state of the mean-temperature profile is to be expected in a fully developed system. The simulations for high $\text{Ri}_0 \in \{5, 10, 100\}$ are hence still developing.

The partitioning of the internal-energy flux, H, according to Eq. (3.3) into a molecular flux $-c_p \rho \kappa \partial_3 \langle T \rangle$ (dotted) and a turbulent flux $c_p \rho \langle v_3' T' \rangle$ (dashed) warrants a separate description of the diffusion-dominated inner layer and the turbulence-dominated mixed layer.

5.3.1 The Diffusion-Dominated Inner Layer

Next to the interface, the molecular flux alone determines the transport (cf. Figure 5.4b). Over this molecular-diffusion-dominated inner layer, the main mean-temperature and mean-salinity change is of order $(T_\infty - T_{\text{ice}})$ and $(S_\infty - S_{\text{ice}})$ respectively (cf. Figure 5.3). The resulting gradient diffusively transports internal energy, salt and momentum across the inner layer to the interface. According to the laws of Fick and Fourier, the transport is quantified by this mean change over the extent of the inner layer.

Martin and Kauffman (1977) identify the extent of the inner layer through the edge of the so called 'salinity boundary layer'. They define its height, z_S, by the

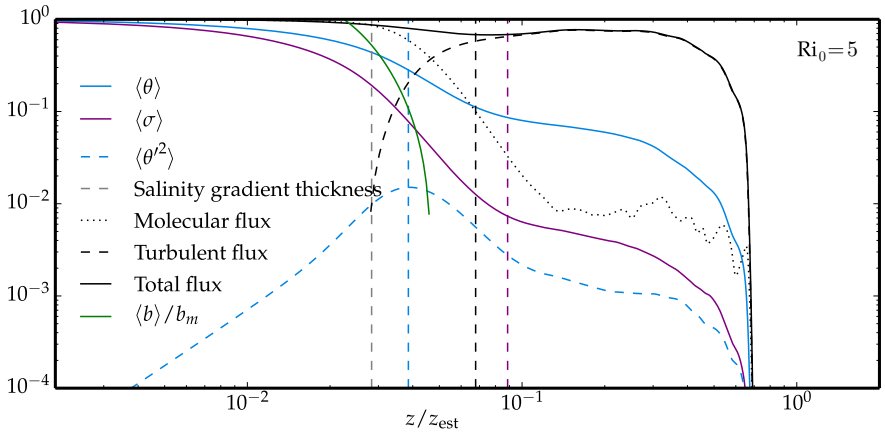

Figure 5.5: Inner-layer extent (vertical dashed lines) according to temperature (red), salinity (purple), buoyancy (green), temperature-fluctuation (red dashed) and internal-energy flux (black, cf. Figure 5.2) profiles of a simulation at $\mathrm{Ri}_0 = 6$. The salinity gradient thickness is indicated by the vertical gray dashed line.

point of occurrence of the maximum of $\langle T'^2\rangle^{1/2}$. There, S has reached its far-field value to within their measuring accuracy. From the consideration that

$$\frac{1}{\rho\left(S_2,T_2\right)}\left.\frac{\partial\rho}{\partial S}\right|_{S_2,T_2}\Delta S \stackrel{!}{=} \frac{1}{\rho\left(S_2,T_2\right)}\left.\frac{\partial\rho}{\partial T}\right|_{S_2,T_2}\Delta T, \tag{5.1a}$$

they find that temperature mainly varies outside of the salinity boundary layer. They also use a temperature difference $\Delta T = (T_\infty - T_2) = 10^{-2}$ °C and $\Delta S = (S_\infty - S_2)$ to define z_S in terms of $S_2 = S\left(z = z_S\right)$. Generally, in free-convection systems the extent of the diffusive wall layer is usually defined by the decline of the buoyancy flux down to 10% of the total flux. That leaves four possibilities for the definition of an diffusion-dominated inner layer extent: (i) where $S = S_2$, (ii) where $\max\left(\langle T'^2\rangle^{1/2}\right)$ occurs, (iii) where the diffusive flux has declined to 10% of the total flux in salinity, temperature or buoyancy and (iv) the salinity gradient thickness $\delta_S = (S_\infty - S_{\mathrm{ice}}) \,/\, \partial_3 S|_{z=0}$.

The inner-layer extent is of the same order of magnitude according to all definitions (i), (ii) and (iii) (cf. Figure 5.5) and evolves similarly in time. The definitions are thus equally valid even though the spread between them ranges between four to one-and-a-half in my simulations depending on the Ri_0. In the following, I will use definition (ii) because it collapses with the height at which the mean-buoyancy profile intersects the value of the far-field buoyancy. This definition is useful in comparing the sea-ice–sea-water system to the fresh-ice–fresh-water system. It matches the extent of the stable-stratification shield next to the ice interface. Furthermore that definition collapses with about the height at which molecular and turbulent flux contributions equal for all of my simulations.

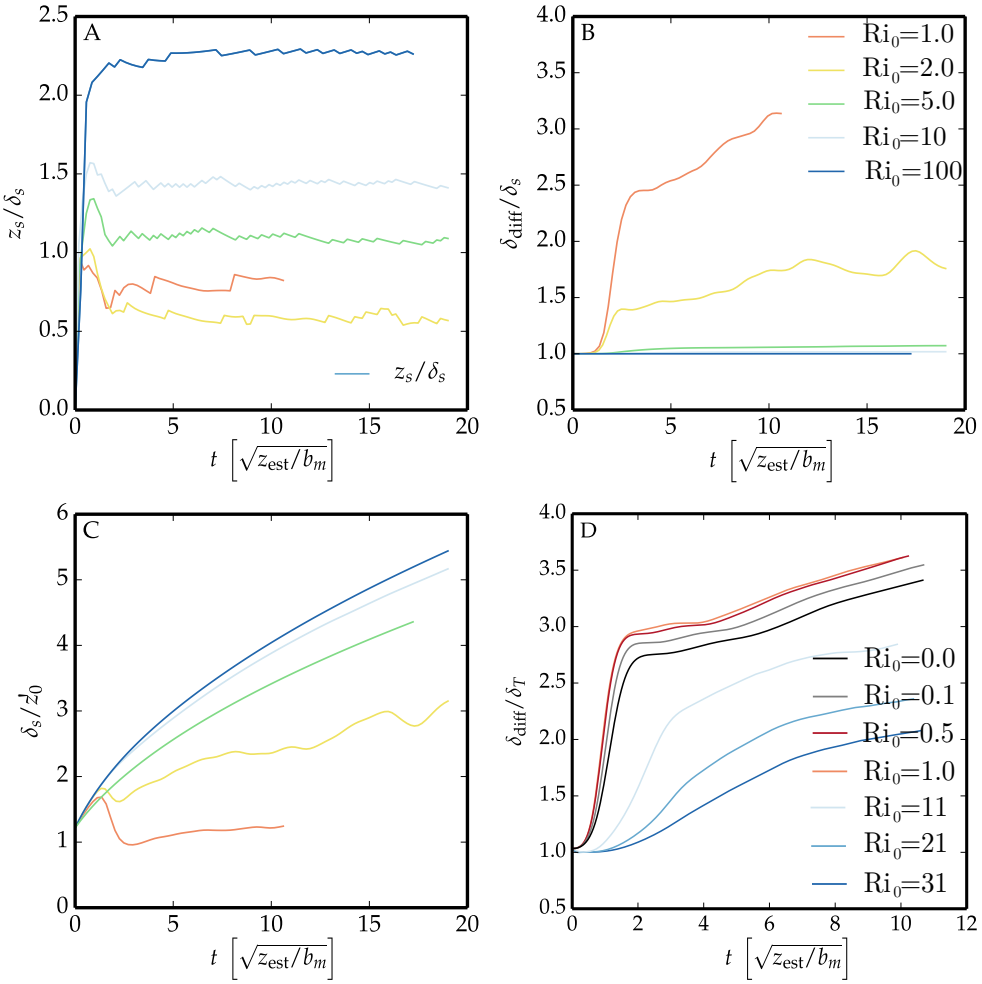

Figure 5.6: a) Temporal evolution of the extent of the salinity boundary layer, z_S, in terms of the salinity gradient thickness δ_S. b) Turbulent enhancement, E, of the non-dimensionalised salinity gradient, δ_S^{-1}, in terms of the non-dimensionalised gradient of a diffusively broadening error function, $\delta_{\text{diff}}^{-1}$. c) Temporal evolution of the salinity gradient thickness, δ_S, in terms of the diffusive length scale, z_0. d) Temporal evolution as in (b) but taken from the temperature gradient thickness of the fresh-ice–fresh-water system, δ_T.

Definition (iv), by the gradient thickness,

$$\delta_\circ = (\circ_\infty - \circ_{\mathrm{ice}}) \,/\, \partial_3 \circ|_{z=0}\,, \tag{5.2}$$

of salinity (with $\circ = S$)[1] is the most direct measure for the extent of a salinity boundary layer. δ_S is still growing as the boundary layer continues to develop. Its growth rate is identical to that of the salinity boundary as defined by (ii) (cf. Figure 5.6a). The non-dimensionalised salinity gradient, $\partial_3 S / (S_\infty - S_{\mathrm{ice}}) = \delta_S^{-1}$, develops diffusively for almost all Ri_0 (cf. Figure 5.6b). A significant enhancement of the gradient is only observed if the Richardson number is very low, $\mathrm{Ri}_0 = 1$ or $\mathrm{Ri}_0 = 2$ (orange line and yellow). Richardson numbers so low correspond to far-field temperatures $T_\infty > 50$ °C according to Figure A.6 for $R \approx 2$ and $S_\infty \approx 34$ g kg^{-1}. In these cases, the enhancement of the gradient follows a similar pattern as has been observed for the fresh-ice–fresh-water interface (cf. Figure 5.6d).

The similarity of the temporal evolution of δ_S to the one of δ_T from fresh-ice–fresh-water interface and the similarity of inner-layer extent, z_S (ii), to the shield of the fresh-ice–fresh-water interface motivates the consideration of z_S in terms of a diffusive length scale. In analogy to Eq. (4.3), I define a diffusive length scale

$$z_0 = \frac{10}{g(\mathrm{Ri}_0)^{2/3}} \mathrm{Pr}^{1/3} \left(\kappa_T^2 / \left|b_m\right|\right)^{1/3}, \tag{5.3}$$

where $g(\mathrm{Ri}_0)$ is the unstable fraction of the diffusive region next to the interface. For the fresh-ice–fresh-water interface, g was analytically determined as $2\chi_m$. For the sea-ice–sea-water interface, g results from the double-diffusive interplay of temperature and salinity.

If g is chosen such that it perfectly represents the unstable fraction under consideration of the vicinity of the wall, then

$$\delta_S / z_0 \overset{!}{=} 1. \tag{5.4}$$

One can then define $z_0' = g^{2/3} z_0$. From the simulation data, I observe an unstable fraction g, $g_{\mathrm{obs}} = \delta_S / z_0'$, of order one (cf. Figure 5.6c). Especially the simulations at high $\mathrm{Ri}_0 \in \{5, 10, 100\}$ have not yet reached a flux equilibrium and they show an enduring growth of the diffusive-sublayer extent (cf. Figure 5.6c). The determined unstable fraction can therefore only be understood as an upper bound to the unstable fraction of the fully developed system, $g_\uparrow = g_{\mathrm{obs}}$.

To circumvent the issue that the systems are mostly still approaching a fully developed state, I make use of evolution of turbulence further away from the interface, in the mixed layer.

[1] The gradient-thickness is identically defined for temperature with $\circ = T$

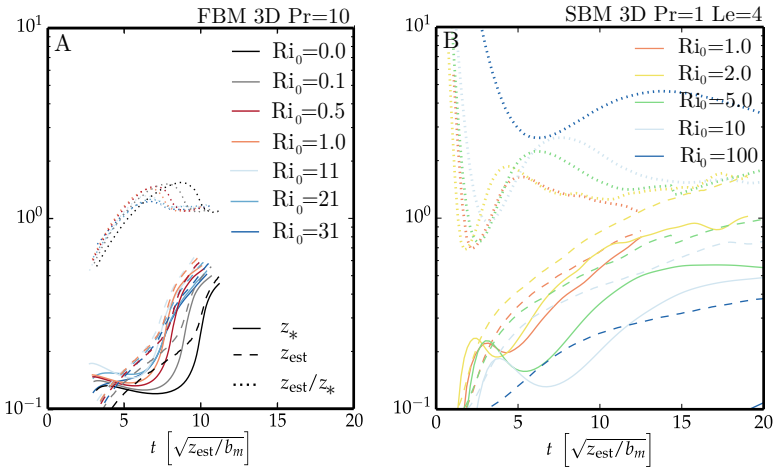

Figure 5.7: Boundary-layer height measured by z_* as defined in Eq. (4.4) (solid) and estimated by z_{est} as defined in Eq. (5.5) (dashed). The fraction z_{est}/z_* (dotted) indicates how well z_* represents z_{est}. a) For the fresh-ice–fresh-water systems of different stable stratification Ri_0, $z_{\text{est}}/z_* \approx 1$. b) For the ice–ocean systems of different stable stratification Ri_0, z_{est}/z_* is constant but depends on Ri_0.

5.3.2 The Turbulence-Dominated Mixed Layer

Away from the interface, the turbulent flux alone determines the transport (cf. Figure 5.4b). The turbulent transport of temperature is now used to assess the boundary layer height and the convective velocity. Both measures will be useful in the discussion of the melt rate in chapter 5.5. The turbulent transport of salinity is used in this section to assess a lower bound for the unstable fraction of the fully developed system.

The length scale z_* is strictly defined as based on the turbulent transport of temperature as in Eq. (4.4) (cf. Figure 5.7, solid). I assess its quality in representing the boundary-layer height with the estimate, z_{est}, defined with the threshold criterion,

$$\langle T\,(z = z_{\text{est}})\rangle = 0.99\; T_\infty. \tag{5.5}$$

The comparison of z_{est} and z_* shows, that z_* is proportional to the boundary-layer height. As opposed to the fresh-ice–fresh-water system, z_{est}/z_* is generally not $\mathcal{O}\,(1)$ nor is it independent of Ri_0 (cf. Figure 5.7b, dotted) (cf. Figure 5.7a). An analogous definition based on the turbulent transport of salinity also proves to be off. The boundary-layer height is estimated better by z_{est}. The temporal evolution of z_{est} is similar in both the fresh-ice–fresh-water system and the sea-ice–sea-water system (cf. Figure 5.7, dashed).

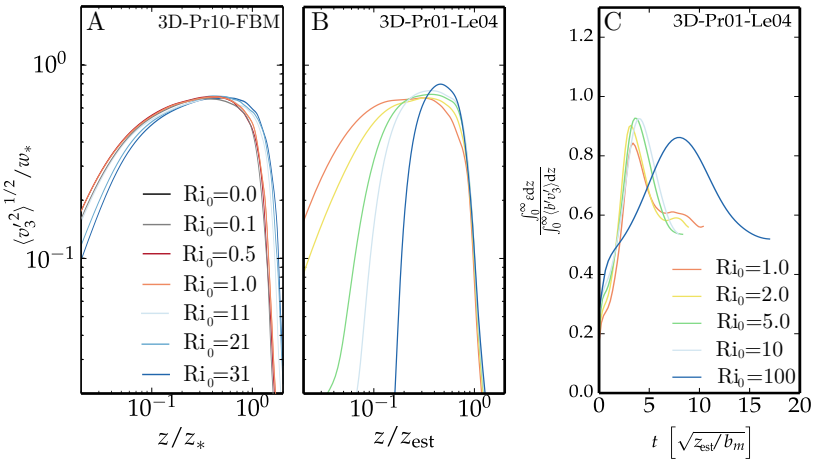

Figure 5.8: a) Velocity root mean square scaled with the convective velocity scale w_* for the fresh-ice–fresh-water systems of different stable stratification Ri_0. b) Same as (a) but for the ice–ocean systems of different stable stratification Ri_0 at $\mathrm{Pr} = 1$. c) Balance between viscous dissipation and turbulent buoyancy production for the ice–ocean systems.

Following the argumentation of the fresh-ice–fresh-water system, I define a convective velocity scale for the sea-ice–sea-water interface, w_*, from the inviscid scaling of the viscous dissipation rate $\varepsilon \propto w_*^3\ z_*^{-1}$ and the balance of the viscous dissipation rate ε and the turbulent buoyancy production $\langle b' v_3' \rangle$:

$$\frac{\int_0^\infty \varepsilon \mathrm{d}z}{\int_0^\infty \langle b' v_3' \rangle \mathrm{d}z} \approx 0.6 \tag{5.6}$$

(cf. Figure 5.8c). I define w_* based on the turbulent buoyancy flux as Eq. (4.5). w_* scales the root-mean-square vertical velocity fluctuations (cf. Figure 5.8b) just as it does for the fresh-ice–fresh-water system (cf. Figure 5.8a). The effective buoyancy flux based on z_{est} and w_* (cf. Eq. (4.7)) is about $0.01\left(b_m^4 \kappa_T\right)^{1/3}$, an order of magnitude smaller than that of the fresh-ice–fresh-water system (not shown).

The transport of salinity across the boundary layer follows a similar pattern as the transport of temperature (cf. Figure 5.9a, solid lines). Next to the interface, the molecular flux alone determines the transport (dotted lines). Away from the interface, the turbulent flux alone determines the transport (dashed lines). The turbulent flux in the mixed layer is significantly smaller than the molecular flux at the interface. As long as the molecular flux dominates the turbulent transport, the transport at the interface dilutes the water next to the interface. As a consequence, the region over which the molecular flux is dominant broadens because diluted water stabilises. If the diffusion-dominated inner layer broadens,

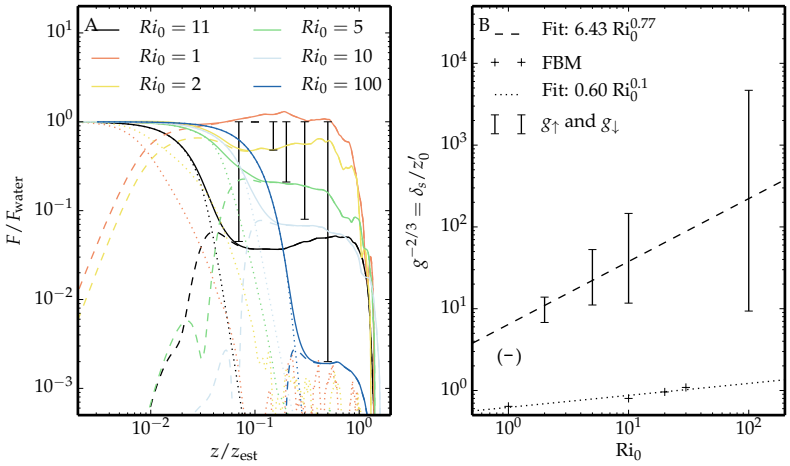

Figure 5.9: a) Simulated salinity flux, F, normalised by the salinity flux at the wall, F_{water}. Molecular (dotted) and turbulent (dashed) fluxes contribute to the total flux (solid). Colours indicate different far-field temperatures. b) The unstable fraction, $g^{-2/3} = \delta_S/z_0'$, as evaluated from the gradient thickness (lower bound of the black bar) and the ratio of salinity flux at the interface and in the far field (upper bound of the black bar). Bars in (a) mark the difference between molecular and turbulent flux. The comparison with the unstable fraction of the fresh-ice–fresh-water system shows, that double diffusion is at least an order of magnitude less effective in producing the buoyancy reversal instability. The least-square power-law fit to upper and lower bound of g neglects the simulation at $\text{Ri}_0 = 1$, because the buoyancy parameterisation here only very vaguely reflects reality.

the molecular flux decreases and the unstable fraction, g, decreases. When the diffusion-dominated inner layer has broadened sufficiently that turbulent flux and molecular flux are in equilibrium, then the dilution is balanced by the turbulent transport of salt from the far-field. The turbulent flux provides a lower bound to which the molecular flux could possibly decrease to reach this equilibrium. The turbulent flux however also increases—slowly—in time. Analogous to the determination of the upper bound of the unstable fraction, $g_\uparrow$, by the molecular flux, the turbulent flux of salinity is now used to determine a lower bound to the unstable fraction, $g_\downarrow$, (cf. Figure 5.9b, bars indicate upper and lower bound).

From the upper and lower bound of the unstable fraction, $g_\uparrow$ and $g_\downarrow$, one realises that a considerably smaller fraction of the diffusion-dominated layer yields a buoyancy reversal instability than in single diffusive counterpart (cf. Figure 5.9b, dashed and dotted lines). Double diffusion is at least an order of magnitude less effective in producing the buoyancy reversal instability. A least-square power-law fit gives an indication how g varies with the shielding strength, Ri_0, for the

simulations for $\mathrm{Pr} = 1$.

$$g_S \left(\mathrm{Ri}_0\right)^{-2/3} = 6.43 \ \mathrm{Ri}_0^{0.77} \tag{5.7}$$

I estimate the extent of the diffusive sublayer from this fit with $\mathrm{Pr} = 1$ as

$$z_0 = 64.3 \ \mathrm{Ri}_0^{0.77} \left(\kappa_T^2 / \left|b_m\right|\right)^{1/3} . \tag{5.8}$$

5.4 Interfacial Equilibrium

The mixed-layer transports heat to the ice interface, thereby ablates it, and dilutes it, but the mixed-layer also transports salt to the ice interface that counteracts the dilution. The interfacial equilibrium between dilution and salt transport yields an interfacial salinity. The temperature of the interface must always be the freezing temperature of this interfacial salinity (cf. Eqs. (A.20)).

Following Gade (1993), the interfacial salinity follows from the boundary conditions, Eqs. (A.20), as

$$S_{\mathrm{ice}} = -\frac{\rho_{\mathrm{ice}}}{\rho_{\mathrm{water}}} \frac{\mathrm{Lat}}{c_p} \frac{\kappa_S}{\kappa_T} \ R \frac{\left(S_\infty - S_{\mathrm{ice}}\right)}{\left(T_\infty - T_{\mathrm{ice}}\right)} \tag{5.9}$$

[cf. Eqs. (A.21–A.26)], where

$$R = \delta_T / \delta_S \tag{5.10}$$

is the gradient-thickness ratio—the ratio between the gradient thicknesses of temperature and of salinity. R describes the effect of the mixing beneath the interface on the interfacial equilibrium.

The fact that the interface conditions can be predicted from the boundary conditions once the effect of the mixing of the ocean is known, has launched several assessments: Josberger (1983) uses a two-layer boundary-layer model and defines the interface conditions based on the ratio of the heat transfer coefficient, C_H, to salinity transfer coefficient, C_S. He introduces C_H and C_S as

$$H = \rho_w c_p C_H \left(T_\infty - T_{\mathrm{ice}}\right) \qquad \text{and} \tag{5.11a}$$

$$F = \rho_w C_S \left(S_\infty - S_{\mathrm{ice}}\right) . \tag{5.11b}$$

From the analogous definitions of the heat flux, H, and the salinity flux, F,

$$H = \rho_w c_p \left(\kappa_T \partial_3 \left\langle T \right\rangle (z,t) - \left\langle \upsilon_3' T' \right\rangle (z,t)\right) , \text{ and} \tag{5.12a}$$

$$F = \rho_w \left(\kappa_S \partial_3 \left\langle S \right\rangle (z,t) - \left\langle \upsilon_3' S' \right\rangle (z,t)\right) , \tag{5.12b}$$

one obtaines the flux ratio, γ,

$$\gamma = \frac{C_H}{C_S} = \frac{H/c_p / \left(T_\infty - T_{\mathrm{ice}}\right)}{F / \left(S_\infty - S_{\mathrm{ice}}\right)} = \frac{\kappa_T \partial_3 \left\langle \theta \right\rangle (z,t) - \left\langle \upsilon_3' \theta' \right\rangle (z,t)}{\kappa_S \partial_3 \left\langle \sigma \right\rangle (z,t) - \left\langle \upsilon_3' \sigma' \right\rangle (z,t)} . \tag{5.13}$$

Notz, McPhee, Worster *et al.* (2003) use only the turbulent contributions of γ to determine the interface conditions. This turbulent-flux ratio, γ_{turb}, is identical to their ratio of turbulent exchange coefficients,

$$\gamma_{\mathrm{turb}} = \frac{\langle \upsilon_3' \theta' \rangle (z,t)}{\langle \upsilon_3' \sigma' \rangle (z,t)}. \tag{5.14}$$

Gade (1993) uses only the molecular contributions of γ at the wall to determine the interface conditions. This molecular-flux ratio, γ_{mol}, is

$$\gamma_{\mathrm{mol}} = \mathrm{Le} \frac{\partial_3 \langle \theta \rangle (z,t)}{\partial_3 \langle \sigma \rangle (z,t)}, \tag{5.15}$$

with $R = \mathrm{Le}\gamma_{\mathrm{mol}}|_{z=0}{}^{-1}$. The approximation to only employ either γ_{mol} at the wall or γ_{turb} in the far-field is reasonable, because there the corresponding contributions to the fluxes dominate numerator and denominator of γ.

The determination of the interface conditions from γ_{turb} is convenient, because it allows for the employment of turbulent-flux measurements from the field. This determination requires, however, that turbulent-flux ratio and molecular-flux ratio at the interface are equivalent. It has been shown that this is not the case for the double-diffusive regime of saltfingering (Zweigle, 2011). In the double-diffusive regime of semiconvection—subject to the present work—, the equivalence of molecular-flux ratio, γ_{mol}, and turbulent-flux ratio, γ_{turb}, is to the author's knowledge untested. It still has to be assessed. The quality of the equivalence of γ_{turb} and γ_{mol} is expressed by the turbulent Lewis number.

The turbulent Lewis number is an effective Lewis number. Just as the Lewis number describes the ratio of diffusivities, $\mathrm{Le} = \kappa_T/\kappa_S$, the turbulent Lewis number [2], τ, describes the ratio of effective diffusivities of temperature, K_T, and salinity, K_S.

$$K_T = -\frac{\langle \upsilon' T' \rangle}{\partial_z \langle T \rangle} \tag{5.16}$$

$$K_S = -\frac{\langle \upsilon' S' \rangle}{\partial_z \langle S \rangle} \tag{5.17}$$

$$\tau = K_T/K_S = \underbrace{\frac{\langle \upsilon' \theta' \rangle}{\langle \upsilon' \sigma' \rangle}}_{\gamma_{\mathrm{turb}}} \underbrace{\frac{\partial_3 \langle \sigma \rangle}{\partial_3 \langle \theta \rangle}}_{\mathrm{Le}\ \gamma_{\mathrm{mol}}{}^{-1}} = \mathrm{Le}\ \gamma_{\mathrm{turb}}/\gamma_{\mathrm{mol}} \tag{5.18}$$

If turbulent Lewis number is unit, then

$$\gamma_{\mathrm{mol}} = \gamma_{\mathrm{turb}}/\mathrm{Le}. \tag{5.19}$$

For the double-diffusive regime of semiconvection, my simulations show that turbulent-flux ratio and molecular-flux ratio are indeed close to identical over

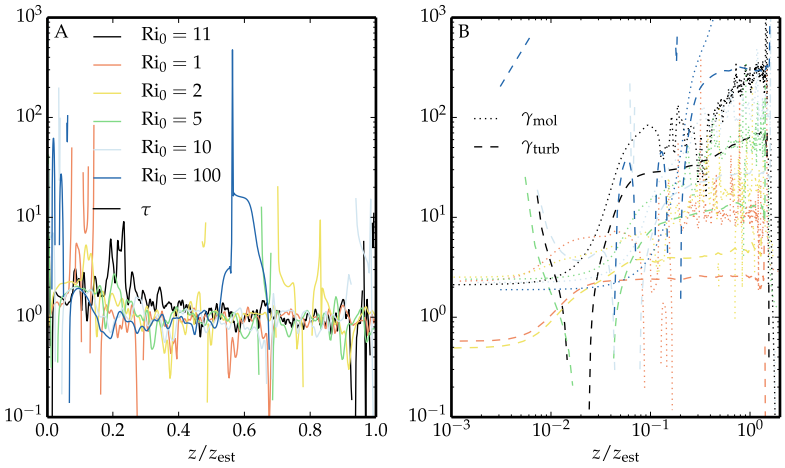

Figure 5.10: a) Turbulent Lewis number, τ, for the simulations at final simulation time. b) Molecular-flux ration, γ_{mol}, and turbulent-flux ratio, γ_{turb} at final simulation time.

a broad range of conditions, $\mathrm{Ri}_0 \in \{1, 2, 5, 10, 100\}$, (cf. Figure 5.10a); The turbulent Lewis number fluctuates around unity. The local fluctuations are due to two things: on the one hand too small a domain to yield statistically converged results (cf. Figure 5.10b). On the second hand, deviations seem to be systematic in parts of the mixed layer. For one, the simulation at $\mathrm{Pr} = 10$, $\mathrm{Ri}_0 = 11$ (cf. Figure 5.10a, black) mostly lingers in-between one and two, partly up to ten.

Even if the turbulent Lewis number is different from unity, it is always true that the molecular contribution to the flux of temperature and salinity in the mixed layer is negligable compared to their respective turbulent contribution:

$$\gamma|_{\text{mixed layer}} \longmapsto \gamma_{\text{turb}}. \tag{5.20}$$

It is also always true that at the interface the turbulent contribution to the flux of temperature and salinity is negligable compared to their respective molecular contribution:

$$\gamma|_{z=0} \longmapsto \gamma_{\text{mol}}. \tag{5.21}$$

The main complication in using γ_{turb} as a measure for H/F arises from the spatial structure of γ (cf. Figure 5.11a). The ratio of flux ratio is different in the mixed layer than and in the diffusive sublayer. At the interface, I find a constant flux ratio, γ, when turbulence is fully developed, independent of the far-field conditions (cf. Figure 5.11a). Away from the interface, I find a flux ratio, γ, that depends on the far-field conditions. γ away from the interface scales with

[2]Turbulent Lewis number τ, not to be confused with the turbulent transport term $\mathcal{T}$

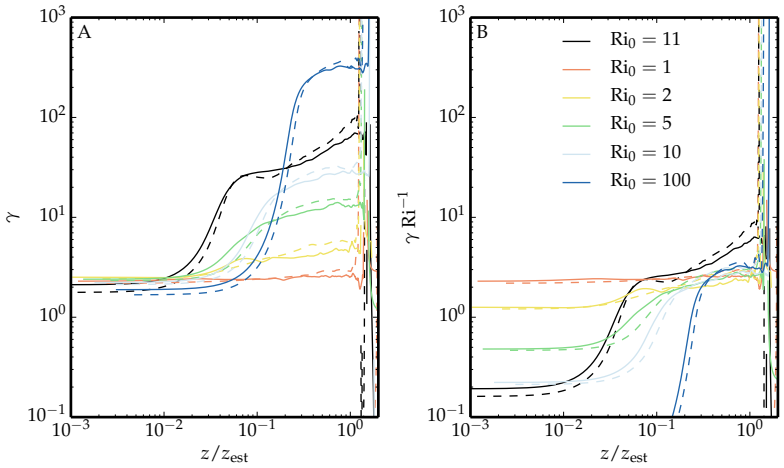

Figure 5.11: a) Ratio between the total transport (molecular + turbulent) of temperature and the total transport of salinity at final simulation time (solid line) and at half time of the simulation (dashed line). γ_{turb} describes this spatial structure well in the mixed layer, γ_{mol} describes it well next to the interface (cf. Figure 5.10b). b) Ratio between the total transport of temperature and the transport of salinity at final simulation time, but scaled with Ri_0^{-1}.

the shielding strength, Ri_0 (cf. Figure 5.11b). This can lead to confusion in the determination of the transport ratio at the interface from γ_{turb}. Currently, γ_{turb} is deemed to be in-between 35 and 70 (Notz, McPhee, Worster *et al.*, 2003), which probably reflects the dependence on the far-field conditions of the measurements.

In the following, I will assess the interfacial equilibrium based on the gradient-thickness ratio, $R = \mathrm{Le}\ \gamma_{\mathrm{mol}}|_{z=0}{}^{-1}$. Two-dimensional and three-dimensional simulation are employed to examine the way in which R varies with $\{\mathrm{Pr}, \mathrm{Le}\}$. In real-world systems, $\mathrm{Pr} = 13.8$, and $\mathrm{Le} = 176$. Here, I approach the real behaviour of R with two sets of simulations. Simulations of $\mathrm{Pr} = 1$ approach the behaviour of varying Le up to 40, and the behaviour of varying Ri_0. Simulations of both $\mathrm{Pr} = 1$ and $\mathrm{Pr} = 10$ on two dimensional grids approach the behaviour of varying Le up to 160. The comparison of two-dimensional and three-dimensional simulation in the next section, follows the assessment of the gradient-thickness ratio, R, and—once determined—the assessment of the interface conditions.

5.4.1 2D Simulations as a Proxy for 3D Simulations

Simulations of a system on a two-dimensional grid take considerably less effort in storage and in computational power than on a three-dimensional grid. Unfortunately, the mean evolution of two-dimensional turbulence does not represent the mean evolution of three-dimensional systems correctly: A fundamental dif-

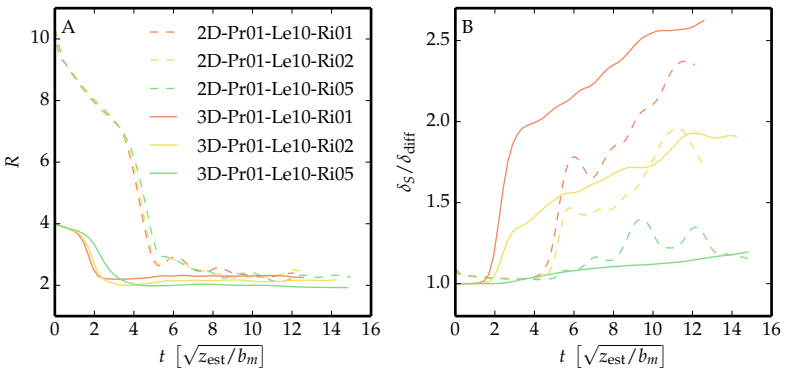

Figure 5.12: Comparison of the interfacial internal-energy and salinity balance between two-dimensional (dashed lines) and three-dimensional (solid) simulations. Despite different initial conditions, two-dimensional and three-dimensional simulations coincide to within 10% regarding their interfacial temperature and salinity fluxes at final simulation time. This is illustrated by coinciding ratio R (a) and coinciding salinity gradient thickness (b).

ference between two-dimensional and three-dimensional turbulence is that the former cannot generate small intense vortices (Tabeling, 2002). Two-dimensional turbulence features an inverse energy cascade to ever larger scales (Kraichnan and Montgomery, 1980).

Nonlinear flow phenomena, such as cascades, coherent structures and dissipative processes, however, take place in both systems and a common conceptual framework between two- and three-dimensional turbulence exists (Tabeling, 2002). It can hence be instructive to employ simulations of two-dimensional turbulence, not only to test the working principle of a setup (cf. Figure A.5), but also to study certain aspects of turbulent systems (Fedorovich, Rotunno and Stevens, 2004). Direct numerical simulation of two-dimensional double-diffusive systems have been employed before (Zweigle, 2011), and have proven to agree in certain respects with three-dimensional simulations (Carpenter, Sommer and Wüest, 2012).

Even though two-dimensional simulations of free convection do not conserve energy and their time evolution is likely to be different, they appear to yield an energy balance at the interface that is to within 10% precise to that of three-dimensional simulations. This has already been observed for simulations of the fresh-ice–fresh-water system (not shown), and it is so for the simulations that have been compared of the sea-ice–sea-water system in both temperature and salinity (cf. Figure 5.12). Carpenter, Sommer and Wüest (2012) have shown that two-dimensional direct numerical simulation “accurately ”captures the heat flux and interfacial structures of three-dimensional direct numerical simulations when the density variation due to salinity is at least three times larger than the

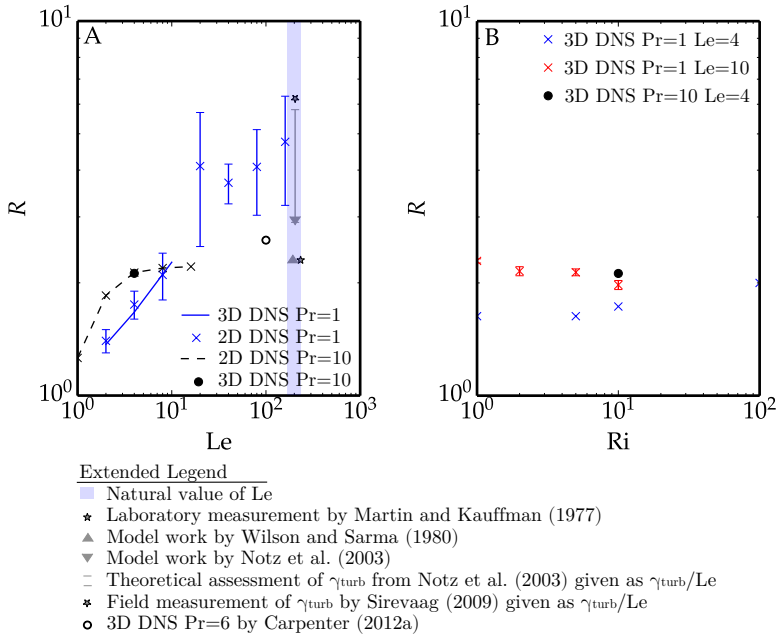

Figure 5.13: Lewis-number series (a) and Richardson-number series (b) of gradient-thickness ratio $R = \delta_T/\delta_S$. a) Three-dimensional simulation series (solid / dot) and two-dimensional simulation series (dashed, crosses) of Pr = 1 (blue) and Pr = 10 (black). b) Three-dimensional simulation series of Pr = 1 and Le = 4 (blue), three-dimensional simulation series of Pr = 1 and Le = 10 (red).

density variation due to temperature (Carpenter and Timmermans, 2013).

I will support my studies by the use two-dimensional simulations as a proxy for expected gradient thicknesses from three-dimensional simulations that are infeasible even with the most recent computational ressources. Still, results arise from three-dimensional simulations in the following if not explicitly stated otherwise.

5.4.2 Determination of the Gradient-Thickness Ratio R

The gradient-thickness ratio, $R = \delta_T/\delta_S$, approaches a constant value long before the system is in a fully developed state. An increase in the gradient thickness of salinity is thus accompanied by an increase in the gradient thickness of temperature and vice versa. An estimate of R may therefore be obtained from the simulation series while they are still developing (cf. Appendix A.6).

The three-dimensional simulation series of Pr = 1, Ri = 10 and varying Le increases in R with increasing Le (cf. Figure 5.13a, blue line): The larger the difference of temperature diffusivity and salinity diffusivity is, the larger the difference in their gradient thicknesses. This evolution agrees to the evolution

of simulations of the same parameter set but on a two-dimensional grid (blue crosses). The two-dimensional simulation series of Pr = 1 and varying Le seems to level off in R for further increasing Le. This evolution agrees to the one of a two-dimensional series of Pr = 10 (black dashed). R first increases and then levels off with increasing Le. The three-dimensional simulation of a water-like fluid of Pr = 10 and Le = 4 agrees with the two-dimensional simulation series of Pr = 10 (black dot). The similar evolution of Pr = 1 and Pr = 10 simulation series in terms of R and the agreement of three-dimensional and two-dimensional simulations in terms of R suggests an extrapolation of R to (2.25 ± 0.10) for a real-world Le = 176.

Gade (1993) interpreted the temperature and salinity profiles found from previous laboratory experiments and model work to determine R. He finds $R = 2.3$ from Martin and Kauffman (1977) with Eq. (A.26) and $R = 2.26$ from Wilson, Sarma and Pritchard (1980). My finding supports this value. I find that the three-dimensional simulation at Pr = 10 and a Lewis number of only Le = 4 already exhibits the near-interface characteristics that are to be expected for Le $\approx$ 200. A report of effective diffusivities that are similar no matter if Le = 100 or Le = 10 is used by (Zweigle, 2011, 87) supports this finding.

My findings oppose previous assessments of the interfacial flux ratio based on the turbulent-flux ratio of Notz, McPhee, Worster *et al.* (2003) and Sirevaag (2009). For a smooth ice interface, the interfacial flux ratio, $\gamma|_{z=0} = \gamma_{\mathrm{mol}}$, is rather $\gamma_{\mathrm{mol}} = \mathrm{Le}\ R^{-1} \in [80; 90]$ than the previously assessed $[35; 70]$. Eventhough the flux ratios determined by Sirevaag (2009) compare well to the values I observe in the mixed layer, these flux ratios do not hold at the interface (cf. Figure 5.11a).

The three-dimensional simulation series of Pr = 1, Le = 4 and varying Ri_0 (cf. Figure 5.13b, blue crosses) and the three-dimensional simulation series of Pr = 1, Le = 10 and varying Ri_0 (red crosses) exhibit values of R around two. R of both series varies little compared to the variation with Le. The three-dimensional simulation of a water-like fluid of Pr = 10 and Le = 4 agrees with both series (black dot) given the shift observed between series of Pr = 1 and Pr = 10 (cf. Figure 5.13a). I conjecture that R does not vary with Ri_0 given a relative standard deviation of only 10% for each simulation series.

5.4.3 Determination of the Interfacial Conditions

With R determined, I provide the interfacial conditions in Figure 5.14 for varying far-field conditions, T_∞ and S_∞, from Eq. (5.9) with an iterative technique (cf. A.4.2).

The interfacial salinity, S_{ice}, decreases with increasing far-field temperature, T_∞, (cf. Figure 5.14a). At first sight, this is plausible: higher temperatures melt more ice and the melt water dilutes the interface. At second sight, it is implausible: higher temperature create more intense mixing and turbulence transports

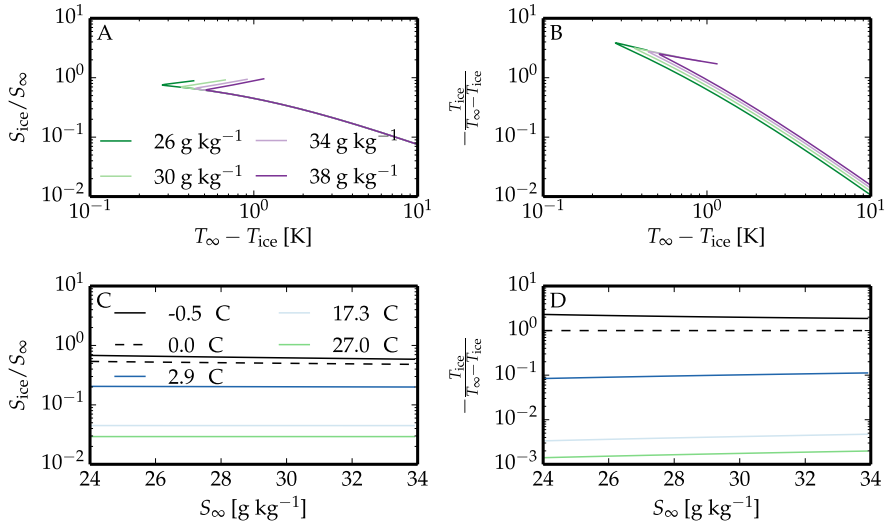

Figure 5.14: Interfacial conditions obtained from Eq. (A.26) with $R = 2.25$. a) Dependence of the interfacial salinity, S_{ice}, on the far-field temperature, T_∞. The interfacial salinity is given in units of the far-field salinity, S_∞. b) Dependence of the interfacial temperature, T_{ice}, on the far-field temperature, T_∞. The interfacial temperature is given in units of the temperature difference $(T_\infty - T_{ice})$. c) Dependence of the interfacial salinity, S_{ice}, on the far-field salinity, S_∞. d) Dependence of the interfacial temperature, T_{ice}, on the far-field salinity, S_∞.

thus more freshwater away from, and more salt to the interface. The truth lies somewhere in-between: salt transport to the interface and dilution pursue an equilibrium. To counteract the stronger dilution at higher far-field temperatures, more salt must be transported to and through the interface. Because the transport of salt at the interface is limited by diffusion, the only way to increase the transport is to increase the difference, $S_\infty - S_{\text{ice}}$, and thus to decrease the interface salinity S_{ice}. Because lower interface salinities imply an increased difference, $T_\infty - T_{\text{ice}}$, via the freezing-point relationship, it also implies an increased transport of temperature. The equilibrium between the transport of temperature and transport of salinity is possible because the relative change to $S_\infty - S_{\text{ice}}$ by a change in S_{ice} is larger than the relative change to $T_\infty - T_{\text{ice}}$ by a change in T_{ice}. This has been described and defined by Eq. (5.9).

The interfacial temperature, T_{ice}, must be at the freezing temperature (cf. Eq. (A.21)). It follows from the interfacial salinity. The interfacial salinity and thus the interfacial temperature hardly vary with the far-field salinity (cf. Figure 5.14c,d).

5.5 The Melt-Rate Parameterisation

The assessment of the flow structure and the interfacial equilibrium in the previous two sections, allows to approach the melt-rate of the sea-ice–sea-water system. The melt rate, w_s, is used as a metric for the internal-energy transport, H_{water}, from the ocean to the ice by neglecting any internal-energy transport through the ice:

$$w_s = \frac{1}{\rho_{\text{ice}} L} H_{\text{water}}.$$

The internal-energy transport is

$$H_{\text{water}} = -\rho_{\text{water}} c_p \kappa_T \, \partial_3 \langle T \rangle \, (z,t)|_{z=0} \,, \tag{5.22}$$

determined solely by the temperature gradient at the ice interface, $\partial_3 \langle T \rangle|_{z=0}$. This temperature gradient can be expressed in terms of the temperature difference between ice interface and the far-field ocean, $(T_\infty - T_{\text{ice}})$, over the gradient thickness, δ_T, (cf. Eq. (5.2)).

$$\partial_3 \langle T \rangle \, (z,t)|_{z=0} = \frac{T_\infty - T_{\text{ice}}}{\delta_T} = \frac{T_\infty - T_{\text{ice}}}{R \delta_S} = \frac{1}{R} \frac{T_\infty - T_{\text{ice}}}{z_0} \tag{5.23}$$

It has been shown that the gradient-thickness ratio, $R = \delta_T / \delta_S = 2.25$, is constant. The gradient thickness of temperature can therefore be expressed in terms of the gradient thickness of salinity which is equivalent to the extent of the diffusive sublayer, z_0, (cf. Eq. (5.4)). I note that the expression derived for z_0 is based on the simulation at a Prandtl number $\text{Pr} = 1$. From the scaling

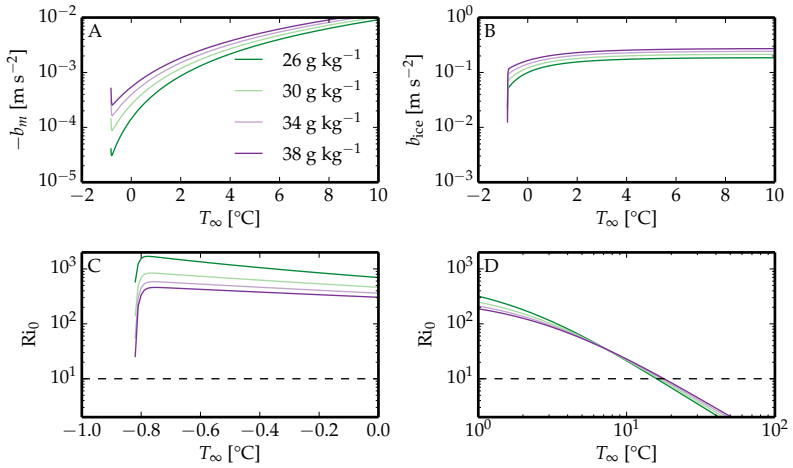

Figure 5.15: Interfacial buoyancy and minimum buoyancy obtained from the interfacial conditions (cf. Figure 5.14). a) Minimum buoyancy, b_m. b) Interfacial buoyancy, b_{ice}. c) Richardson number, Ri_0, for $T_\infty \in [-1, 0]$ °C. d) Ri_0 for $T_\infty \in [1, 100]$ °C.

of the fresh-ice–fresh-water interface and the cloud-top mixing layer, it is to be expected that the temperature gradient scales with $\mathrm{Pr}^{1/3}$. The comparison of these simulations of $\mathrm{Pr} = 1$, $\mathrm{Le} = 4$, $\mathrm{Ri}_0 = 10$ to the one of $\mathrm{Pr} = 10$, $\mathrm{Le} = 4$, $\mathrm{Ri}_0 = 11$ confirms this scaling. In the following I therefore include an additional factor of $\mathrm{Pr}^{1/3}$ in the expression of the temperature gradient, Eq. (5.23). Together with the expression derived for the diffusive-sublayer extent, Eq. (5.8), this yields the melt rate of the sea-ice–sea-water system:

$$w_s = \frac{\mathrm{Pr}^{1/3}}{R\ 64.3} \frac{\rho_{\mathrm{water}}\left(T_\infty\right)}{\rho_{\mathrm{ice}}\left(S_{\mathrm{ice}}\right)} \frac{c_p\left(T_\infty - T_{\mathrm{ice}}\right)}{L} \left(\frac{\left(|b_m|\ \kappa_T\right)}{\mathrm{Ri}_0^{2.31}} \right)^{1/3}, \tag{5.24}$$

for $\mathrm{Pr} = 10$, $R = 2.25$, $\rho_{\mathrm{water}} = 1020$ kg m^{-3} and $\rho_{\mathrm{ice}} = 920$ kg m^{-3}.

The melt rate, w_s, depends on the interfacial conditions, T_{ice} and S_{ice}, via the interfacial buoyancy, b_{ice}, and the minimum buoyancy, b_m, that are implicit to the shielding strength, Ri_0. It is beyond the scope of this work to provide scaling laws for these buoyancy values that are based on the density of sea water (cf. Eq. (2.2)). The buoyancy values, b_{ice} and b_m, and their dependence on the far-field conditions can however be obtained from the solution to the interfacial conditions (cf. Figure 5.14). I provide these buoyancy values in Figure 5.15a,b.

From b_{ice} and b_m, it shows that once the interface is fresh, the interfacial buoyancy, b_{ice}, hardly changes anymore with the far-field temperature (cf. Figure 5.15b); say above 2 °C. It only changes with the far-field salinity and does so equivalently to the change of the minimum buoyancy, b_m, (cf. Figure 5.15a). As a consequence, the Richardson number no longer depends on salinity anymore. The variation of

the minimum buoyancy with the far-field temperature is then the only influence on the Richardson number (cf. Figure 5.15d). Below 2 ℃, the influence of salinity on the Richardson number is as apparent as the influence of temperature.

With T_{ice} from Figure 5.14b, b_m from Figure 5.15a, and Ri_0 from Figure 5.15c&d, I calculate the melt rate of the sea-ice–sea-water system from Eq. (5.24) (cf. Figure 5.16).

5.6 Discussion

The melt rates provided with Figure 5.24 have to be assessed with caution. They have been derived from a Rayleigh-number criterion in analogy to the fresh-ice–fresh-water system. A theory that describes the unstable fraction as in the fresh-ice–fresh-water system is so far unknown. As an approach to the unstable fraction, I have approximated it from numerical simulations of flows at $\mathrm{Pr} = 1$. Even though one simulation at a $\mathrm{Pr} = 10$ supports the results obtained from the former (cf. Figure 5.16,b empty diamond), one should bare in mind that this approximation has a large uncertainty attached (cf. Figure 5.9). Therefore, Eq. (5.24) is not final but a great deal can be learned from it.

The melt rates depend on both the far-field salinity and on the far-field temperature. For high temperatures, the dependence on salinity is lost because, here, salinity variations contribute less to shielding strength, Ri_0, (cf. Figure 5.16a,b). For low temperature, the dependence on salinity can be as important as the dependence on temperature.

For reasonable far-field temperatures of $T_\infty \approx 0$ ℃ the melt rates seem to be of the order of 0.1 mm d^{-1}. Such melt rates are similar to those of diffusive sublayers with an extent of the order of meters. Only if a boundary layer would be considerably larger and fully turbulent, a free-convection-driven enhancement of the melt rate is to be expected. Typical boundary-layer depths in nature range in-between 10 m and 100 m. If the boundary-layer depth is 100 m, a turbulent enhancement of the melt rate to the rates given in Figure 5.16 is plausible. If the boundary-layer depths is 10 m, a turbulent enhancement of the melt rate will only occur for Richardson number, Ri_0, smaller than 100 (cf. Figure 5.16c). Only then a scale separation of an order of magnitude or more prevails. A Richardson number below 100 corresponds to far-field temperature of three degrees Celsius or more. These conditions would only occur in nature if a floe of ice happened to travel over extraordinary warm water. Hence, free-convection boundary layers of a depth of the order of $\mathcal{O}\left(10^1 \text{ m}\right)$ are likely to feature diffusive energy exchange at the interface.

Even if the boundary layer is not sufficiently deep to evolve turbulently by free convection, other driving mechanisms, such as shear or internal heating from radiation, can promote a turbulent enhancement of the melt rate. To allow for the

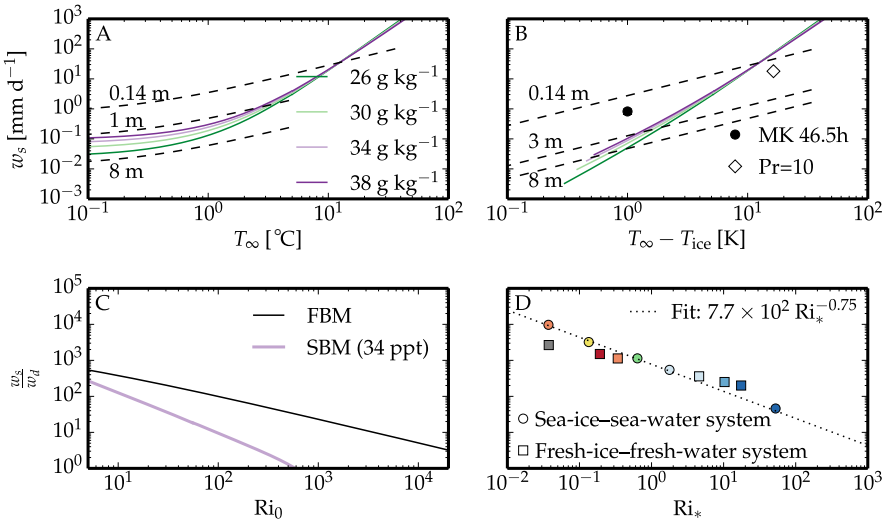

Figure 5.16: a) Melt rate as a function of the far-field temperature, T_∞, and far-field salinity, S_∞, as given in Eq. (5.24). Diffusive melt rates for $S_{ice} = 5$ g kg^{-1}, according $T_{ice} = 5$, and boundary layers of thicknesses 0.14 m, 1 m and 8 m provide a reference (dashed lines). b) Melt rate as a function of $(T_\infty - T_{ice})$, and S_∞, Diffusive melt rates for boundary layers of thicknesses 0.14 m, 3 m and 8 m provide a reference (dashed lines). The black dot is the melt rate derived from the temperature profile of the experiment of Martin and Kauffman (1977) at time 46.5h. A fairer comparison can be found in the appendix where the melt rate is given for a NaCl solution of 38 g kg^{-1} (cf. B.4). The empty square is melt rate of the simulation Pr = 10, Le = 4, Ri = 11. The simulation is still in a developing stage. Consistently, the observed melt rate is lower than the melt rates predicted for the fully developed system. c) Turbulent enhancement of the melt rate compared to the diffusive melt rate w_d of a boundary layer thickness of 10 m (cf. Eq. (3.7)) over Richardson number Ri$_0$ (cf. Eq. (4.18)): fresh-ice–fresh-water system (black line) and sea-ice–sea-water system of 34 g kg^{-1} (pink). d) Turbulent enhancement of the melt rate over the convective Richardson number Ri$_*$ (cf. Eq. (4.20)) with the simulations of the fresh-ice–fresh–water system and of the sea-ice–sea-water system. A linear fit of the final-simulation values of the sea-ice–sea-water system, $\log(w_f/w_d)$ over $\log(\mathrm{Ri}_*)$, gives the fitted curve (dotted line).

comparison of my results to those of systems with different driving mechanisms, I have proposed the use of the convective Richardson number, Ri_*, based on the study of the fresh-ice–fresh-water system in chapter 4. The simulations of different stable-stratification strength have so far been interpreted as simulations of varying far-field conditions (cf. Figure 5.15c,d). As for the fresh-ice–fresh-water system, they can also be interpreted as simulations of fixed stable stratification but varying convective velocity.

Simulations of varying $\mathrm{Ri}_* \propto w_*^{-2}$ behave qualitatively similar to those of the fresh-ice–fresh-water system (cf. Figure 5.16d, coloured squares): The stronger the convective velocity is, the higher the enhancement of the melt rate (coloured dots). From a linear fit of the values $\log(w_f/w_d)$ over final-simulation values of $\log(\mathrm{Ri}_*)$, I conjecture that the melt rate follows Ri_* as

$$w_s = \text{const.} \times \mathrm{Ri}_*^{-0.75} \tag{5.25}$$

(dotted line). The influence of the convective velocity on the melt rates is stronger for the sea-ice–sea-water system than for the fresh-ice–fresh-water system.

With the interpretation of the simulations in terms of the convective Richardson number, the relevance of melt-water advection can be assessed for the sea-ice–sea-water system based on the simulations of the fresh-ice–fresh-water system. For the fresh-ice–fresh-water system, melt-water advection did not affect the melt rates for $\chi_m < 0.8$. The simulation at $\chi_m = .76$ is just beneath that threshold (cf. Figure 5.16d, grey square). Because the influence of the convective velocity on the melt rate is stronger in the sea-ice–sea-water system, the melt rates for a shear-driven melting of similar relative convective velocity, i.e. similar Ri_*, are larger. Consequently, the sea-ice–sea-water system is already affected by melt-water advection for lower convective velocities than the fresh-ice–fresh-water system. Melt rates, for which the influence of melt-water advection cannot be ruled out, occur here for $\mathrm{Ri}_* < 0.2$.

Chapter 6

Conclusions

This work is a combined laboratory and numerical study on the effect of buoyancy-driven turbulence on the heat flux to a horizontal ice–water interface. Buoyancy-driven turbulence beneath an ice–ocean interface mainly depends on the combination of three processes: the presence of an ice interface next to turbulence, the buoyancy reversal instability that intrinsically drives any ice–ocean boundary layer, and double diffusion. In this work, I have approached the processes one after another. Two methodological questions had to be addressed first, before the two main questions have been tackled and answered thereafter.

How can the three processes involved in the turbulent mixing beneath ice be studied independently from each other? The diffusive sublayer between any interface and turbulent convection is a well studied aspect, and the posed question reduces to that of the separation of the remaining two processes: the buoyancy reversal instability and double diffusion. I have demonstrated the fresh-ice–fresh-water system as an idealised setup and framework. The idealisation simplifies the research subject and reduces the number of independent control parameters without changing the qualitative structure of the mean-buoyancy profile. The well-defined and well-controllable framework depends only on its far-field temperature and allows me to study wall-bounded turbulence that arises from the buoyancy reversal instability without the occurrence of double diffusion. I have applied the framework successfully in the following in laboratory and simulations.

Can direct numerical simulations be used to reproduce and complement laboratory experiments? In its core, the question encompasses whether or not the physical model involved in the direct numerical simulation is valid. The validity of the physical model is assessed in two parts: First, I ask: How do the melt rates of laboratory and simulation compare? Second, I ask: How does the temporal evolution of their mean-temperature profile compare? The melt rates agree quantitatively and the structure of the flow differs insignificantly. Thus, the physical model is sound and I complement the temperature profile from the laboratory experiment with the temperature and flow fields of the direct numer-

ical simulations. The simulations are spatially and temporally higher resolved and provide comprehensive statistics. This advantage has subsequently allowed me to solve, first, the questions on the idealised setup, and, second, the questions on the full setup including double diffusion.

How does the buoyancy reversal instability influence the flow structure of free convection next to the ice interface? The simulations show that molecular diffusion sets and limits the energy exchange at the ice interface, just as seen for linear-buoyancy-driven free convection next to any smooth interface under Dirichlet conditions. Deviating from linear-buoyancy free convection, free convection with the buoyancy reversal instability imprints on the flow structure. The diffusive sublayer of the former is quasi replaced by the inversion layer of the latter. As a consequence, the extent of the diffusive sublayer decreases with increasing far-field temperature. In the limit of high far-field temperatures the diffusive-sublayer extent is similar to that of linear-buoyancy free convection. The presence of the ice interface next to the buoyancy reversal instability reflects in a factor of two to the diffusive-sublayer extent. That factor linearly decreases down to one as the high-temperature limit is approached. The increased extent of the diffusive sublayer decreases the effective surface buoyancy flux as well as the surface heat flux. I have identify the extended diffusive sublayer as a stably stratified shield of the ice against the turbulent outer layer. The effect of the stably stratified shield is characterised by a Richardson number, Ri_0. This understanding allows me to derive an analytical expression for the melt rate w_f of ice under purely thermally driven conditions from first principles. The meltrate has been discussed in the context of more general systems, investigating in particular the impact of melt water on the flow, the spatial homogeneity of the melt rate and estimating the effect of salinity on the derived melt rates. The meltrate has been discussed in the context of more general systems: The impact of melt water on the flow shows to be only relevant for far-field temperature larger 15℃. The spatial homogeneity of the melt rate is characterised by its probability density function, which shows relative standard deviations of up to 60 %. The effect of salinity on the melt rate can be estimated from this setup with the introduction of the Richardson number, Ri_0.

How does double diffusion influence the flow structure of free convection next to an interface? For the first time ever, a fully resolving simulation of the physical processes beneath the horizontal sea-ice–sea-water interface is performed to answer this question. The simulations show that molecular diffusion sets and limits the energy exchange at the ice interface, just as seen for the idealised setup: With increasing strength of the stably stratified shield, the diffusive sublayer broadens. In the presence of double diffusion, however, the stably stratified shield is more efficient in protecting the ice from turbulence. As a consequence, the diffusive-sublayer extent is significantly increased over that of the idealised setup and the fluxes of heat, salt and momentum to the interface are reduced: The melt rate is decreased. I assess the two following questions

that have hindered the determination of the energy transport across the diffusive sublayer so far. How much is the diffusive-sublayer extent increased compared to that the idealised setup? The diffusive-sublayer is increased by a factor of 10 for $\mathrm{Ri}_0 = \mathcal{O}(1)$. The diffusive-sublayer is increased by a factor of 200 for $\mathrm{Ri}_0 = \mathcal{O}(100)$. An assessment of the unstable fraction of the diffusive sublayer is given that provides the broadening. For (very) low Ri_0, both systems are mainly thermally driven and the role of the stably stratified shield is negligible compared to the influence of the wall on the flow. For high Ri_0, both systems are mainly determined by the influence of the stably stratified shield. Besides the extent of the diffusive sublayer, the interfacial conditions also need to be known. What are the interfacial conditions between ice and the diffusive sublayer? The interfacial conditions are determined tby he flux ratio between heat transport and salt transport across the diffusive sublayer. I find that the flux ratio is mostly independent of the diffusive-sublayer extent. As opposed to previous research methods, the flux ratio, γ is readily obtained as a simulation outcome: $\gamma = \mathrm{Le}/2.12 = 94$ with $\mathrm{Le} = 200$. From the evolution of γ with increasing Le, I have strong indications that the real-world value will not play within the previously assessed interval of $[35, 70]$ but above. With the determination of the flux ratio, this work provides physically sound interfacial temperatures and salinities in Figure 5.14. With these two questions answered, I provide approximations to the melt rate in Figure 5.16.

Appendix A

Analytical Considerations

In this appendix, some analytical considerations are recorded that have been essential for the development of the fifth chapter. In the pursuit of an analogous presentation of chapter four and five, however, these considerations seemed interuptive. They are appended in the following.

A.1 The Buoyancy

The buoyancy Eq. (2.1) is a function of the density Eq. (2.2). The density is mainly effected by the salinity S of a fluid particle. For a typical ice–ocean system, $T_\infty \approx 0$ ℃ , $T_{\text{ice}} \approx -1.0$ ℃ and $S_\infty \approx 36$ g kg^{-1} and $S_{\text{ice}} \approx 18$ g kg^{-1}, the largest relative buoyancy sensitivities found are at the order of

$$\frac{1}{\rho\left(S_{\text{ice}}, T_{\text{ice}}\right)} \left.\frac{\partial \rho}{\partial S}\right|_{S_{\text{ice}}, T_{\text{ice}}} = 8.0 \times 10^{-4} \text{ g}^{-1} \text{ kg} \tag{A.1a}$$

$$\frac{1}{\rho\left(S_\infty, T_\infty\right)} \left.\frac{\partial \rho}{\partial T}\right|_{S_\infty, T_\infty} = -5.6 \times 10^{-5} \text{ ℃}^{-1}. \tag{A.1b}$$

A temperature variation of order $T_{\text{ice}} - T_\infty$ yields a relative density variation of order 8.4×10^{-5}. A similar relative density variation is already achieved for a salinity variation of $\frac{7}{1000}\left(S_{\text{ice}} - S_\infty\right)$.

The resulting variations of buoyancy that occur within the parameter space (S, T), is consequently largest for salinity variations. This variation is well-captured with a first-order approximation for any temperature $\tilde{\theta}$ (cf. Figure A.1a).

$$\left.\frac{b}{b_m}\right|_{\theta=\tilde{\theta}} \approx -\alpha_S \sigma, \tag{A.2}$$

with $\alpha_S = \left(\rho\left(S_{\text{ice}}, T_\infty\right) - \rho\left(S_\infty, T_\infty\right)\right) / \left|\rho\left(S_\infty, T_{\text{ice}}\right) - \rho\left(S_\infty, T_\infty\right)\right|$. The variation of buoyancy that occur for temperature variations is more subtle. This can

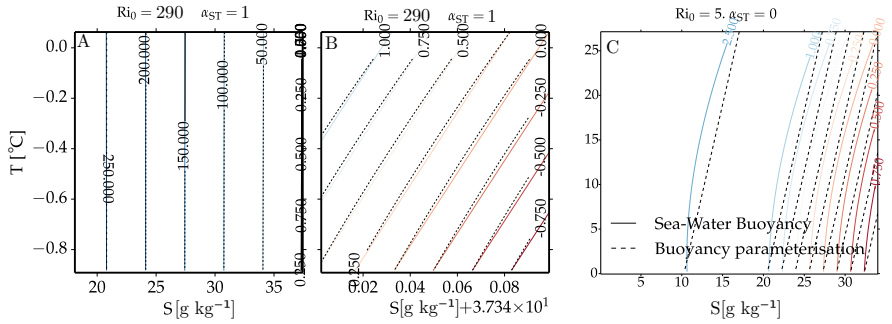

Figure A.1: a) Relative buoyancy b/b_m given as contour lines over the full parameter range (S,T) of interest for a common scenario of $\alpha_S = 290$. The buoyancy derived from Eq. (2.2) (solid lines) matches the buoyancy parameterisation Eq. (A.6) (coloured lines). b) Magnification of (a) in the parameter range close to $b/b_m = 1$. c) As (a) but for significantly smaller α_S, $\alpha_S = 5$.

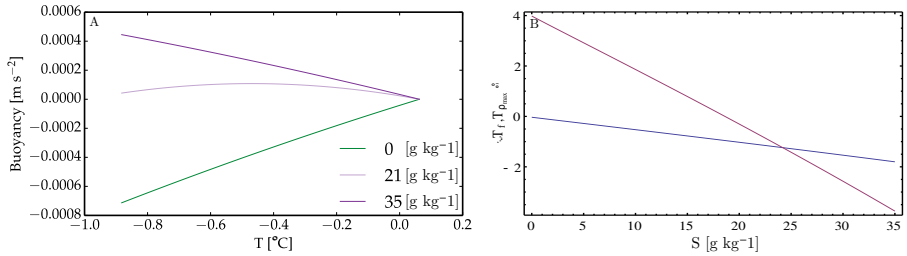

Figure A.2: a) Buoyancy $b\left(\tilde{S}, T\right)$ for constant salinity $\tilde{S} \in \{0, 21, 35\}$ g kg^{-1}. The buoyancy of 21 g kg^{-1} is blown up by a factor of 5. b) Temperature of maximum density (red) and freezing temperature of ice (blue) over salinity. Temperatures are given in ℃.

be infered from $b\left(\tilde{S},T\right)\Big|_{\tilde{S}\in\{0,21,35\}\ \mathrm{g\ kg^{-1}}}$ (cf. Figure A.2a). The temperature of maximum density varies with salinity (cf. Figure A.2b) and needs to be represented depending on the salinity. I introduce a parameterisation of buoyancy as

$$\frac{b}{b_m} = -\alpha_S\ \sigma + \alpha_T\left(\sigma\right)\theta, \tag{A.3}$$

where $\alpha_T\left(\sigma\right)$ accounts for the variation of maximum density.

A.1.1 Buoyancy Parameterisation

The buoyancy parameterisation that I am looking for shall thus meet the following requirements.

$$\frac{b}{b_m} \underset{(S,T)=(S_\infty,T_\infty)}{\longrightarrow} 0 \tag{A.4a}$$

$$\frac{b}{b_m} \underset{(S,T)=(S_\infty,T_{\mathrm{ice}})}{\longmapsto} 1 \tag{A.4b}$$

$$\frac{b}{b_m} \underset{S=S_{\mathrm{ice}}}{\longmapsto} -\alpha_S \tag{A.4c}$$

Hence,

$$\alpha_T\left(\sigma\right) = \frac{S - S_{\mathrm{ice}}}{S_\infty - S_{\mathrm{ice}}} = 1 - \sigma \tag{A.5}$$

and

$$\frac{b}{b_m} = -\alpha_S\ \sigma + \theta - \sigma\ \theta \tag{A.6a}$$

$$\alpha_S = \frac{\rho\left(S_{\mathrm{ice}},T_\infty\right) - \rho\left(S_\infty,T_\infty\right)}{\left|\rho\left(S_\infty,T_{\mathrm{ice}}\right) - \rho\left(S_\infty,T_\infty\right)\right|} \tag{A.6b}$$

For $\alpha_S = 290$ the deviations between Eq. (2.2) and Eq. (A.6) are indistinguishable by eye when the full parameter space is observed (cf. Figure A.1a). Slight deviations only appear for salinities close to S_∞ (cf. Figure A.1b). Caution is advised when low values of $\alpha_S < 10$ are to be investigated. Then the deviations between Eq. (2.2) and Eq. (A.6) become apparent. The smaller α_S is, the more pronounced the curvature of iso-buoyancy lines in the parametric plot (cf. Figure A.1c).

It shows that the simpler buoyancy parameterisation,

$$\begin{aligned}\frac{b}{b_m} &= -\left(\alpha_S + 1\right)\ \sigma + \theta = \\ &= -\mathrm{Ri}_0\ \sigma + \theta,\end{aligned} \tag{A.7}$$

also satisfies Eq. (A.4) except for

$$\frac{b}{b_m} \underset{(S,T)=(S_{\text{ice}},T_\infty)}{\longmapsto} -\alpha_S. \tag{A.8}$$

The parameter combination $\{S_{\text{ice}}, T_\infty\}$, however, is never expected to occur due to the significantly smaller diffusivity of salinity. Eq. (A.8) can therefore be removed from requirements Eq. (A.4). The resulting parameterisation, Eq. (A.7), matches the data better in the relevent region of the paramter space and approximates it well, even for small Richardson numbers down to 5 and 2 (cf. Figure A.1c). Similar parameterisations have been employed before, for example by (Zweigle, 2011, 21) and by Carpenter, Sommer and Wüest (2012).

A.1.2 Explicit Expression for the Buoyancy Parameters

In analogy to the analysis of the fresh-ice–fresh-water setup, I define the strength of the buoyancy forcing b_m with respect to the strength of the stable stratification next to the ice b_{ice}.

$$b_m = b\left(S_\infty, T_{\text{ice}}\right) \tag{A.9a}$$
$$b_{\text{ice}} = b\left(S_{\text{ice}}, T_{\text{ice}}\right) \tag{A.9b}$$

The best approximation to the buoyancy b is given by a high-order polynomial that depends on both temperature and salinity (cf. Eqs. (2.2, 2.1)). A sufficiently good approximation is obtained by a fresh-water-like temperature dependence with a variable maximum-density temperature $T_m\left(S\right)$ and a linear salinity dependence in density.

$$\rho_{\text{fit}} = \rho_S \cdot \Delta\rho_T \tag{A.10a}$$
$$\rho_S\left(S\right) = c_1 + c_2 S \tag{A.10b}$$
$$\Delta\rho_T\left(T,S\right) = 1 - c_3(T - T_m\left(S\right))^2 \tag{A.10c}$$
$$T_m\left(S\right) = \tilde{T}_m - c_4 S \tag{A.10d}$$

With the definitions Eq. (A.9), I obtain

$$b_{m,\text{calc}} = -g c_3 \left(T_\infty - T_{\text{ice}}\right)\left(T_\infty + T_{\text{ice}} - 2T_m\right) \,\& \tag{A.11}$$
$$b_{\text{ice,calc}} = \frac{g}{\rho} c_2 \left(S_{\text{ice}} - S_\infty\right) + \mathcal{O}\left(0.1\ b_{\text{ice}}\right). \tag{A.12}$$

from this approximation (cf. Eq. (A.10)). In general this formulation of b_m and b_{ice} yields relative deviations from Eq. (A.10) smaller than 5% (cf. Figure A.3) for the parameter range of interest. Caution is advised for b_{ice} when uncommonly high far-field temperatures $T_\infty > 6$ °C are to be considered because relative deviations then exceed 10% (cf. Figure A.3b).

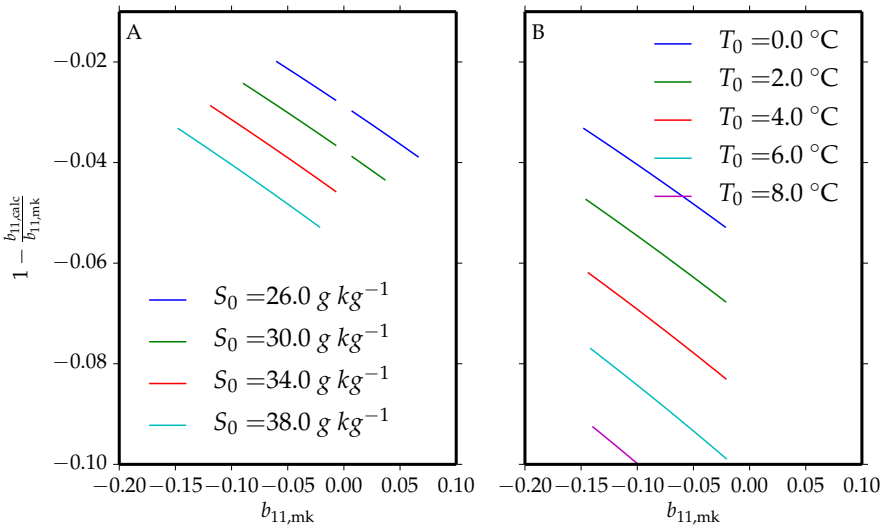

Figure A.3: Comparison of the approximation of b_{ice}, $b_{\mathrm{ice,calc}}$ (cf. Eq. (A.12)), to the full expression that results from Eq. (A.10) for variations of interfacial salinity in the relevant parameter range. a) Far-field salinity is varied in the relevant parameter range. Relative deviation of $b_{\mathrm{ice,calc}}$ to $b_{\mathrm{ice,MK}}$ as obtained from Eq. (A.10). d) Far-field temperature is varied in the relevant parameter range. Relative deviation of $b_{\mathrm{ice,calc}}$ to $b_{\mathrm{ice,MK}}$ as obtained from Eq. (A.10).

A.2 Two-Dimensional Proof-Of-Concept Study: Creation of the Buoyancy Reversal Instability by Double Diffusion

The mixing as a consequence of different diffusivities is called double diffusive (Turner, 1974). Before I studied the impact of double-diffusive mixing on the melting of ice, I have verified that the simulations reproduce the buoyancy reversal instability by double diffusion based on the chosen buoyancy parameterisation. Here, I depict the working principle in an averaged sense and demonstrate it with two-dimensional simulations.

If temperature and salinity mix equally well, then

$$\frac{\langle S\rangle\,(z') - S_\infty}{S_\mathrm{ice} - S_\infty} \overset{!}{=} \frac{\langle T\rangle\,(z') - T_\infty}{T_\mathrm{ice} - T_\infty}. \tag{A.13}$$

Hence, the mean-buoyancy profile along z maps to that of a diagonal line connecting (S_∞, T_∞) and $(S_\mathrm{ice}, T_\mathrm{ice})$ in a parametric plot (cf. Figure A.4a, solid line). Consequently, if temperature and salinity mix differently well, the mean-buoyancy profile maps to that of a curved path (cf. Figure A.4a, dotted and dashed lines). Temperature has the larger diffusivity, $\kappa_t > \kappa_s$, and is the destabilising agent (cf. Eq. (2.14)). Temperature will therefore always mix more efficiently and its mixing will curve the path towards the point of the instability $b_m = b\,(S_\infty, T_\mathrm{ice})$. If the curvature is sufficient to exceed the contour line of $b/b_m = 0$, the buoyancy reversal instability occurs (cf. Figure A.4b, dotted and dashed lines crossing the orange line). The exact path in the parametric plot is subject to the solution of the two advection–diffusion equations, Eq. (2.5c) and Eq. (2.5d).

Neglecting the advection terms in Eq. (2.5c) and Eq. (2.5d), one obtains a mean-buoyancy profile that depends only on the diffusivities of temperature and salinity, κ_t and κ_s. The mean-buoyancy profile then evolves as follows. Close to the interface, $\mathrm{Ri}_0\ \sigma$ is always larger than the normalised temperature Θ, because $\sigma \approx 1$, $\theta \approx 1$ and $\mathrm{Ri}_0 > 1$ [cf. Eq. (2.14)]. Here, the buoyancy follows the diffusive advancement of the normalised salinity σ. Away from the interface, Θ inevitably becomes larger than $\mathrm{Ri}_0\ \sigma$, because temperature diffusively advances faster than salinity with $\kappa_t > \kappa_s$. There, the buoyancy follows the diffusive advancement of Θ and becomes negative (cf. Eq. (2.14)). This is the origin of the buoyancy reversal instability. The diffusive advancement of Θ compared to that of σ,

$$\left(\frac{\kappa_t}{\kappa_s}\right)^{1/2} = \mathrm{Le}^{1/2}, \tag{A.14}$$

—square root of the so called Lewis number, Le—scales the maximum strength of the domain-wide buoyancy reversal instability .

Accounting for the advection term in Eq. (2.5c) and Eq. (2.5d), one obtains a mean-buoyancy profile that depends not only on the diffusivities of temperature

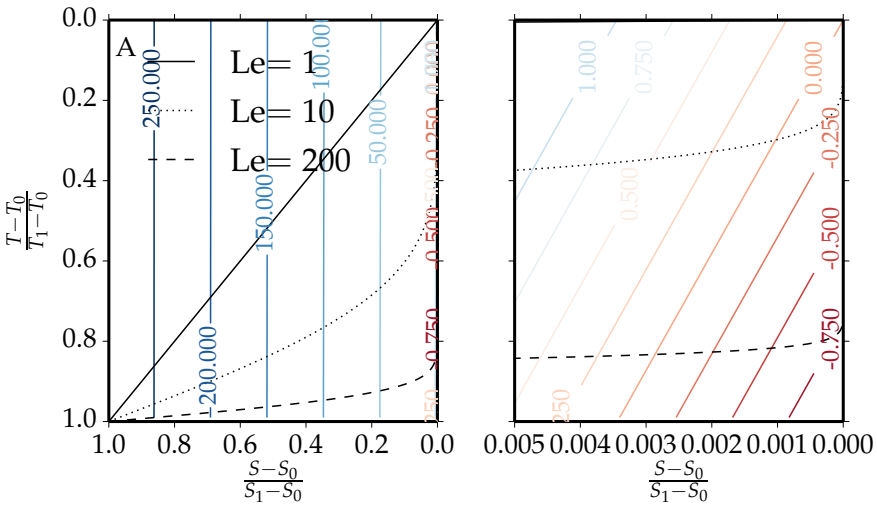

Figure A.4: Diffusive mean-buoyancy profiles (black) for varying ratio $\left(\frac{\kappa_T}{\kappa_S}\right)^{1/2} = \mathrm{Le}^{1/2}$ in a parametric plot. Coloured lines indicate iso-buoyancy levels. a) For increasing diffusivitiy difference, Le, the curvature of the mean-buoyancy profile increases. b) Zoom-in on the high-salinity region of (a). If the *Le* is large enough, the mean-buoyancy profile crosses the zero-buoyancy line (orange) and negative buoyancies occur (to the right of the orange line). This is the origin of the buoyancy reversal instability that drives the system and leads to mixing if the advection term is accounted for.

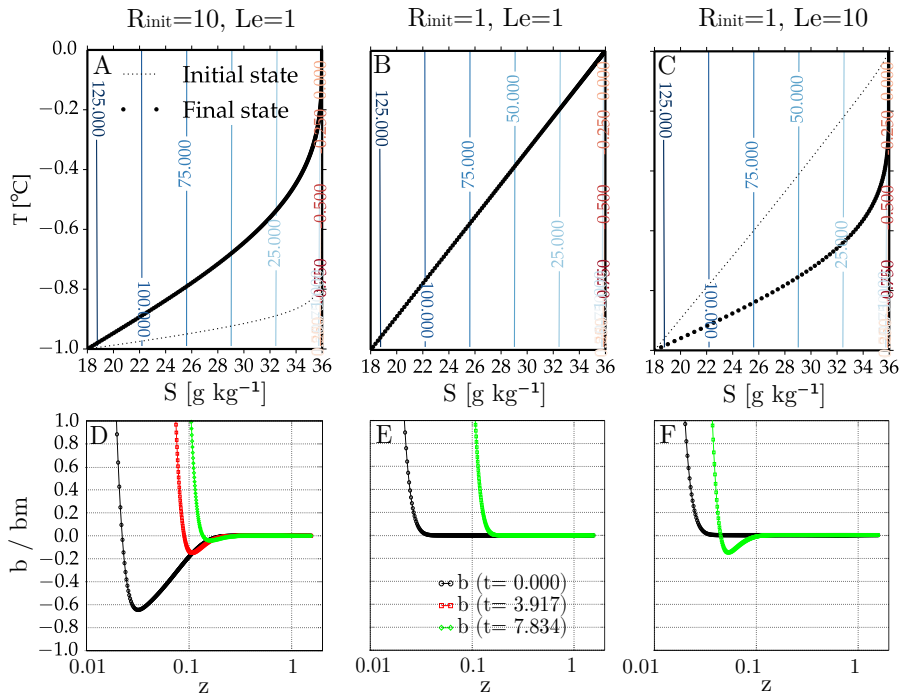

Figure A.5: Three two-dimensional simulation runs of varying initial gradient thickness and diffusivity of temperature and salinity illustrate the working principle of double diffusion. The runs are simulated with the parameterisation Eq. (A.6). They reproduce double diffusion as expected. The upper row illustrates the mean buoyancy of the simulations parametrically (analogous to Figure A.4). The lower row illustrates the mean buoyancy of the simulations spatially. Each column represents one of the following simulations after different evolution times: a,d) a run with same diffusivities, but different initial gradient thicknesses, b,e) a run with same diffusivities and same initial gradient thicknesses and c,f) a run with different diffusivities and same initial gradient thicknesses.

and salinity but also on the turbulent mixing. To illustrate this working principle, its dependence on the diffusivities and its reproduction by Eq. (2.14), I examplarily give three simulated mean-buoyancy profiles for varying initial gradient thickness and diffusivity of temperature and salinity:

Run (i) Same diffusivities, different initial gradient thicknesses

Run (ii) Same diffusivities, same initial gradient thicknesses

Run (iii) Different diffusivities, same initial gradient thicknesses

The buoyancy profile in run (i) shows a pronounced buoyancy reversal instability in the initial profile (t=0). The gradient thickness of the salinity profile is chosen ten times smaller than the gradient thickness of the temperature profile. Salinity increases quickly to its far-field value next to the interface. Temperature increases more slowly and reaches its far-field value further away from the interface. Next to the interface, buoyancy decreases with increasing salinity. Away from the interface, buoyancy increases with increasing temperature. Because temperature and salinity diffuse at the same rates in (i), their gradient thicknesses approximate each other. Salinity increasingly dominates the buoyancy across the whole domain and the buoyancy reversal instability vanishes (cf. Figure A.5a,e).

Run (ii) illustrates the limit of similar gradient thicknesses, the buoyancy profile does not feature a buoyancy reversal instability anymore (cf. Figure A.5b,d).

If temperature and salinity diffuse, however, at different rates like in run (iii) as opposed to run (i) and (ii), then a buoyancy reversal instability intrinsically creates even for similar initial gradient thicknesses (cf. Figure A.5c,f).

With these two-dimensional simulation a proof-of-concept has been achieved.

A.3 Initial Conditions

From the two-dimensional proof-of-concept study I have learned that system tends from an initial diffusive state to a final turbulent free-convection state. The initial state is set as

$$v\left(x, t=0\right) = 0, \tag{A.15}$$

$$T_{\mathrm{bg}}\left(x, t=0\right) = T_{\mathrm{ice}} + T_{\infty}\mathrm{erf}\left(-\frac{\sqrt{\pi}}{2}\frac{z}{\delta_i}\right), \tag{A.16}$$

$$S_{\mathrm{bg}}\left(x, t=0\right) = S_{\mathrm{ice}} + S_{\infty}\mathrm{erf}\left(-\frac{\sqrt{\pi}}{2}\frac{z}{\delta_i/10}\right), \tag{A.17}$$

where $\delta_i = 0.056\ L_0$ and L_0 is the system length scale. The final turbulent state is my objective.

I aim to speed up the initial transient of the system from the diffusive state to the final turbulent state. I use initial perturbations to the scalar profiles to provide the system already initially with driving buoyancy perturbations. The turbulent state of proof-of-concept study features temperature fluctuations on the order of 15% $(T_\infty - T_{\mathrm{ice}})$ and salinity fluctuations on the order of 8% $(S_\infty - S_{\mathrm{ice}})$. I supply a tenth part of theses fluctuations to all following systems as initial broadband perturbations T_{perturb} and S_{perturb}. The perturbations are chosen to have a gaussian power spectral density centered around a spatial frequency f_0 with a standart deviation of $f_0/6$. The temperature field is perturbed as

$$T\left(x, t=0\right) = T_{\mathrm{perturb}}\left(x_1, x_2\right)\left[1 - \mathrm{erf}\left(\frac{\sqrt{\pi}}{2}\frac{z}{\delta_{i,t}}\right)\right] + T_{\mathrm{bg}} \tag{A.18}$$

and the salinity field is perturbed as

$$S\left(x, t=0\right) = S_{\mathrm{perturb}}\left(x_1, x_2, z\right)\exp\left(-\left(\frac{z - z_{\mathrm{perturb}}}{2\delta_i}\right)^2\right) + S_{\mathrm{bg}}, \tag{A.19}$$

where $z_{\mathrm{perturb}}/L_0 = 0.006$, $\delta_{i,s} = 0.0025\ L_0$, $\max\left(S_{\mathrm{perturb}}\left(x_1, x_2, z\right)\right)/\left(S_\infty - S_{\mathrm{ice}}\right) = 0.008$ and $\delta_{i,t} = 0.056\ L_0$, $\max\left(T_{\mathrm{ice}}\left(x_1, x_2\right)\right)/\left(T_\infty - T_{\mathrm{ice}}\right) = 0.015$. $f_0 = 26.6$ corresponds to 7 d.

A.4 Boundary Conditions

A.4.1 In Nature

Unlike in the purely thermally driven system, here, molecular fluxes at the interface, the interfacial temperature and the interfacial salinity values adjust dynamically. Frank 1950 formulated the boundary conditions as

$$\left(T, S\right)\big|_{z_{\mathrm{ice}}} = \left(T_f\left(S_{\mathrm{ice}}\right), S_{\mathrm{ice}}\right) \tag{A.20a}$$

$$\frac{\partial T}{\partial z} = \frac{\mathrm{Lat}\rho_{\mathrm{ice}}}{k}\frac{\partial Z\left(t\right)}{\partial t} \tag{A.20b}$$

$$\frac{\partial S}{\partial z} = \frac{S_{\mathrm{ice}}}{\kappa_S}\frac{\partial Z\left(t\right)}{\partial t}. \tag{A.20c}$$

The first boundary condition Eq. (A.20a) forms the Dirichlet boundary condition of the temperature field at the interface just as in the fresh-ice–fresh-water system and is generally approximated as

$$T_{\mathrm{ice}}\left(x_1, x_2\right) + mS_{\mathrm{ice}}\left(x_1, x_2\right) = 0, \tag{A.21}$$

where $m = 0.05411$ °C g^{-1} kg (for sea water) and $m = 0.0598$ °C g^{-1} kg (for NaCl solutions) is a first order fitting parameter to the empirical relationship of

freezing-point temperature T_f and salinity (Notz, 2005). The interface value T_{ice} depends on the interface value S_{ice} of the salinity field.

Each the second and the third boundary condition Eq. (A.20b) and Eq. (A.20c) form a boundary condition on the velocity field. We found from the study of the purely fresh-ice–fresh-water system, that the flow velocity imposed by this boundary condition is negligable for the Richardson numbers under consideration. The boundary conditions on the velocity field must essentially be identical, because the interface can only ablate at one well-defined rate. Thus, Eq. (A.20b) and Eq. (A.20c) together form the Neumann boundary condition of the salinity field at the interface:

$$\kappa_S \left.\frac{\partial S}{\partial z}\right|_{z_{\mathrm{ice}}} = -\left(\frac{\rho_{\mathrm{ice}}}{\rho_{\mathrm{water}}}\frac{\mathrm{Lat}}{c_p T_{\mathrm{ice}}\left(S_{\mathrm{ice}}\right)}\frac{T_{\mathrm{ice}}\left(S_{\mathrm{ice}}\right)}{S_{\mathrm{ice}}}\right)^{-1} \kappa_T \left.\frac{\partial T}{\partial z}\right|_{z_{\mathrm{ice}}}. \tag{A.22}$$

Eq. (A.21) and Eq. (A.22) illustrate how the boundary conditions of temperature field and salinity field depend on the turbulent evolution of the flow. Certain prevailing interfacial values and gradients of temperature and salinity, $\tilde{T}_1$, $\tilde{S}_1$, $\partial_3\tilde{T}|_{z=0}$, and $\partial_3\tilde{S}|_{z=0}$, form the boundary conditions and determine the buoyancy structure of the flow close to the interface. The boundary conditions and the buoyancy profile force the velocity field of the flow. The temperature and salinity field evolves according to the velocity field and the boundary condition. The evolution of the flow in turn yields new interfacial gradients, $\partial_3\tilde{T}|_{z=0}$, and $\partial_3\tilde{S}|_{z=0}$. The interfacial gradients influence both the interfacial values, $\tilde{T}_1$, $\tilde{S}_1$, and the evolution of the flow.

A.4.2 In the Simulations

The interfacial temperature, T_{ice}, and interfacial salinity, S_{ice}, are subject to the evolution of the flow and to the boundary conditions (cf. Appendix A.4.1). In general, they are not constant, and neither is $b_{\mathrm{ice}} = b\left(S_{\mathrm{ice}}, T_{\mathrm{ice}}\right)$ constant.

Notwithstanding the boundary conditions encountered in nature, Eq. (A.21) and Eq. (A.22), I have apply Dirichlet boundary conditions at the top boundary of the scalar fields. The implementation of dynamical boundary conditions in the algorithm for the numerical simulations is not trivial and the following workaround is used instead:

I perform the simulations with Dirichlet boundary conditions at the top boundary of the scalar fields. It is therefore not readily evident that the simulation reflect a natural evolution of the fields. Once, turbulence is fully developed, the simulation certainly yields fixed interfacial scalar gradients. I make use of these fully developed interfacial scalar gradients to redefine $\{T_\infty, T_{\mathrm{ice}}, S_\infty, S_{\mathrm{ice}}\}$ a posteriori such that the boundary conditions Eq. (A.21) and Eq. (A.22) are met. Thus, the fields in the simulations do initially not evolve as they would in nature, but they do so once turbulence is fully developed.

Determination of Interfacial Temperature and Salinity

$\{T_\infty, S_\infty\}$ and the interfacial scalar gradients determine $\{T_{\text{ice}}, S_{\text{ice}}\}$ as follows. Following Gade (1993), I use the gradient thicknesses of salinity and temperature,

$$\delta_s = (S_\infty - S_{\text{ice}}) \,/\, \partial_3 S|_{z_{\text{ice}}} \text{, and } \delta_t = (T_\infty - T_{\text{ice}}) \,/\, \partial_3 T|_{z_{\text{ice}}} , \tag{A.23}$$

to derive an expression for the interfacial salinity S_{ice} from the boundary condition Eq. (A.22):

$$S_{\text{ice}} = -\frac{\rho_{\text{ice}}}{\rho_{\text{water}}} \frac{\text{Lat}}{c_p} \frac{\kappa_S}{\kappa_T} \, R \frac{(S_\infty - S_{\text{ice}})}{(T_\infty - T_{\text{ice}})}, \tag{A.24}$$

where

$$R = \delta_t / \delta_s \tag{A.25}$$

is the ratio of gradient thicknesses between temperature and salinity. Eq. (A.24) simplifies to

$$S_{\text{ice}} = \frac{f S_\infty}{T_\infty - T_f\,(S_{\text{ice}}) + f}, \tag{A.26}$$

with Eq. (A.21) and $f = -(\rho_{\text{ice}}/\rho_{\text{water}})(\text{Lat}/c_p)(\kappa_S/\kappa_T)R$. Eq. (A.26) converges independently of the initial choice of S_{ice}. S_{ice} only depends on T_∞, S_∞ and R. T_{ice} is then obtained from S_{ice} with Eq. (A.21).

The gradient-thickness ratio R of natural systems is unknown. Previous studies suggests $R \approx 2$ based on temperature and salinity profiles measured in a laboratory experiment (Martin and Kauffman, 1977). For identical gradient thicknesses, $R = 1$. For pure diffusion, Gade (1993) provides $R = 13.8 - 1.17\,(T_\infty - T_{\text{ice}})$ with the solutions given by Martin and Kauffman (1977).

A.5 Sensitivity of Interface Conditions to the Gradient-Thickness Ratio

If the flow is intermittent, gradient-thickness ratio in-between Gade (1993)'s parameterisation or pure diffusion and 2.25 will occur. Here, I utilise Eq. (A.26) to obtain a sense for the sensitivity of T_{ice}, b_m and Ri_0 on R.

The sensitivity of T_{ice}, b_m, and Ri_0 on T_∞ appears slightly stronger than on S_∞. T_{ice} and b_m change by order one for considerable changes in S_∞ from 26 g kg^{-1} to 38 g kg^{-1} but several times as strong for considerable changes in T_∞ from $(T_\infty - T_{\text{ice}}) = 0$ K to up to $(T_\infty - T_{\text{ice}}) = 5$ K. Ri_0 even changes by an order of magnitude for varying T_∞. For very high far-field temperatures, the sensitivity of Ri_0 on S_∞ is lost and it only depends on T_∞.

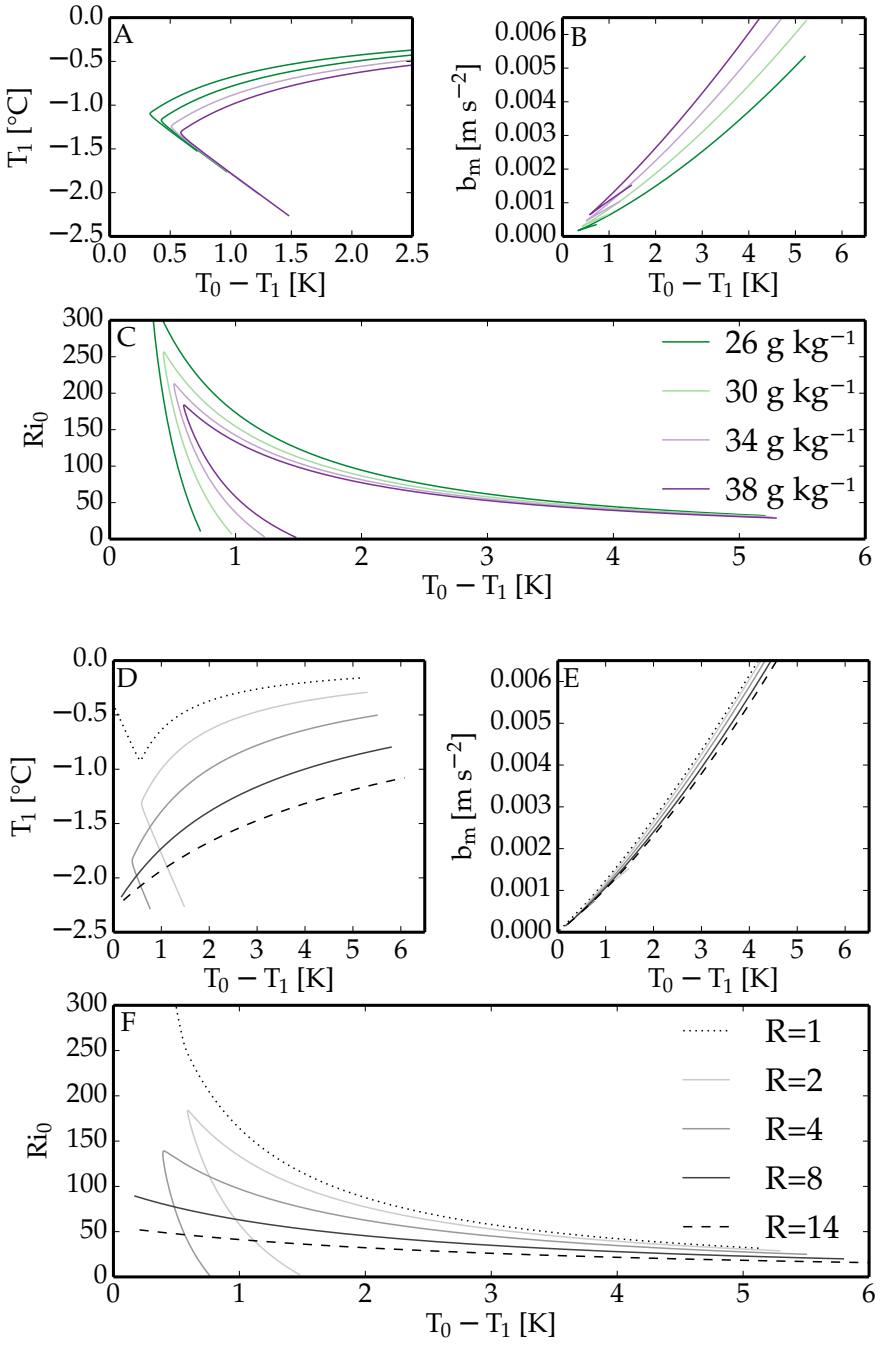

Figure A.6: a) Dependence of T_{ice} on far-field temperature T_∞ and on salinity S_∞ following Eq. (A.26) for $R = 2$. b) $b_m = b(S = S_\infty, T = T_{\text{ice}})$ as calculated from the values of (a), Eq. (9) in Martin and Kauffman (1977), Eq. (2.1) and Eq. (4.18). c) $\text{Ri}_0 = 1 - \frac{b_{\text{ice}}}{b_m}$ as calculated from the values of (a), Eq. (9) in Martin and Kauffman (1977), Eq. (2.1) and Eq. (4.18). d) Dependence of T_{ice} on the gradient-thickness ratio R following Eq. (A.26) for $S_\infty = 38$ g kg^{-1}. e) $b_m = b(S = S_\infty, T = T_{\text{ice}})$ as calculated from the values of (b), Eq. (9) in Martin and Kauffman (1977), Eq. (2.1) and Eq. (4.18). f) $\text{Ri}_0 = 1 - \frac{b_{\text{ice}}}{b_m}$ as calculated from the values of (b), Eq. (9) in Martin and Kauffman (1977), Eq. (2.1) and Eq. (4.18).

The sensitivity of T_{ice}, b_m, and Ri_0 on R appears slightly stronger than on S_∞. T_{ice} and b_m change by order one for considerable changes in S_∞ from 26 g kg^{-1} to 38 g kg^{-1} but several times as strong for considerable changes in T_∞ from $(T_\infty - T_{\mathrm{ice}}) = 0$ K to up to $(T_\infty - T_{\mathrm{ice}}) = 5$ K. Ri_0 even changes by an order of magnitude for varying T_∞.

For $R = 2$ as estimated from the laboratory experiment of Martin and Kauffman (1977), one finds that the interfacial temperature varies between about -1.3℃ and about -0.2℃ for different far-field temperatures and salinities. For T_∞ just slightly above T_{ice}, T_{ice} increases rapidly with increasing T_∞ (not shown). This behaviour yields the lower branch in Figure A.6a of increasing T_{ice} with decreasing $T_\infty - T_{\mathrm{ice}}$. The upper branch for T_∞ well above T_{ice} and T_{ice} increases with increasing $T_\infty - T_{\mathrm{ice}}$.

The absolut magnitude of the minimum buoyancy b_m varies by order one with S_∞.

A.6 Sensitivity of the Buoyancy-Reversal Strength on the Initial Conditions

The simulations of the fresh-ice–fresh-water interface serve as a starting point for the setup of the ice–ocean interface. I choose error functions as mean vertical profiles in temperature (cf. Figure 5.3, red dashed) and salinity (purple dashed). Run (iii) indicates that considerable computational time is expended when diffusion alone developes the buoyancy reversal instability (BRI) from identical gradient thicknesses in temperature and salinity. The ratio of gradient thicknesses is R. $R\,(t = 0) = R_{\mathrm{initial}}$ sets the initial BRI strength $b_{\mathrm{min}}/b_m|_{\mathrm{t=0}}$. Its choice is a risky business. On the one hand the system should quickly reach a fully developed state in which the initial conditions are forgotten. On the other hand the system should not be provided with potential energy substanially higher than the in-flow that it would develop out of itself. The choice of R_{initial} is further complicated by the dependence of the initial BRI strength on the Ri_0 of the simulation (cf. Figure A.7), and the dependence of the potential-energy flow to the system on the Le.

I choose an initial value of $R = R_{\mathrm{initial}} = 4$. This is close to previously reported values of $R \approx 2.3$ (Gade, 1993) and features a sufficiently strong initial BRI of about 0.4 ± 0.1 (cf. Figure A.7) to trigger convection early within the simulation (cf. Figure A.8). It will be shown later that the choice of R_{initial} influences the evolution of relevant flow properties significantly. The relevant simulation outcome, R and e, remain however uneffected (cf. Figure A.8), and $R_{\mathrm{initial}} = 4$ seems to yield quickly developed and stable results.

Spatial perturbations to the initial BRI $b_{\mathrm{min}}/b_m|_{\mathrm{t=0}}$ grow in time and lead up to mixing and free convection. The perturbations are chosen similar to the setup

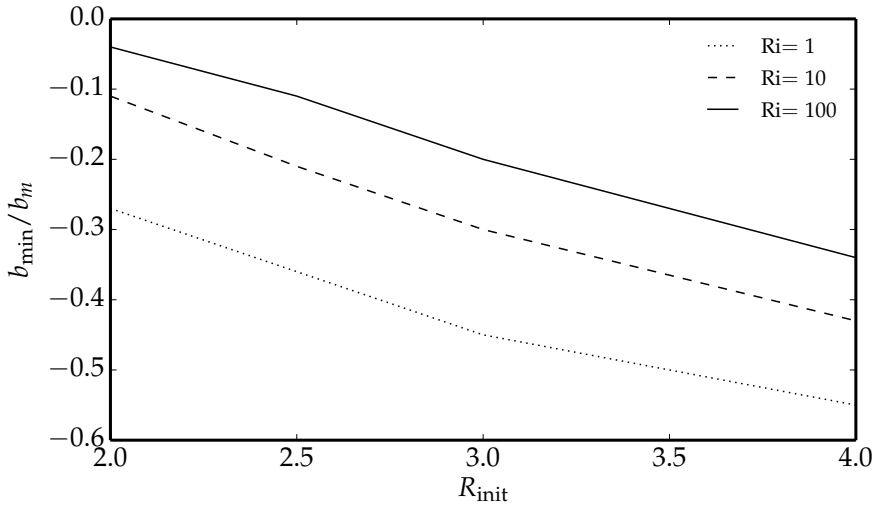

Figure A.7: Variation of the initial buoyancy reversal strength $b_{\min}/b_m|_{\text{t=0}}$ with Ri_0 and R_{initial}.

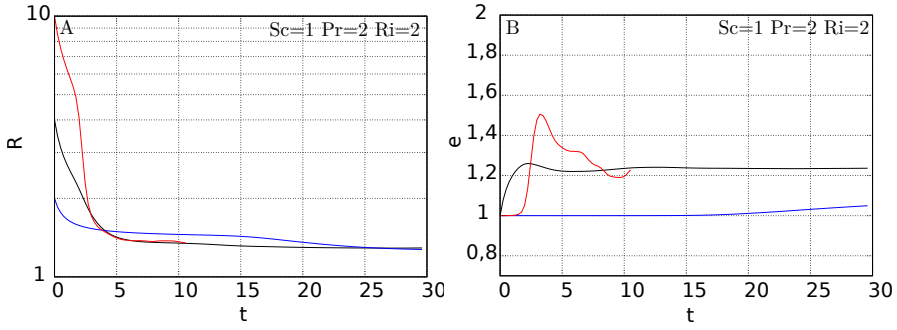

Figure A.8: a) The simulation outcome R at a final non-dimensionalised simulation time $t = 30$ is similar for simulations of different R_{initial}. The transition to the final value takes a substantial fraction of the whole simulation time for too low a value of R_{initial} (here for $R_{\text{initial}} = 2$). Simulations of higher R_{initial} reach a stable state more quickly. b) The simulation outcome e at a final non-dimensionalised simulation time $t = 30$ seems similar for simulations of different R_{initial}. The transition to the final value is not achieved for simulations of too low a value of R_{initial} (here for $R_{\text{initial}} = 2$). Simulations of too high R_{initial} seem to oscillate around a final value that is not reached.

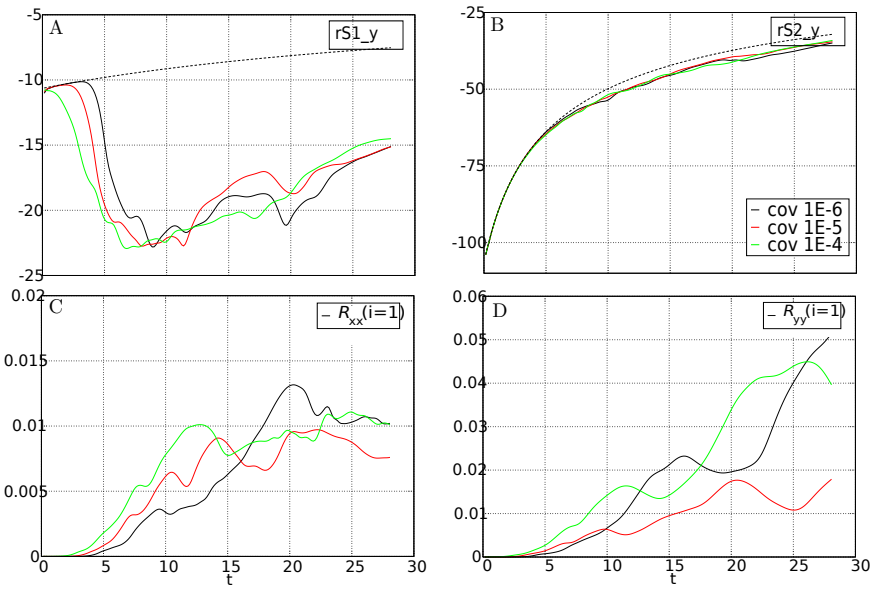

Figure A.9: Non-dimensionalised temperature gradient (a), salinity gradient (b), integrated horizontal velocity fluctuations (c) and vertical velocity fluctuations (d) over non-dimensionalised simulation time for simulations of different initial temperature fluctuations: half as strong as later on used in simulations (black), twice as strong (red), five times as strong (green). Final temperature gradients, salinity gradients and velocity fluctuations that are identical within the degree of statistical convergence of the two-dimensional sensitivity test study.

of the fresh-ice–fresh-water interface. I perform three simulation of initial temperature fluctuations that are (i) half as strong, (ii) twice as strong and (iii) five times as strong to test the sensitivity of the simulation on the initial perturbations (cf. Figure A.9). Final temperature gradients, salinity gradients and velocity fluctuations that are identical within the degree of statistical convergence of the two-dimensional sensitivity test study. Final temperature fluctuations are of the order of 15% $(T_\infty - T_{\mathrm{ice}})$.

Appendix B

Experimental Considerations

In this appendix, the heat flux through the walls of the tank in the laboratory experiment is assessed. Further, the double page 114–115 provides the ensemble data of the laboratory realisation and the numerical realisation of the turbulent-mixing experiment at $T_\infty \approx 5$ °C. Finally, an assessment of the experiment by Martin and Kauffman (1977) is given.

B.1 Heat Flux Through Walls

Eq. (3.5) assumes that no energy flows through water-body boundaries except through the ice–water interface but the system is not perfectly closed. Even though it is isolated and located in a cooling chamber, energy still enters and leaves the system through its boundaries. In the following, I assess how ΔE_{int} is influenced by the energy fluxes through the boundaries, first the latent-heat flux by melt water dripping from the ice walls, second the sensible-heat flux through the tank walls.

Latent-Heat Flux

Melt water is created by two processes: the energy exchange at the ice–water interface and the energy exchange at the ice–air interface.

The energy exchange at the ice–air interface, $E_{\text{mw,air}}$, compares to the energy exchange at the ice–water interface, $E_{\text{mw,water}}$, as

$$\frac{E_{\text{mw,air}}}{E_{\text{mw,water}}} = \frac{-\lambda_{\text{air}}\, \nabla T|_{\text{wall}}\, \mathbf{e}_3 \left(1 + 4\frac{0.1\times 0.35}{0.35\times 0.35}\right)}{-\lambda_{\text{water}} \mathbf{e}_3\, \nabla T|_{\text{wall}}}. \tag{B.1}$$

The geometrical factor $\left(1 + 4\frac{0.1\times 0.35}{0.35\times 0.35}\right)$ represents one main and four lateral ice walls of an area of 0.1 m×0.35 m that are in contact with air compared to the the

ice–water interface of an area of 0.35 m×0.35 m. Eq. (B.1) can be simplified as follows because the initial and final temperatures of the melt waters are identical,

$$\frac{E_{\mathrm{mw,air}}}{E_{\mathrm{mw,water}}} = 0.10 \frac{z_{0,\mathrm{water}}}{z_{0,\mathrm{air}}}, \tag{B.2}$$

where z_0 is the characteristic distance over which the temperature change $\nabla T \mathbf{e}_3 z_0$ occurs. If both energy exchanges were diffusive, $0.10\ z_{0,\mathrm{water}}/z_{0,\mathrm{air}} = 0.10\ (\mathrm{Pr}_{\mathrm{water}}/\mathrm{Pr}_{\mathrm{air}})^{1/2} = 0.32$. The energy exchange at the ice–air interface is laminar most of the time, because the cooling chamber is only in operating mode for a short term every 30 minutes. The energy exchange at the ice–water interface, however, is turbulent, and $\frac{E_{\mathrm{mw,air}}}{E_{\mathrm{mw,water}}} \leq 0.32$.

The internal-energy change of the melt water compares to the heat of fusion as

$$\frac{E_{\mathrm{mw,water}}}{E_{\mathrm{lat}}} = \frac{\rho_{\mathrm{ice}} h_m c_v \left(T_{\mathrm{end}} - T_{\mathrm{ice}}\right)}{\rho_{\mathrm{ice}} h_m L}. \tag{B.3}$$

$E_{\mathrm{mw,water}}/E_{\mathrm{lat}} \leq 0.08$ for all laboratory experiments except the one at $T_\infty = 15.9$ ℃, where it is ≤ 0.20. I therefore conclude to neglect melt water dripping from the ice–air interface to the water body, and to retain melt water from the ice–water interface in the analysis.

Sensible-Heat Flux

The energy flux through the tank walls distorts ΔE_{int} as a measure for the energy exchange at the fresh-ice–fresh-water interface. The temperature difference between the water body and the cooling chamber drive this energy flux. In principle, I minimise the temperature difference, but the chamber's ability to keep the temperature is limited to about ±3 ℃. The chamber is mostly in a stand-by mode while it is slowly heating from temperatures beneath its set temperature to temperatures above its set temperature. The temperature difference between cooling chamber and water body, hence, varies from realisations to realisation. Further, the temperature profile in the cooling chamber stratifies while it is in stand-by mode and one finds a vertical temperature gradient in air next to the tank wall (cf. Figure B.1). I therefore obtain the mean energy flux through the tank walls from the temporal evolution of the bulk temperatures of all laboratory realisations (cf. Figure B.2).

In the beginning of the laboratory realisation at $T_\infty = 5$ ℃, before the ice is in contact with the water but after the water temperature has been homogenised to T_∞, the mean-temperature flux out of the water body is

$$-\left(0.3 \pm 2.0\right) \times 10^{-4} \frac{\mathrm{K}}{\mathrm{s}} \tag{B.4}$$

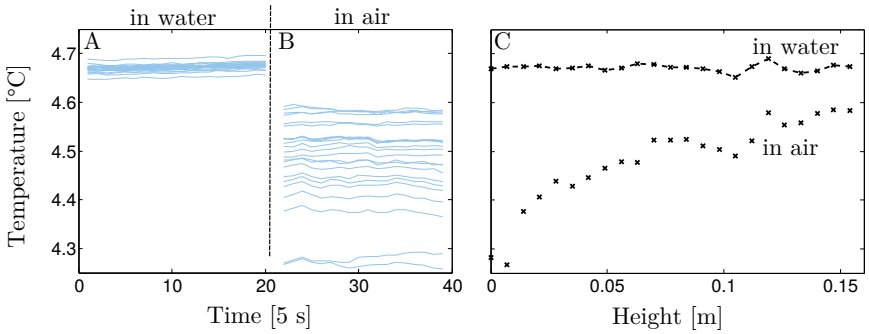

Figure B.1: a) Temporal evolution of individual thermistor measurements in a water body at homogeneous far-field temperature. b) Temporal evolution of individual thermistor measurements in air next to the water body. c) Temporal mean of the temperature evolution shown in (a) and (b).

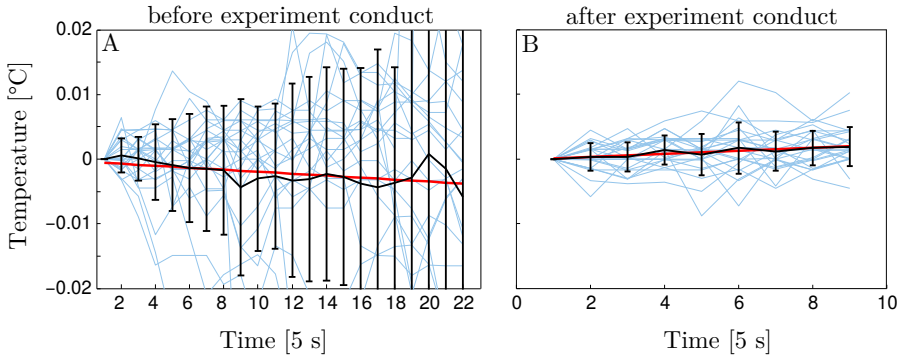

Figure B.2: Mean energy flux through the tank walls from the evolution of the mean temperatures of all laboratory realisations. a) Before the laboratory realisation but after the water temperature has been homogenised to T_∞, the mean-temperature flux out of the water body is $-(0.3 \pm 2.0) \times 10^{-4} \frac{\mathrm{K}}{\mathrm{s}}$. b) After the laboratory realisation but while the water is mixed with a pump, the mean-temperature flux out of the water body is $+(1.6 \pm 9.9) \times 10^{-5} \frac{\mathrm{K}}{\mathrm{s}}$.

(cf. Figure B.2a). At the end of a laboratory realisation, while the water is mixed with a pump, the mean-temperature flux to the tank is

$$+\,(1.6 \pm 9.9) \times 10^{-5} \frac{\mathrm{K}}{\mathrm{s}} \tag{B.5}$$

(cf. Figure B.2b). These temperature fluxes reveal that the average temperature in the cooling chamber at the height of the tank is in-between T_∞ and T_{end}. The spread of 2.0×10^{-4} K/s is larger than the average temperature flux of 0.3×10^{-4} K/s itself.

From the spread of 2.0×10^{-4} K/s and $(T_{\mathrm{end}} - T_\infty) \approx 0.25$ K follows that ΔE_{int} could statistically deviate by up to 80 % over the course of a 20-minute laboratory realisation. Effectively the observed statistical spread for a given run time is less than 10 % for all bulk measurements except for $T_\infty = 15.9$ °C, where it is between 5 % and 22 % (cf. Figure 3.7).

From the average temperature flux of 0.3×10^{-4} K/s follows that a systematic deviation can be excluded to an accuracy of 12 % of ΔE_{int}.

B.2 Turbulent Laboratory Experiment for $T_\infty = 5.0$ ℃

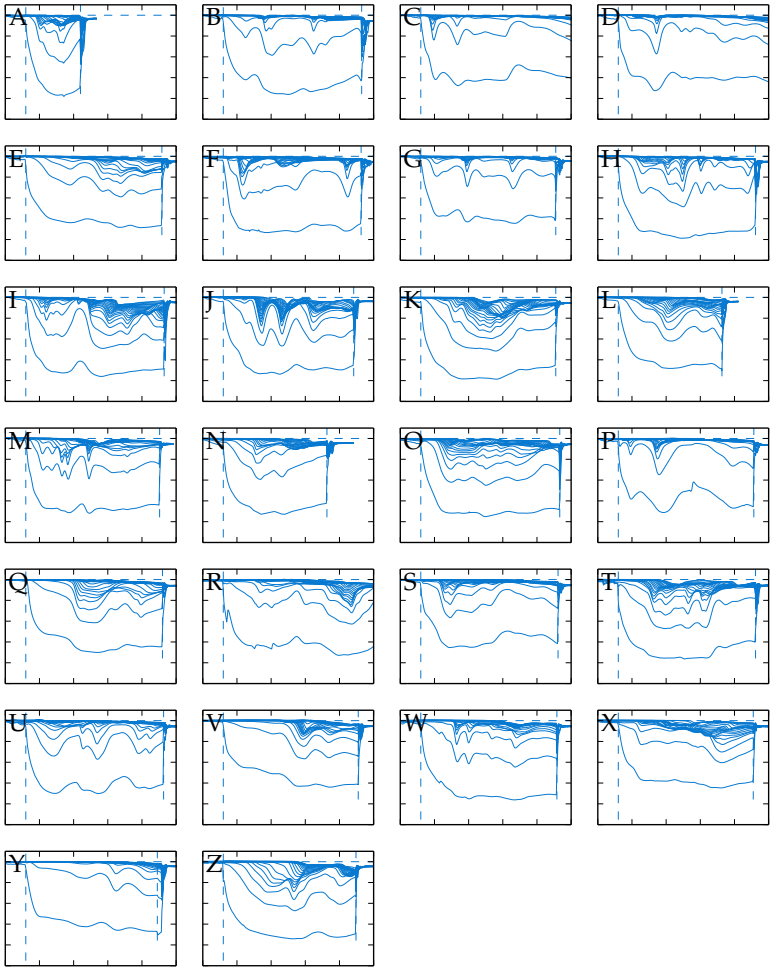

Figure B.3: Thermistor measurements of all individual laboratory realisations of the ensemble of $T_\infty = 5.0$ ℃. Y axis: Temperature from 0 ℃ to 5.5 ℃; ticks mark one-degree-celsius steps. X axis: Time; ticks mark 5 minute steps. The first vertical line marks the time of ice–water contact, the second line the starting time of external mixing with a pump.

B.3 Numerical Simulation of the Turbulent Laboratory Experiment

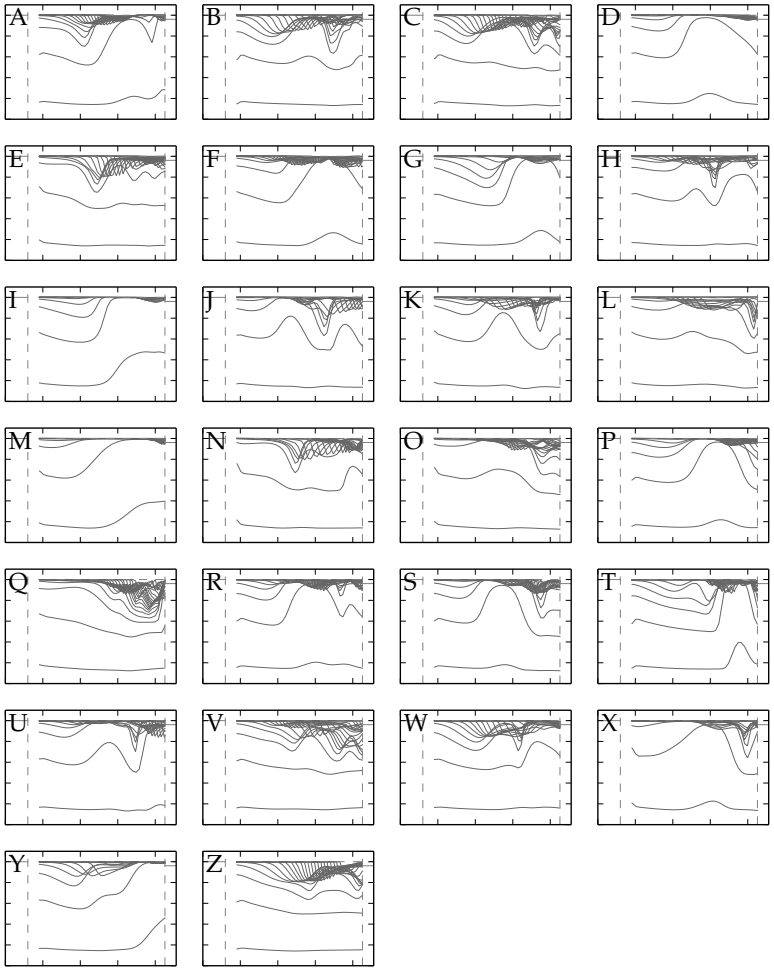

Figure B.4: Temperature measurement of randomly selected towers of a numerical simulation of $T_\infty = 4.975$ ℃. Y axis: Temperature from 0 ℃ to 5.5 ℃; ticks mark one-degree-celsius steps. X axis: Time; ticks mark 5 minute steps. The first vertical line marks the time of ice–water contact, the second line the starting time of external mixing with a pump.

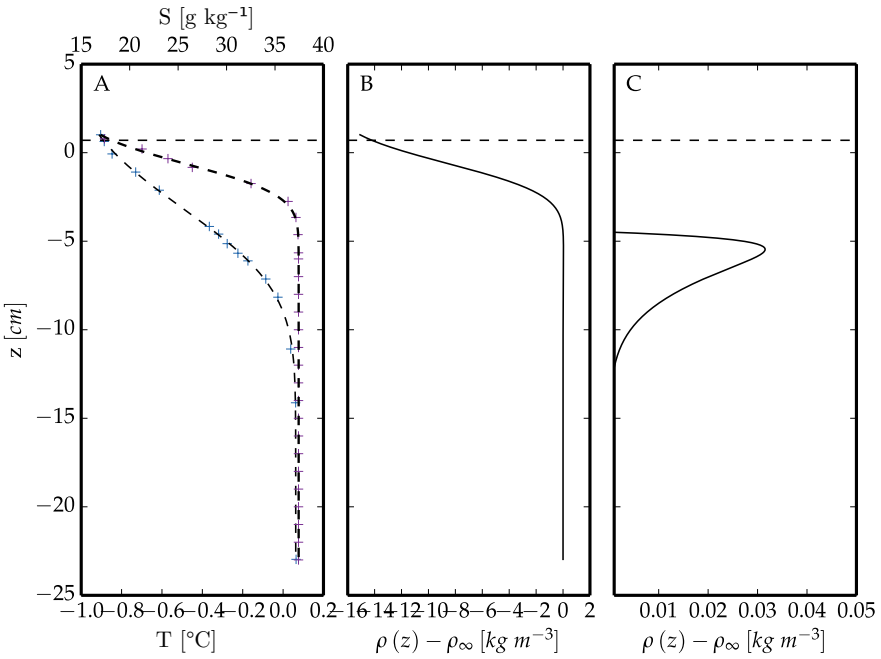

Figure B.5: a) Temperature (blue) and salinity (purple) profiles observed by Martin and Kauffman (1977) in their laboratory tank experiment after 46.5h. b,c) Buoyancy profile derived from the temperature and salinity profiles in (a).

B.4 The Martin–Kauffman Case

The study of Martin and Kauffman (1977) provides an insightful reference. They conduct a laboratory experiment of floating fresh ice on a 37.6 ‰NaCl solution. From the temperature and salinity profiles, they provide (cf. Figure B.5a), one can obtain the buoyancy profile (cf. Figure B.5b,c). It suggests values $b_{\text{ice}} = 1.384\ 10^{-1}\text{m s}^{-2}$, $b_m = 1.083\ 10^{-3}\text{m s}^{-2}$ and $b_{min} = 2.83\ 10^{-1}\ b_m$ from which we then obtain $Ri_0 = 129$ and $Ri_* = 450$. The Ri_0 number determined from their laboratory experiment agrees almost to order one with the estimate from our diffusive assessment of $Ri_0 \approx 300$ for $T_\infty = 0$ ℃and $S_\infty = 38$ g kg^{-1} (cf. Figure A.6).

Martin and Kauffman (1977) provide the relationship of boundary conditions T_{ice}, S_∞ and $T_s + mS_\infty$ from their one-dimensional theoretical model, where T_s is the temperature at a height $\delta_s = 2 \times 2.8 \times (\kappa_S\ t)^{1/2}$ beneath the ice and $m = 5.71 \times 10^{-2}$ ℃. I use their results (copied in Figure B.6a) to obtain the minimum buoyancy values b_m (cf. Figure B.6b) and Richardson numbers Ri_0 (cf. Figure B.6b). To give b_m and Ri_0 as a function of the temperature difference $T_\infty - T_{\text{ice}}$, I rewrite their dependent variable $H' = T_s + mS_\infty$. I further assume

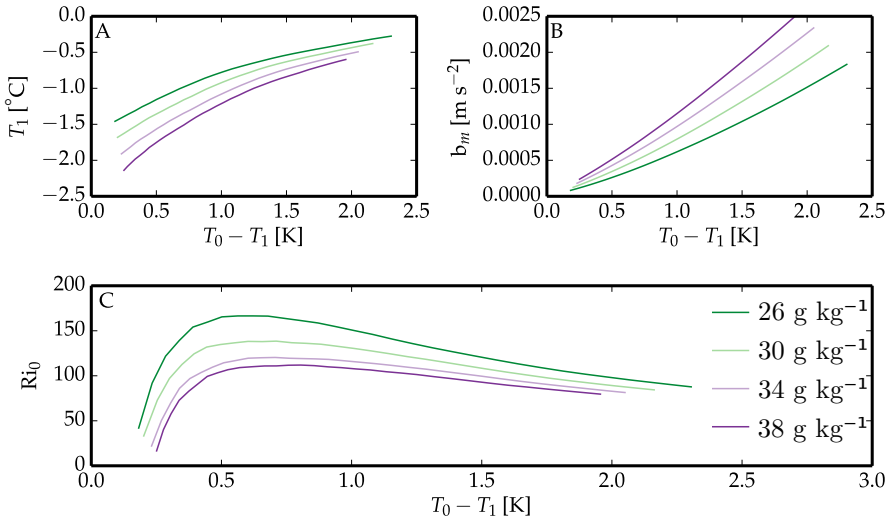

Figure B.6: a) Copy of relationship between interfacial temperature T_{ice} and far-field temperature T_∞ and salinity S_∞ (originally given as Fig. 9. in Martin and Kauffman (1977)). b) $b_m = b(S = S_\infty, T = T_{\text{ice}})$ as calculated from the values of (a), Eq. (9) in Martin and Kauffman (1977), Eq. (2.1) and Eq. (4.18). c) $\text{Ri}_0 = 1 - \frac{b_{\text{ice}}}{b_m}$ as calculated from the values of (a), Eq. (9) in Martin and Kauffman (1977), Eq. (2.1) and Eq. (4.18).

that the temperature T_s, defined as the temperature at the lower end of the diffusive layer next to the wall, is approximately $T_{\text{ice}} + 0.9\,(T_\infty - T_{\text{ice}})$.

$$H' = T_s + mS_\infty \approx T_{\text{ice}} + 0.9\,(T_\infty - T_{\text{ice}}) - T_f\,(S_\infty) \tag{B.6}$$

$$T_\infty - T_{\text{ice}} \approx \frac{1}{0.9}\left(H' - (T_{\text{ice}} - T_f\,(S_\infty))\right). \tag{B.7}$$

Depending on the temperature difference $T_\infty - T_{\text{ice}}$ and the far-field salinity S_∞, their results yield Richardson numbers between 17 and 170.

One can further use the buoyancy profiles obtained from the laboratory experiment of Martin and Kauffman (1977) as indication to how the system is represented in the (S,T)-diagram (cf. Figure B.7). In agreement with the (σ,θ)-profiles found from diffusive salinity and temperature profiles (cf. Figure A.4), the (σ,θ)-profiles of Martin and Kauffman (1977) als0 bend towards (0,1). In particular, the curvature of the (σ,θ)-profile in the parameter space is far more pronounced than the curvature of the iso-buoyancy lines (coloured lines). The comparison of the two shows that difference of diffusivities has a substanially stronger influence on the (S,T)-profile than does the difference between parabolic and bilinear buoyancy profile. I conclude that the bilinear buoyancy function Eq. (A.6) is sufficiently precise for the simulation setup, given the constraints in Le number and boundary conditions.

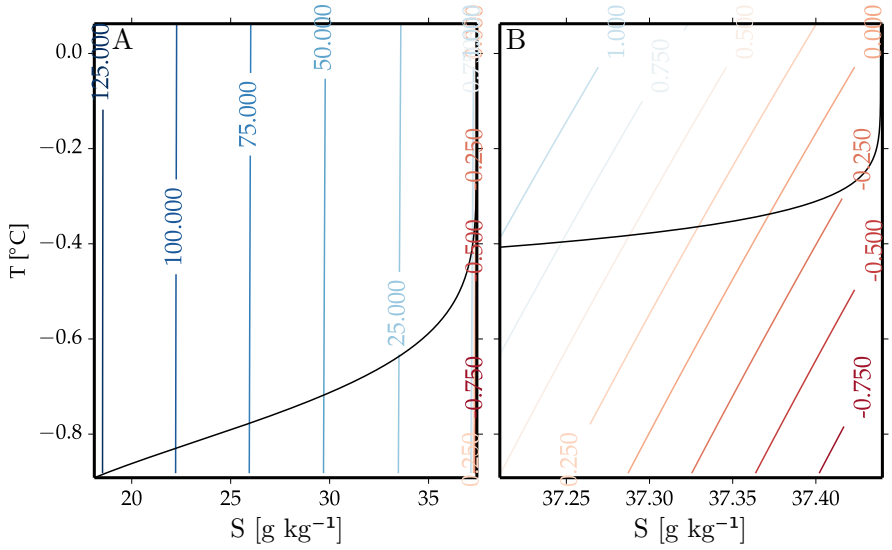

Figure B.7: a) Parametric plot of iso-buoyancy contours for the laboratory study conducted by Martin and Kauffman (1977) as calculated from their temperature and salinity profiles Figure B.6a, Eq. (9) in (Martin and Kauffman, 1977, 279), Eq. (2.1) and Eq. (4.18). b) Zoom-in on the high-salinity region of (a)

An evaluation of the temperature profile of Martin and Kauffman (1977) (cf. Figure B.6a), yields a melt rate in their laboratory experiment of about (0.82 ± 0.17) mm d^{-1}. If the melt rate expression obtained in this work, Eq. (5.24), is used in combination with the density of NaCl (as used in their experiment), melt rates by a factor of three lower than those observed in their experiment are obtained (cf. Figure B.8). Two main consideration may explain the discrepancy. First, the determination of the unstable fraction yields a considerable uncertainty for the Richardson number equivalent to the laboratory experiment by Martin and Kauffman (1977). The comparison would thus indicate that the unstable fraction is actually larger than given in Eq. (5.7). Second, the bound laboratory configuration that they use and run till equilibrium may also have influenced their result. Further free-convection experiments of lower Richardson number along with an stability analysis to properly determine the unstable fraction would provide insight.

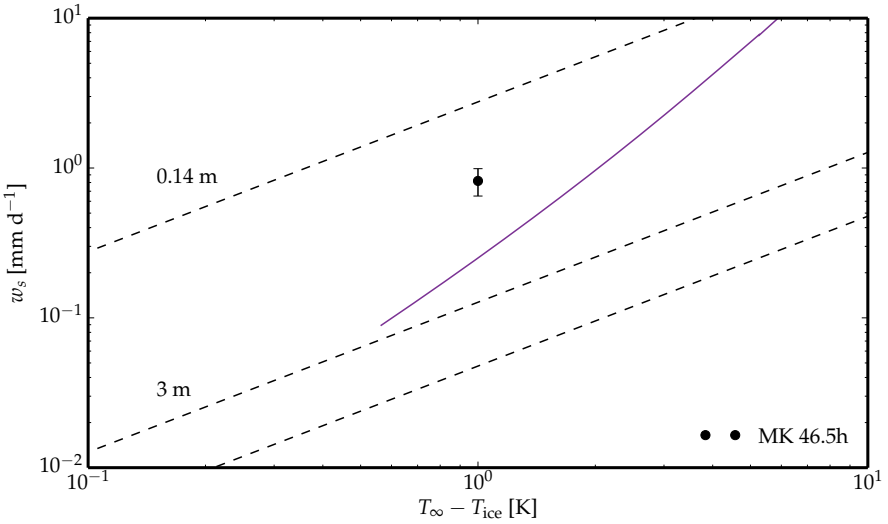

Figure B.8: Melt rate as derived from Eq. (5.24) for ice in a 38 g kg^{-1} NaCl solution as a function of $(T_\infty - T_{\mathrm{ice}})$. Diffusive melt rates for boundary layers of thicknesses 0.14 m, 3 m and 8 m provide a reference (dashed lines). The black dot is the melt rate derived from the temperature profile of the experiment of Martin and Kauffman (1977) at time 46.5h.

Bibliography

Boger, D. V., **Westwater, J. W.** (1967): Effect of Buoyancy on the Melting and Freezing Process. *J. Heat Transfer*, **89(1)**:pp. 81–89, doi:10.1115/1.3614327

Carpenter, J. R., **Sommer, T.**, **Wüest, A.** (2012): Simulations of a double-diffusive interface in the diffusive convection regime. *J. Fluid Mech.*, **1(1)**:pp. 1–26

Carpenter, J. R., **Timmermans, M.-L.** (2013): Does Rotation Influence Double-Diffusive Fluxes in Polar Oceans? *J. Phys. Oceanogr.*, **44(1)**:pp. 289–296, doi:10.1175/JPO-D-13-098.1

Chillá, F., **Schumacher, J.** (2012): New perspectives in turbulent Rayleigh-Bnard convection. *Eur. Phys. J. A.*, **35(7)**, doi:10.1140/epje/i2012-12058-1

Deardorff, J. W. (1970): Convective Velocity and Temperature Scales for the Unstable Planetary Boundary Layer and for Rayleigh Convection. *J. Atmos. Sci.*, **27(8)**:pp. 1211–1213, doi:10.1175/1520-0469(1970)027⟨1211:CVATSF⟩2.0.CO;2

Fedorovich, E., **Rotunno, R.**, **Stevens, B.** (Eds.) *Atmospheric Turbulence and Mesoscale Meteorology: Scientific Research Inspired by Doug Lilly* (Cambridge University Press, Cambridge, 2004)

Frank, F. C. (1950): Radially Symmetric Phase Growth Controlled by Diffusion. *Proc. R. Soc. A*, **201(1067)**:pp. 586–599, doi:10.1098/rspa.1950.0080

Frankenstein, G., **Garner, R.** (1967): Equations for determining the brine volume of sea ice from -0.5C to -22.9C. *J. Glaciol.*, **6**:pp. 943–944

Gade, H. G. (1979): Melting of Ice in Sea Water: A Primitive Model with Application to the Antarctic Ice Shelf and Icebergs. *J. Phys. Oceanogr.*, **9(1)**:pp. 189–198, doi:10.1175/1520-0485(1979)009⟨0189:MOIISW⟩2.0.CO;2

—— (1993): When ice melts in sea water: A review. *Atmos.-Ocean*, **31(1)**:pp. 139–165, doi:10.1080/07055900.1993.9649466

Gebhart, B., **Sammakia, B.**, **Audunson, T.** (1983): Melting characteristics of horizontal ice surfaces in cold saline water. *J. Geophys. Res.*, **88(C5)**:pp. 2935–2942, doi:10.1029/JC088iC05p02935

Josberger, E. G. (1983): Sea ice melting in the marginal ice zone. *J. Geophys. Res.*, **88(C5)**:pp. 2841–2844, doi:10.1029/JC088iC05p02841

Keitzl, T., **Notz, D.**, **Mellado, J.-P.** Video: How fast does ice melt from below? (American Physical Society, 2014), doi:10.1103/APS.DFD.2014.GFM.V0020

Kraichnan, R. H., **Montgomery, D.** (1980): Two-dimensional turbulence. *Rep. Prog. Phys.*, **43(5)**:pp. 547–619

Lele, S. K. (1992): Compact finite difference schemes with spectral-like resolution. *J. Comput. Phys.*, **103(1)**:pp. 16–42, doi:10.1016/0021-9991(92)90324-R

Martin, S., **Kauffman, P.** (1977): An Experimental and Theoretical Study of the Turbulent and Laminar Convection Generated under a Horizontal Ice Sheet Floating on Warm Salty Water. *J. Phys. Oceanogr.*, **7(2)**:pp. 272–283, doi:10.1175/1520-0485(1977)007⟨0272:AEATSO⟩2.0.CO;2

McPhee, M. G. *Air-Ice-Ocean Interaction: Turbulent Ocean Boundary Layer Exchange Processes* (Springer, 2008)

Mellado, J., **Ansorge, C.** (2012): Factorization of the Fourier transform of the pressure-Poisson equation using finite differences in colocated grids. *Z. angew. Math. Mech.*, **92(5)**:pp. 380–392, doi:10.1002/zamm.201100078

Mellado, J. P. (2010): The evaporatively driven cloud-top mixing layer. *J. Fluid Mech.*, **660**:pp. 5–36, doi:10.1017/S0022112010002831

—— (2012): Direct numerical simulation of free convection over a heated plate. *J. Fluid Mech.*, **712**:pp. 418–450, doi:10.1017/jfm.2012.428

Mellado, J. P., **Stevens, B.**, **Schmidt, H.**, *et al.* (2010): Two-fluid formulation of the cloud-top mixing layer for direct numerical simulation. *Theor. Comp. Fluid. Dyn.*, **24(6)**:pp. 511–536, doi:10.1007/s00162-010-0182-x

Notz, D. (2005): *Thermodynamic and Fluid-Dynamical Processes in Sea Ice.* Ph.D. thesis, University of Cambridge

Notz, D., **McPhee, M. G.**, **Worster, M. G.**, *et al.* (2003): Impact of underwater-ice evolution on Arctic summer sea ice. *J. Geophys. Res.*, **108**:p. 12 PP., doi:200310.1029/2001JC001173

Pope, S. B. *Turbulent Flows* (Cambridge University Press, 2000)

Pounder, E. R. *The Physics of Ice* (Pergamon Press, Oxford, UK, 1965)

Sharqawy, M. H., **Lienhard, J. H.**, **Zubair, S. M.** (2010): Thermophysical properties of seawater: a review of existing correlations and data. *Desalination*, **16(1-3)**:pp. 354–380, doi:10.5004/dwt.2010.1079

Siems, S. T., **Bretherton, C. S.**, **Baker, M. B.**, *et al.* (1990): Buoyancy reversal and cloud-top entrainment instability. **116**:pp. 705–739, doi:10.1002/qj.49711649309

Sirevaag, A. (2009): Turbulent exchange coefficients for the ice/ocean interface in case of rapid melting. *Geophys. Res. Lett.*, **36(4)**:p. L04606, doi:10.1029/2008GL036587

Steele, M., **Mellor, G. L.**, **Mcphee, M. G.** (1989): Role of the Molecular Sublayer in the Melting or Freezing of Sea Ice. *J. Phys. Oceanogr.*, **19(1)**:pp. 139–147, doi:10.1175/1520-0485(1989)019⟨0139:ROTMSI⟩2.0.CO;2

Stern, M. E. (1960): The Salt-Fountain and Thermohaline Convection. *Tellus*, **12(2)**:pp. 172–175, doi:10.1111/j.2153-3490.1960.tb01295.x

Stull, R. B. *An introduction to boundary layer meteorology* (Kluwer Academic Publishers, Dordrecht; Boston, 1988)

Tabeling, P. (2002): Two-dimensional turbulence: a physicist approach. *Physics Reports*, **362(1)**:pp. 1–62, doi:10.1016/S0370-1573(01)00064-3

Turner, J. S. *Buoyancy effects in fluids*. Cambridge monographs on mechanics and applied mathematics (Univ. Press, London [u.a.], 1973)

—— (1974): Double-Diffusive Phenomena. *Annu. Rev. Fluid Mech.*, **6(1)**:pp. 37–54, doi:10.1146/annurev.fl.06.010174.000345

Williamson, J. H. (1980): Low-storage Runge-Kutta schemes. *J. Comput. Phys.*, **35(1)**:pp. 48–56, doi:10.1016/0021-9991(80)90033-9

Wilson, N., **Sarma, T.**, **Pritchard, R.** Prediction of Heat, Mass, and Momentum Transfer during Laminar Forced Convective Melting of Ice in Saline Water. In: *Sea ice processes and models: proceedings of the Arctic Ice Dynamics Joint Experiment International Commission of Snow and Ice symposium*, (p. 339) (University of Washington Press, 1980)

Winters, K. B., **Lombard, P. N.**, **Riley, J. J.**, *et al.* (1995): Available potential energy and mixing in density-stratified fluids. *J. Fluid Mech.*, **289**:pp. 115–128, doi:10.1017/S002211209500125X

Yaglom, A. M., **Kader, B. A.** (1974): Heat and mass transfer between a rough wall and turbulent fluid flow at high Reynolds and Péclet numbers. *J. Fluid Mech.*, **62(03)**:pp. 601–623, doi:10.1017/S0022112074000838

Zweigle, T. (2011): *Direkte numerische Simulation von Salzfingern - Direct numerical simulation of saltfingers*. Ph.D. thesis, Universität Bremen

List of Tables

List of Publications

Peer-reviewed Papers

- **Keitzl, T., Mellado, J.-P., Notz, D.** (2015); Impact of Thermally Driven Ocean Turbulence on the Melting of Ice. *J. Phys. Oceanogr.*, (submitted).
- **Keitzl, T.**; The Interfacial Equilibrium of an Ablating Ice–Ocean Interface: An Assessment of the Turbulent-Flux Ratio and the Molecular-Flux Ratio in Semi-convection. *The Cryosphere*, (in preparation).

Other scientific contributions

- **Keitzl, T.; Mellado, J.-P.; Notz, D.** (2014): Turbulence-enhanced bottom melting of a horizontal glacier–lake interface. *2014 AGU Fall Meet.* (Poster)
- **Keitzl, T.; Notz, D.; Mellado, J.-P.** (2014): How fast does ice melt from below? (American Physical Society, 2014), doi:10.1103/APS.DFD.2014.GFM. (Video)
- **Keitzl, T.** (2012): Shi, X. et al. - Studies on Ice-Ocean Heat Flux Parameterization in Sea Ice Models. *Ice at the Interface: Atmosphere-Ice-Ocean Boundary Layer Processes and Their Role in Polar Change*, Boulder, (Workshop contribution)

List of Tools and Acknowledgements

This work was written in the research group *Turbulent Mixing Processes in the Earth System* (*TMP Group*) lead considerately and competently by *Juan-Pedro Mellado*. It is a combined laboratory and simulation study in collaboration with the research group *Sea Ice in the Earth System* lead by *Dirk Notz*. Both group leaders supervised this study. As a combined study more tools and support was required than average. For the laboratory work, *Simon Kamprath*, *Felix Matt*, *Thilo Klenz*, and *Niels Fuchs* assisted in the data acquisition. *Björn Brügmann* and *Wolfgang Keitzl* were always ready to support me in matters of electronics. For the simulation work, the whole *TMP Group* provided the scientific comfort. This work has been produced with the help of a variety of hardware and software, and the infrastructure provided by the *Max Planck Institute for Meteorology*. The following has provided the background for my daily labour.

The **computational resources** for the simulations was supplied by *Jülich Supercomputing Centre* under the project grant `hhh07` and by the *German Climate Computing Centre*.

The **laboratory equipment** for the experiments was supplied by the research group *Sea ice in the Earth System*. A Julabo FB50-HL thermostat, a cold room, lots of water and a tank were the main components for the setup of the laboratory experiment. A Campbell CR3000 data logger, a Campbell AM16/32B Multiplexer, and BetaTHERM 2.2K3A1B Thermistors were used for the data acquisition. The thermistor cascade that kept the thermistors safe and in situ was fabricated by *Leif Riemenschneider*. The ice frame and lifting system was fabricated and installed by the institute's workshop.

It follows a list of **software** that was used over the course of this work.

- Direct-numerical-simulation code & the associated toolchain. By the *TMP Group*.
- Tkstat. A graphical user interface to comfortably access the statistic output of the direct numerical simulation code. By the *TMP Group*.
- Avizo and Paraview. Visualisation Software by FEI Software and Kitware.
- Python with NumPy Stack (NumPy, SciPy, Matplotlib, IPython) and NetCDF Library. Multi-paradigm scripting language with a scientific computing package. By the Python Software Foundation.
- MatLab, Mathematica.
- Gnuplot, Xmgrace, Inkscape, Gimp, Libre Office, FFMPEG, Latex, Kile, Zotero.
- stats.py. A python script that transforms the statistics output of the direct numerical simulation to NetCDF format. Written by Chiel van Heerwaarden.

- nc_gen.py. A python script that transforms binary scalar fields to NetCDF format. Written by Cedrick Ansorge.
- read_field.f90. A fortran code that reads the header of a binary scalar field. Written by Cedrick Ansorge.
- WebPlotDigitizer. An application that helps to manually digitise data from an image. Written by Ankit Rohatgi. http://arohatgi.info/WebPlotDigitizer/app/
- Colour Brewer. A website that provides colourblind safe, print friendly and photography safe colour scales. By Cynthia Brewer, Mark Harrower and The Pennsylvania State University. http://www.colourbrewer2.org
- Detexify. An application that provides the latex symbol from a free-hand drawing. Philipp Kühl and Daniel Kirsch. http://detexify.kirelabs.org/classify.html

This work was financially supported by the Research-Group Program of the Max Planck Society.